Physik-Department

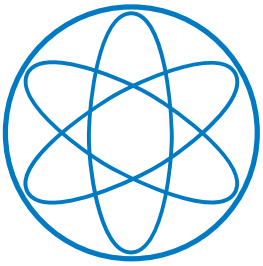

Diffusion Dynamics in liquid and undercooled Al-Ni alloys

Dissertation
vorgelegt von
Sebastian Stüber

Technische Universität München

TECHNISCHE UNIVERSITÄT MÜNCHEN/
Lehrstuhl für Experimentalphysik IV
Physikdepartment E13

Diffusion Dynamics in liquid and undercooled Al-Ni alloys

Sebastian Stüber

Vollständiger Abdruck der von der Fakultät für Physik der Technischen Universität München zur Erlangung des akademischen Grades eines

Doktors der Naturwissenschaften (Dr. rer. nat.)

genehmigten Dissertation.

Vorsitzender:
Univ.-Prof. Dr. M. Ratz

Prüfer der Dissertation:
1. Univ.-Prof. Dr. A. Meyer,
Ruhr-Universität Bochum
2. Univ.-Prof. Chr. Pfleiderer, Ph.D.

Die Dissertation wurde am 05.11.2008 bei der Technischen Universität München eingereicht und durch die Fakultät für Physik am 21.01.2009 angenommen.

Summary

This work presents data on Ni self-diffusion in binary Al-Ni alloys with high precision. For this, we combined two techniques: containerless electromagnetic levitation to position the samples, and neutron time-of-flight spectroscopy to measure the decay of the self-correlation.

This combination offers new measurement ranges, especially at low temperatures, several hundreds of Kelvin below the liquidus temperature. Because without container, the primary cristallization seeds for the metallic melt are avoided. But it is also possible to measure reactive samples, and at very high temperatures at and above 2000 K, as problematic reactions with the containing cask won't occur. Furthermore this technique also enables measurements at higher momentum transfer q, as one does not have to limit the q-range of the measurement to avoid Bragg peaks of the solid container material.

By this time-of-flight spectroscopy on levitated metallic melts, it is possible to determine the Ni self-diffusion in these alloys directly and on an absolute scale. The dependence of the Ni self-diffusion coefficient on temperature and concentration was studied in pure Ni and binary Al-Ni alloys. In a temperature range of several hundred degrees, we always found Arrhenius-like temperature dependence of the diffusion, irrespective of possible undercooling.

In the context of these measurements, we also studied the interdependence between diffusivity in the metallic melt and its quasielastic structure factor. Time-of-flight spectroscopy made it also possible to derive the dynamic partial structure factors of the binary alloy $Al_{80}Ni_{20}$.

All this to enable a better understanding of the atomic processes in the metallic melt, especially of the undercooled melt, as an alloy is always formed out of the (undercooled) melt of its stoichiometric compounds. For this, material transport and diffusion are immensely important. The final goal would be materials design from the melt, i.e. the prediction of alloy properties in advance by computer simulation. But simulation needs exact data on dynamics and diffusion coefficients in the melt.

That is one goal of this work, but also to give an insight into the processes in metallic melts on an atomic scale.

Zusammenfassung

Diese Arbeit untersucht die Ni-Selbstdiffusion in binären Al-Ni-Legierungen. Dazu wurden zwei herausragende Techniken kombiniert: die elektromagnetische Levitation als behälterlose Methode zur Probenpositionierung, und die Neutronenflugzeitspektroskopie.

Diese Kombination ermöglicht den Zugang zu neuen Messbereichen, insbesondere tiefere Temperaturen unterhalb der Liquidustemperatur der Metallschmelze – da ohne einen Behälter die primären Kristallisationskeime stark reduziert sind –, aber auch höhere Temperaturen bis über 2000 K, sowie das Messen von chemisch reaktiven Proben, da keine schadhafte Reaktion mit dem Behälter befürchtet werden muss. Des Weiteren ermöglicht elektromagnetische Levitation auch die Messung über einen größeren q-Bereich, da Streubeiträge in Form von Bragg peaks des Behälters entfallen.

Mit dieser Methode der Flugzeitspektroskopie an levitierten Proben ist es nun möglich, die Ni-Selbstdiffusion absolut und direkt zu messen. Im Vergleich zu anderen Verfahren, wie Tracer Diffusion oder der Langkapillar-Technik, ist die Präzision, wie auch die Variabilität der Methode beeindruckend.

Es werden die Ergebnisse der Untersuchungen zur Abhängigkeit der Ni-Selbstdiffusion von der Konzentration und von der Temperatur für binäre Al-Ni-Legierungen dargestellt. Im untersuchten Temperaturbereich von etlichen 100 Grad über und unter der Liquidustemperatur findet sich dabei durchweg eine Arrhenius-Abhängigkeit.

Im Kontext dieser detaillierten Untersuchungen ergeben sich aber auch Zusammenhänge von übergeordnetem Interesse, wie z.B. die Relation zwischen effektiver Diffusivität und quasielastischem Strukturfaktor. Die Flugzeitspektroskopie ermöglichte außerdem die Bestimmung der dynamischen partiellen Strukturfaktoren von $Al_{80}Ni_{20}$ aus drei Messungen mit verschiedenen Ni-Isotopzusammensetzungen.

All dies soll dem besseren Verständnis der atomaren Vorgänge in der Metallschmelze, v.a. auch der unterkühlten, dienen, da eine Legierung stets aus der unterkühlten Schmelze erstarrt. Und deren Beschreibung setzt eine Kenntnis von Materialtransport und Diffusion voraus. Letzlich gilt als großes

Ziel die Vorhersage von Struktureigenschaften einer Legierung durch Computersimulation. Und für diese Simulation sind genaueste Daten zu Beweglichkeiten und Diffusionskonstanten in der Schmelze entscheidend.

Dazu soll diese Arbeit beitragen, aber nicht zuletzt auch einen Einblick in das Geschehen auf atomarer Ebene in amorphen metallischen Flüssigkeiten gewähren.

Contents

Chapter 1

Introduction

Materials Science, and more specifically metallurgy, is one of the bases of modern technology and industrial production. Most machines need special alloying to get high-strength material. Its properties like stability and durability depend on the microstructure of the alloy. In this framework, it is vital to address and answer questions about diffusion and dynamics in the metallic melt, to understand the formation of solid alloys out of the liquid state. Dynamics and material transport in the liquid state might not only be faster than in the solid alloy, but the topology of random or short-range order in the melt can lead to correlations between the self-diffusion of the constituents of the alloy.

The solidification can be studied by phase field simulation [9]. The method substitutes boundary conditions at the solid-liquid interface by a partial differential equation of the (auxiliary) phase field, whose dynamics is given by a diffusion equation. So the value of the diffusion is an important input, and variations of the diffusion coefficient lead to strong deviations in the modeling.

Also the structure factors $S(q)$ of the alloys are important ways to gather data on the interdependences of material transport, and a possible interplay between structure and dynamics. The structure factors are input parameters to the powerful tool of mode coupling theory [31]. Possible effects of structure, particularly chemical ordering, on mass transport and structural relaxation will be one focus of this work.

The nucleation and growth of a crystal depends on the mass transport of the needed atoms to the correct nucleation site. Especially for intermetallic compounds like $Al_{50}Ni_{50}$, mass transport is provided for by the self-diffusion of the constituents, here Al and Ni. Interdiffusion is not relevant in this case, as the concentration from melt to compound does not change.

However, a recent study of Kerrache et al. [50] of this system has shown

that crystallization kinetics is much slower than expected by the classical model [29, 94]. This is because the speed of crystal growth is limited by the amount of atoms in the liquid-crystal interface, see Fig. 1.1. This is the

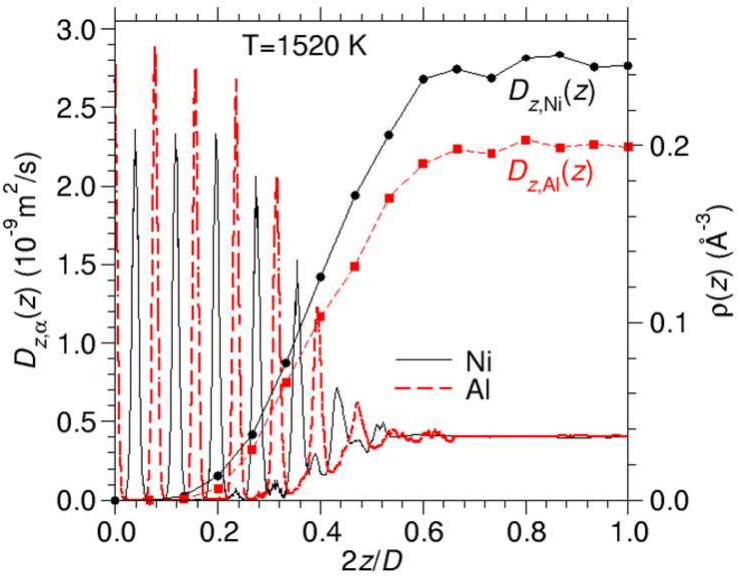

Figure 1.1: Diffusion and number density profiles of $Al_{50}Ni_{50}$, from [50].

result of molecular-dynamics computer (MD) simulation [43, 68]. The x axis gives the length in one direction of the crystal (in units normalized by the length of the simulation box). For the solid part up to about 0.3 relative units, we find the periodic change of Ni and Al high density (right ordinate), characteristic for crystal order. In the relatively short length from 0.3 to 0.6, corresponding to 5-6 atomic layers, the density of both constituents goes to the bulk value. Also the self-diffusion of Al and Ni then reaches the bulk value. The self-diffusion coefficients of the constituents increase by an order of magnitude within the interface region. MD simulation predicts a smaller value of the Al self-diffusion coefficient than the Ni self-diffusion coefficient.

Studying mass transport in the liquid alloy is one step towards the goal of virtual materials design from the melt, which has to rely on the correct modeling of the diffusion in the alloy. This modeling in turn needs reliable data on the temperature and concentration dependence of the diffusion constants. To derive these quantitative data on diffusion in the studied systems, with small error and covering wide temperature and concentration ranges, is the other major part of this thesis. We will present a technique to measure (Ni) self-diffusion coefficients directly.

Understanding the diffusion mechanism in metallic alloys has been a

scientific goal for quite some time, started by Roberts-Austen as early as 1883 [76]. For the largest part, these diffusion experiments worked with tracer methods [26, 34, 97], or via a long capillary [32, 70, 81]. The drawbacks are the limitation to the solid state, and buoyancy driven effects, respectively, leading to errors of the order of the determined diffusion itself. Problems occur during the melting of the diffusion couple with two cylindrical alloys of different compositions. Due to their different composition, they also have different melting temperatures and also different densities, which leads to buoyancy-driven convection [45]. Furthermore, during solidification, there is the danger of precipitation of different crystal phases. To overcome these problems, recent experiments were performed under microgravity conditions in space to reduce the convection [30]. Another option is to use *in-situ* X-ray radiography to study crystal growth kinetics [33].

Studying the dynamics of a metallic melt is chiefly done by containing the liquid in a stable container (made out of Pt or Al_2O_3, e.g.), and performing scattering measurements with neutrons or X-rays. This leads to problems by the demands of containing the liquid metal, thus reducing the accessible temperature range and also limiting the experiments to less active alloy systems. But it also leads to restrictions of the range of possible momentum transfer q (due to unwanted scattering from containers) and prevents undercooling.

Electromagnetic levitation (EML) [38, 40] now is the container-free method to overcome these limitations. A varying magnetic field induces currents in the electrically conductive sample and, by Lorentz' rule, leads to a force counteracting gravity, but also heating the sample. This is done in an ultrapure gas environment. As there are no nucleation seeds from container walls, this technique allows to undercool the metallic melts by several hundred degrees.

The advantage of electromagnetic levitation over other levitation techniques (like electrostatic [74] or aerodynamic [55] levitation) is first of all that the induced eddy currents lead to a small temperature gradient within the sample of just a few K [23]. The convective flow, in the order of less than cm/s [86] to at most some m/s, depending on heating power and conductivity of the sample alloy, will not affect the determination of the self-diffusion coefficients when probed on atomic length and picosecond time scales, cf. the results presented in later chapters and appendix B. So the obtained diffusion coefficients are not altered by convective flow [67]. Also for electromagnetic levitation, one can use larger samples than for electrostatic levitation. This is very important to have enough scattering intensity to get satisfactory statistics within a few hours of levitation experiments. For Ni-rich alloys, the effect of multiple scattering on the measurement has then to be studied.

A new coil design, see Fig. 1.2, ensured a good visibility of the sample

alloys. The samples with a diameter of about 8 mm are held within water-

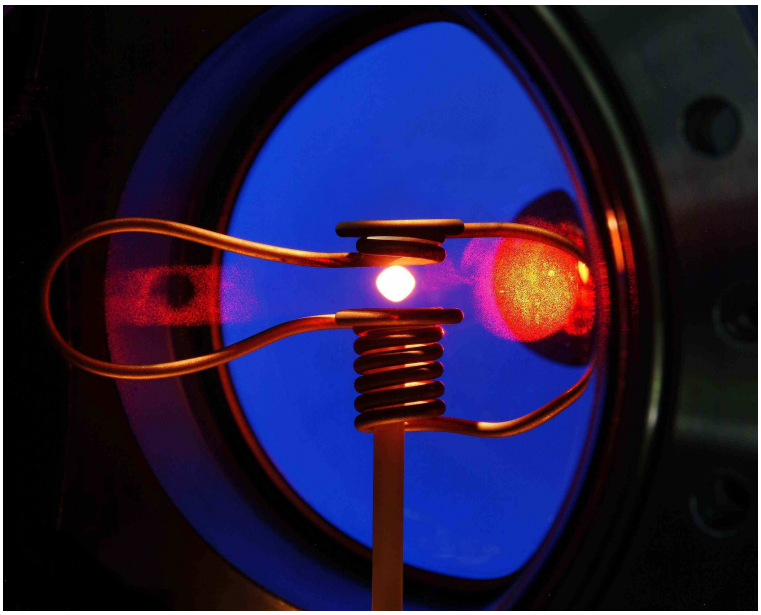

Figure 1.2: Picture of newly designed copper coil with excellent visibility of the sample.

cooled Cu windings of a coil, producing a radiofrequency field. The top and bottom part are 1 cm apart. With some concession for shielding, it is still possible to cover a large detector area of the spectrometer. For details, see chapter 3.2.1.

Containerless processing in combination with quasi-elastic neutron scattering (QENS) offers several possibilities for extended measurement ranges: higher temperatures and access to reactive samples as the melt is self-contained in an inert gas and no reaction with a crucible can occur; possible undercooling due to the removal of the dominant crystallization seeds of a container; and finally also an increased q-range due to a highly reduced scattering from extraneous material.

First QENS measurements in combination with levitation on pure liquid Ni [67] proofed the feasibility of this method. It is then in this work used for binary alloys, to systematically study the temperature and concentration dependence of the Ni self-diffusion coefficients, which, as already mentioned, is indispensable for detailed and reliable simulations of nucleation. With the new time-of-flight spectrometer TOFTOF at the *Forschungsneutronenquelle Heinz Maier-Leibnitz*, we could measure also dynamic partial structure factors to fully describe the correlations of a binary Al-Ni liquid. As our measurements are limited to strong incoherent scatterers as Ni, Ti, Co, or Cu, the study of partial structure factors, in combination with simulation is needed

to learn about the dynamics of the other constituents.

Most simulations, in the lack of experimental data, assume a fairly constant diffusion coefficient for the mass transport during solidification, with a value derived from capillary diffusion measurements at best, though the process in reality works out of the metastable undercooled liquid state, where no value of diffusion has been measured yet.

With QENS, we probe the stochastic scattering of the neutrons on diffusing constituents around the elastic line, especially of elements with high incoherent scattering cross section like Ni ($\sigma_{\mathsf{inc}} = 5.2\,\mathrm{barn}$). The resulting scattering function can be analyzed to derive the (Ni) self-diffusion coefficient as a key to the understanding of the system dynamics. This will be done concentration and temperature dependent. There is no general theory on the temperature dependence of self-diffusion coefficients, although considerable effort was made to find a universal relation of self-diffusion to temperature. For metallic melts with lower density of packing such as Sn, Pb, In and Sb, a T^2 law has been reported [46, 63]. We want to present studies in a different system with high packing fraction and at high temperatures, the self-diffusion in Ni. What temperature dependence prevails in this system? Here, also the possible effect of undercooling on the diffusion will be of interest.

For Ni, we have literature values available for the self-diffusion coefficients, measured by container experiments [16, 17]. Ni is a strong scatterer and easy to handle. It will be used to test the working principle of the combination of electromagnetic levitation with quasi-elastic neutron scattering. It was possible to measure at temperatures up to 2000 K and to keep the samples stable, also in the undercooled state, for a minimum of two hours. Multiple scattering of Ni was not inhibiting the derivation of self-diffusion coefficients, as comparison to the data from the container experiments shows. So it can be deduced that it will be similar for the weaker scattering Al-Ni alloys. The proportionality of the half width at half maximum (HWHM) of the scattering law to q^2, of the hydrodynamic limit of small momentum transfer q, still holds far above $1\,\mathrm{Å}^{-1}$. This will enable us to measure the self-diffusion coefficients on an absolute scale.

We will present measurements on binary Al-Ni compounds, a basis system for the study of super alloys[1] (as $Al_{25}Ni_{75}$ is one of the major stabilizing phases in superalloys), including also the refractory intermetallic compound $Al_{50}Ni_{50}$ with a rather high liquidus temperature of 1940 K. Measurements of this alloy at various temperatures was possible, because we could undercool the melt by more than 250 K. Especially for the intermetallic compounds,

[1] i. e. alloys with a high thermal stability

where the composition in the melt is the same as in the crystal, one might expect an influence of the phase diagram/ of the composition on the dynamics of the metallic melt. This will be studied for a broad compositional range. Important research has already been done in the Al-Ni system, comprising molecular dynamic (MD) simulation [18, 43], diffraction measurements [61], and QENS [18].

Al-Ni alloys show a chemical short-range order (CSRO) in the melt [18, 61], that means that Ni and Al atoms do not arrange just randomly in the liquid, but show certain preferred (chemical) arrangements. In measurements, this can be seen as a prepeak in the coherent contribution to the quasi-elastic structure factor. A comparable CSRO was also found in the Ni-Zr [58, 59, 93] and Al-Cu [8, 11] systems. The Ni self-diffusion coefficients in Al-Ni exhibit a nonlinear dependence on concentration with a pronounced increase on the Al-rich side [18]. However it was not possible yet to derive conclusively diffusion coefficients for the complete compositional range.

A first goal of this work was to complete the data of Das et al. [18] on Ni self-diffusion coefficients on the Ni rich side with higher liquidus temperatures and to test the consistency between experimental data and simulations by Horbach et al. [43]. Detailed structural information of Maret et al. [61] on $Al_{80}Ni_{20}$ were complemented by the measurement of dynamic partial structure factors. We also performed measurements on the same compositions and temperatures as in [18] to see whether our different sample geometry with a thicker sample (8 mm diameter sphere vs. hollow cylinder with 1.2 mm wall thickness and 22 mm outer diameter) poses problems due to relatively increased multiple scattering. This was found to be not disturbing as we are mainly interested in the half width at half maximum (HWHM), which is not very sensitive to deviations from single Lorentzians. We will be able to discuss the concentration and temperature dependence of the Ni self-diffusion in the complete compositional domain, as the handling of high temperatures and undercooling are possible with the levitation technique. In the binary Al-Ni system, the mass transport seems to be dominated by the packing fraction [18], yet one should also check for possible influences of the underlying phase diagram.

The intermetallic compound $Al_{50}Ni_{50}$ with the high liquidus temperature of 1940 K is of particular interest; to see whether this high liquidus is reflected in the dynamics of the melt. Simulation [18] predicts that the Ni self-diffusion in Al-Ni does not vary on the Ni rich side from pure Ni up to 50 at.% addition of Al. Then again, in [50] it was found that the crystal growth for the intermetallic compound $Al_{50}Ni_{50}$ is much slower than for a pure metal like Ni. The explanation of the MD simulation ascribed this to a diffusion-limited growth mechanism together with a peculiar attachment

kinetics to the interface [5]. We will measure the Ni self-diffusion coefficient in this intermetallic compound to see, whether the diffusion really is similar to that in pure Ni and Ni-rich compounds of Al-Ni, and to determine the composition at which the dynamics do change. In addition to the determination of the Ni self-diffusion coefficients on an absolute scale with small error, we will also track the q-dependent dynamics from small q values of about $0.5\,\text{Å}^{-1}$ up to typical momentum transfers of the first structure maximum around $3\,\text{Å}^{-1}$ by means of an effective diffusivity $D(q)$. Simulation data [19] predict an interesting q dependence of correlation lifetimes, and relates the interdiffusion to the self-diffusion of the constituents.

In addition to the intermetallic compound $Al_{50}Ni_{50}$, we studied an alloy of the Ni-rich side ($Al_{25}Ni_{75}$) and an Al-rich one ($Al_{80}Ni_{20}$). For the binary alloy $Al_{80}Ni_{20}$, we could compare our EML results with data from container experiments [16, 17], in order to assure the feasibility of the combination of EML with QENS to derive diffusion coefficients with high precision.

We also used this Al-rich compound to perform detailed studies on q-dependent effects of diffusion on structure and CSRO. $Al_{80}Ni_{20}$ is a system with a relatively low liquidus temperature of 1245 K. To get enough statistics, we measured for 24 h respectively three samples with different isotopic compositions: natural Ni isotopic composition, a sample enriched with ^{58}Ni, and one with ^{60}Ni enrichment. For this study, the alloys were prepared within Al_2O_3 containers.

Findings in the Al-Ni system are in very good agreement to simulations' results and predictions. We wanted to test the broader significance of these findings also for other alloy systems, so we performed diffraction experiments on further Ni based binary alloys, for example the Ni-Zr system. To check, whether there is also a concentration dependence of the Ni self-diffusion coefficients, and if the glass forming properties of Ni-Zr have an influence on dynamics. However, these results are not part of the present work and the kind reader is referred to the cited publications, see also App. C. A short outlook will be given in chapter 5.3.

Chapter 2 will give a short introduction to the general properties of the studied Al-Ni alloys, their synthesis, and will also present the basic concepts of diffusion in liquid alloys. The next chapter will explain the used experimental techniques of electromagnetic levitation and quasi-elastic neutron scattering in more detail, with emphasis on data analysis. In chapter 4, the concentration and temperature dependence of Ni self-diffusion in pure Ni and binary Al-Ni alloys will be studied. Chapter 5 focuses on the relation between structure factor and dynamics, and contains the measured partial structure factors, static and dynamic, of $Al_{80}Ni_{20}$.

Chapter 2

Liquid metals and alloys

2.1 General properties of Al-Ni

Al-Ni has some relevance when dealing with Ni-based superalloys, i.e. alloys with high thermal stabilities, used for example in airplane turbines. $Al_{25}Ni_{75}$ is a major stablizing component in these superalloys, see [21]. Also, the intermetallic compound $Al_{50}Ni_{50}$ is used as coating for blades and vanes in the hot sections of gas turbines, formed by the inward diffusion of aluminum into the surface of a nickel-based superalloy or the outward diffusion of nickel into the gas-deposited Al [21].

The first studies of the phase diagram were performed by Gwyer [35]. For detailed information on the phase diagram, see [37, 56]. Al-Ni is a well-studied system, with many sorts of experimental data available, be it on density, viscosity or structure, see the following for some details. But there is also a number of theoretical works simulating the properties of Al-Ni alloys, using molecular-dynamics computer (MD) simulation or mode-coupling theory (MC) calculations. Our results serve as a test for MD simulation and MC calculations. If the experiments show the validity of the simulation work, then MD simulation and MC theory can give a more detailed insight into these processes as they have access to detailed particle trajectories, which for example in the case of Al-Al correlations are not accessible directly by experiment. In the following, we will include the simulation work of various authors into our discussion.

Structure A liquid metal (or alloy) is amorphous condensed matter, and as such its atomic structure lies between the regular long-range order of a crystal and the free floating atoms of a gas. As in amorphous solids, there usually is also a short-range order in liquids [27].

To quantify this topological ordering of atoms in the (metallic) liquid, two major functions are used (see textbooks like [98] and [62]). The directly accessible function, by neutron diffraction, in reciprocal space is the structure factor $S(q)$. It relates to the differential scattering cross section by [24]

$$\frac{\mathrm{d}\sigma}{\mathrm{d}\Omega} = Nb^2 S(q) \quad , \tag{2.1}$$

with b an appropriate scattering factor, see the discussion in chapter 3.4.5. Fig. 2.1 shows a typical result of a neutron diffraction experiment on levitated liquid $Al_{25}Ni_{75}$, performed at the instrument D20 of the Institut Laue-Langevin [57]. Where in a crystal we would expect Bragg peaks (ideally δ

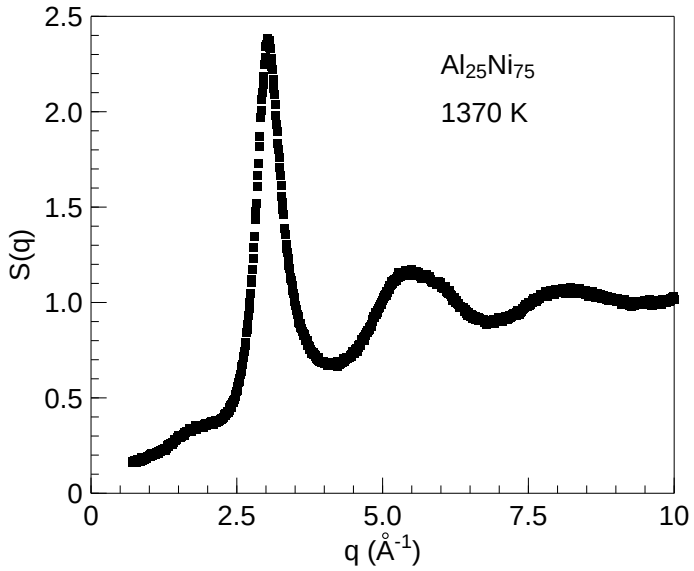

Figure 2.1: Total neutron structure factor S(q) for liquid $Al_{25}Ni_{75}$, measured at D20 at ILL.

functions, scattering is only allowed at certain angles corresponding to certain q values), in a liquid, the structure factor is a continous function. $S(q)$ is usually normalized to the total scattering cross section of the alloy and therefore goes to 1 for large momentum transfer q. The first maximum of $S(q)$ at $q = 3\,\text{Å}^{-1}$ corresponds to the reciprocal approximate average nearest neighbor distance $2\pi/\langle a \rangle$. It is followed by oscillations of $S(q)$ around 1 with decreasing amplitude. For $q \approx 1.7\,\text{Å}^{-1}$, a prepeak, corresponding to larger r than the respective value of the structure factor maximum, is visible, which is a strong indication of chemical short-range order (CSRO). The measured structure factor is in accordance with the simulation of [18]. The second maximum of $S(q)$ at $5\,\text{Å}^{-1}$ shows a shoulder on the right flank at approx. $6\,\text{Å}^{-1}$.

In one-component systems, this is an indication for icosahedral short-range order in the melt [39]. As inferred from our data, in binary and multicomponent systems, the situation becomes more subtle, as this shoulders appear dependent on, for example, the isotope (^{58}Ni instead of ^{60}Ni, e.g.), cf. Fig. 2.3 or 5.21. The diffraction of $Al_{25}Ni_{75}$ is dominated by the coherent scattering of Ni, so it can be expected that the partial structure factor $S_{NiNi}(q)$ will resemble the features of the total neutron structure factor $S(q)$, especially also show the prepeak below $2\,\text{Å}^{-1}$. A comparison of $S_{NiNi}(q)$ and $S(q)$ of $Al_{80}Ni_{20}$ from a similar diffraction experiment can be found in [61]. For a more detailed study of partial structure factors in the quasi-elastic region, see chapter 5.1.

In real space, the pair distribution $g(r)$ gives the deviation of the probability to find another atom at a distance r of a given atom from the product of the independent probabilities of finding both atoms at their respective positions. But as we deal with probabilities, $g(r)$ is just an average over time and all atoms. $g(r)$ is related to $S(q)$ by [96]

$$g(r) = 1 + \frac{1}{2\pi^2\rho_0 r}\int_0^\infty q\,[S(q)-1]\sin(qr)\mathrm{d}q \quad . \tag{2.2}$$

Fig. 2.2 shows the corresponding pair distrbution $g(r)$ to the $S(q)$ of Fig. 2.1 The dotted line shows the oscillations for low distances, where $g(r)$ ought to

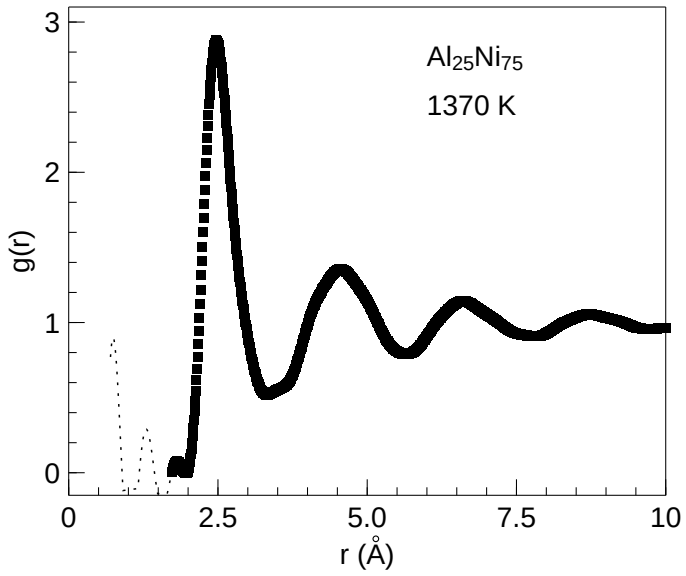

Figure 2.2: Pair distribution for liquid $Al_{25}Ni_{75}$, measured at D20 at ILL.

be zero. As it is experimentally impossible to measure all possible q values,

this is an unavoidable feature. For large distances r, the probability to find another atom corresponds just to the density of the liquid, so

$$\lim_{r\to\infty} g(r) = 1 \quad . \tag{2.3}$$

But for lower distances, there are regions with increased and regions with decreased probability. So oscillations of $g(r)$ correspond to preferred and avoided distances. In a crystal, instead of these oscillations we find delta peaks, and in the free atom gas just the constant value 1, from density. Below a certain value of r, the probability to find another atom is 0. The first maximum is close to the average next neighbor distance, and with $r_0 = 2.5\,\text{Å}$, we see that $Al_{25}Ni_{75}$ is a densely packed system.

The experiments of Maret et al. [61] and Das et al. [18] have shown, that all Al-Ni alloys show a prepeak in the total neutron structure factor, whose position and intensity is dependent on composition. This indicates chemical short-range order (CSRO), meaning a deviation from randomly packed hard spheres, to preferred arrangements regarding atom types, not necessarily positions. These structural features occur on length scales beyond the one of typical distances between nearest-neighbor atoms. Egry et al. [22] have performed X-ray aborption spectroscopy to study the CSRO of Al-rich Al-Ni alloys. For calculations of CSRO for transition metal glasses, see Ref. [64]. Asta et al. [2] have also done *ab initio* molecular-dynamics studies of the structural and thermodynamic properties of liquid Al-Ni alloys.

Fig. 2.3 shows the total neutron structure factor measured by Maret et al. [61] for $Al_{80}Ni_{20}$ with three different Ni isotopic compositions: natural abundance, enriched ^{58}Ni, and enriched ^{60}Ni, at 1330 K. We see that similar to Fig. 2.1 in $Al_{25}Ni_{75}$, in $Al_{80}Ni_{20}$ there is also a prepeak at $q \approx 1.7\,\text{Å}^{-1}$ visible in the alloys with natural Ni isotopic enrichment and ^{58}Ni, but not in the one with ^{60}Ni. We will see later on, that this is because in $Al_{80}{}^{60}Ni_{20}$, we probe more strongly the Al dynamics (Al scatters more strongly than ^{60}Ni), and the Al-Al partial structure factor does not show a prepeak.

In Fig. 2.4, we have reproduced the partial structure factors as determined by Maret et al. [61]. We will discuss partial structure factors in great detail in chapters 3.4.5 and 5.1, where we will focus on the q-range of the prepeak by measuring $Al_{80}Ni_{20}$ with quasi-elastic neutron scattering. But intriguing properties visible in the Faber-Ziman partial structure factors are that the prepeak of CSRO indeed shows up in the Ni-Ni correlation, $I_{MM}(q)$ in Fig. 2.4 a), and not in $I_{AlAl}(q)$. The first peak of $S_{CC}(q)$ in Fig. 2.4 b) at $2\,\text{Å}^{-1}$ (somewhat higher q than the prepeak at $1.7\,\text{Å}^{-1}$), is also a clear indication of CSRO.

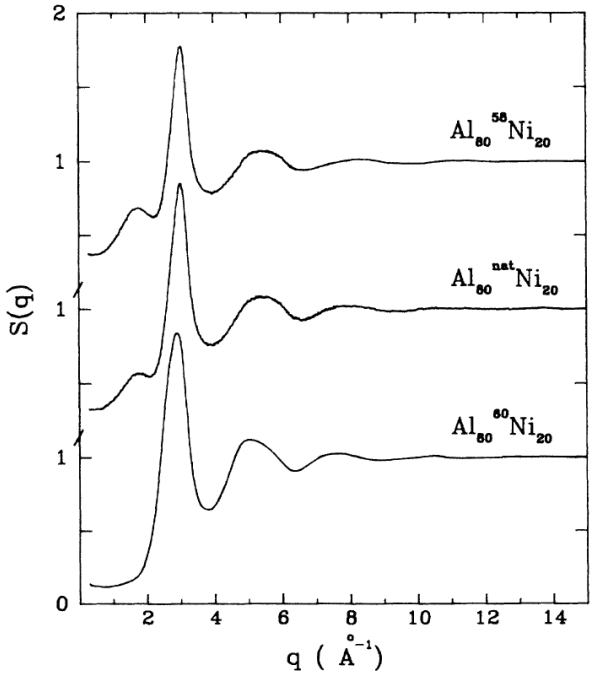

Figure 2.3: Total neutron structure factor of $Al_{80}Ni_{20}$ with natural Ni isotopic composition, ^{58}Ni, and ^{60}Ni, at 1330 K, from [61].

Density and viscosity are important parameters to describe the behavior of liquid metals and alloys. For example, the density of $Al_{25}Ni_{75}$ entered Eq. (2.2) to determine $g(r)$. To measure density and viscosity of liquid alloys is a demanding enterprise, and we cannot go much into details here, for more information see the overview in [14] and [12].

The temperature and concentration variation of the density of Al-Ni alloys was studied first by Ayushina et al. [3]. Al-Ni alloys show a non-linear dependence of density on composition. Das et al. [18] used this to calculate the atomic volume of the respective Al-Ni alloys. The resulting decrease of the packing fraction upon increasing the Al content in the alloy, has direct results on the Ni self-diffusion coefficient, which will increase strongly on the Al-rich side, cf. chapter 4.2.2.

To measure the density of a metallic alloy, one can also use electromagnetic levitation [10]. This has again the advantage that it is possible to determine the density of the metastable liquid alloy below its liquidus temperature. This method measures the volume of the levitated sample, by taking sectional images, frequently taken from three orthogonal directions. Together with the measured weight, one can easily calculate the temperature dependent density. The densities of liquid alloys were generally found to be

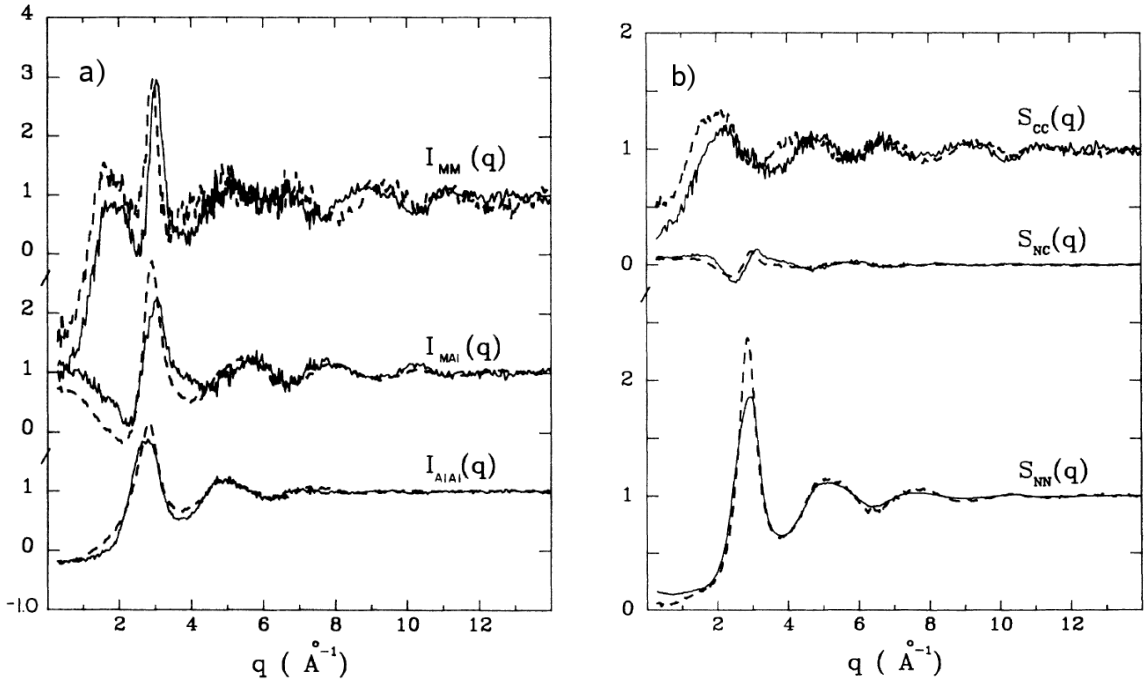

Figure 2.4: Partial structure factors of $Al_{80}Ni_{20}$ at 1330 K in Faber-Ziman notation (a) and Bhatia-Thornton notation (b) (solid lines). "M" stands for Ni. The dashed line shows data for $Al_{80}[Mn_x(FeCr)_{1-x}]_{20}$. From [61].

a linear function of temperature [1, 3].

Also the viscosity η of liquid metals and alloys can be determined using a levitation technique [1]. Here, the damping of oscillations of the levitated droplet is measured. The damping constant Γ is given by [15]

$$\Gamma = \frac{20\pi}{3}\frac{R\eta}{m} \quad , \tag{2.4}$$

with R and m the radius and the mass of the sample droplet, respectively. For Eq. (2.4) to be valid, one has to assume a spherical shape of the droplet and that there are no further damping mechanisms present. To come nearer to this assumptions, experiments were performed under micro-gravity conditions [54].

The viscosity in liquid metals and alloys is usually supposed to have an Arrhenius-like temperature dependence [16]. A suspected connection between viscosity η and diffusion dynamics is the so-called Stokes-Einstein relation[4, 51, 89]

$$D = \frac{k_B T}{6\pi\eta a} \quad , \tag{2.5}$$

where a usually is set to the hydrodynamic radius, and D is the self-diffusion coefficient. But this relation is not to be taken for granted, as it does not hold under all conditions, regarding, for example, temperature and density of the liquid [13, 65, 66].

For the temperature dependence of the viscosity of Al-Ni alloys, see [72]. More data will soon be available, using the new high-temperature oscillating cup viscometer, developed by Kehr et al. [49].

2.2 Diffusion in liquid metals and alloys

2.2.1 Basic concepts

Depending on the examined time- and momentum-scale, the movement of a particle can be described as free, ballistic movement (for very short times and distances), or as performing a random walk in the so-called hydrodynamic limit $q \to 0, \omega \to 0$. There, Fick's law is the description of the (self) diffusion of the test particle.

Fick's law for the problem of self-diffusion in a monatomic [1] liquid can be written as (see [80] or [96])

$$\frac{\partial G_s}{\partial t} = D\nabla_R^2 G_s \quad , \tag{2.6}$$

with $G_s(\mathbf{\Delta R}, \tau)$ the self-correlation function, which gives the probability to find a particle at position $\mathbf{\Delta R}$ at a time $\tau = t - t_0$ after this same particle was at position 0 at time t_0. D of Eq. (2.6) is the self-diffusion coefficient. At time t_0, G_s is given as

$$G_s(\mathbf{\Delta R}, t_0) = \delta(\mathbf{\Delta R}) \quad . \tag{2.7}$$

The solution to Eq. (2.6) is

$$G_s(\mathbf{\Delta R}, \tau) = (4\pi D\tau)^{-3/2} \exp(-\frac{(\mathbf{\Delta R})^2}{4D\tau}) \quad . \tag{2.8}$$

For times τ long enough that $\left\langle (\mathbf{\Delta R})^2 \right\rangle / \tau$ can be considered constant, the self-diffusion coefficient D is

$$D = \lim_{\tau \to \infty} \frac{\left\langle (\mathbf{\Delta R})^2 \right\rangle}{6\tau} \quad . \tag{2.9}$$

[1] Later on we will use the results of this derivation for QENS on Al-Ni alloys. For a first-hand approximation, the neutrons are assumed to scatter only from the Ni atoms with much higher (incoherent) scattering length than Al (with 0 incoherent scattering length). So we study basically the diffusive motion of Ni alone. For a more detailed study, we refer to the determination of partial structure factors in chapter 5.1.

Fourier transformation in space of Eq. (2.8) gives the incoherent intermediate scattering function for the diffusing particle

$$I_s(q,\tau) = f_q \mathrm{e}^{-q^2 D\tau} \quad , \tag{2.10}$$

where f_q corresponds to the Lamb-Mößbauer factor (also known as nonergodicity parameter). It expresses the decorrelation of the system from its state at time $t=0$ due to vibrations, and in glass-forming systems also due to rattling of the particles in their cage [19, 28].

Another Fourier transform in time leads to the (incoherent) scattering law

$$S_{inc}(q,\omega) = \frac{A}{\pi\hbar} \frac{Dq^2}{\left(Dq^2\right)^2 + \omega^2} \quad . \tag{2.11}$$

For an overview of the magnitude and relations of these diffusion values, see e.g. [32, 43] with inclusion and comparison of recent measurements. A more detailed listing of diffusion related termini can be found in [52].

Hard sphere model For most metallic liquids, an approach with an assortment of hard spheres, i.e. assuming a infinitely repelling potential below a hard sphere radius σ_i, leads to satisfying results for the global reproduction of, for example, the static structure factor. But important details like the prepeak of CSRO, or the q dependence of diffusivity (see chapter 5.2) cannot be explained by this simplification.

2.2.2 Experimental methods

The following experimental methods are the main ways to derive self-diffusion coefficients in metals.

Tracer Diffusion The (self) diffusion coefficient is studied by following isotopes of the respective component, marked either by using a radioactive isotope and performing activation analyses, or identified by mass spectroscopy. An amount of the isotopes is put at one end of the sample alloy of given composition. After a given diffusion time (through the solid) at a given temperature, the sample is sliced, and the concentration of the isotope markers is measured using the decay characteristics, or mass spectroscopy. The concentration of tracers as function of penetration gives the diffusion coefficient. See the review article of Faupel et al. [26] and [34, 97].

Long-capillary method The long-capillary (LC) method also uses the help of nuclides to follow the dynamics. But it is performed by adding also a chemical gradient. A diffusion couple of slightly differing concentrations drives the diffusion. The sample is heated to the liquid state. Thus, it is possible to derive diffusion data in the liquid state, but buoyancy driven convection can lead to heavy disturbances. For examples of this technique, cf. [32, 70, 81].

Molecular-Dynamics simulation In molecular-dynamics computer (MD) simulation, the interactions between the atoms are modeled by choosing a suitable potential. For most of the data we will cite in this work, this was an embedded atom potential porposed by Mishin et al. [68]. Using Newtonian equations on a given set of some thousand atoms, the correlations are calculated for various time steps, giving time to equilibrate. MD simulation is a very good means for studying the mechanism of mass transport in the liquid, however, the absolute values of the derived diffusion coefficients may be off by about 20 % [18]. So we need neutron scattering experiments, first of all, to get the absolute values of the diffusion coefficients, and secondly, to check the quality of the model potential of MD simulation. For examples on Al-Ni liquid alloys, see [19, 43, 47, 50].

Fig. 2.5 from the work of Horbach et al. [43] gives an overview of diffusion constants in $Al_{80}Ni_{20}$, measured by quasi-elastic neutron scattering, the long-capillary technique, and derived by MD simulation. The self-diffusion coefficients D_{Ni} and D_{Al} from the simulation are very similar. This was observed in MD simulation for the Al-rich Al-Ni alloys with $c_{Al} >$,0.7 [18]. The neutron scattering results for D_{Ni} as well as the value from LC are in very good agreement with the simulation. The interdiffusion constant[2] is larger than the self-diffusion coefficients over the whole temperature range. Also the LC measurements show that $D_{AB} > D_{Ni}$. In a recent work [43], this has been discussed in the framework of the thermodynamic factor Φ [3] [43].

For the combination of electromagnetic levitation with neutron time-of-flight spectroscopy, used to derive (Ni) self-diffusion coefficients on an abso-

[2]In a polyatomic liquid, diffusion is under the influence of a gradient in chemical composition. The motion of one constituent causes a counterflow of the other constituent(s). This is quantified by the interdiffusion coefficient D_{AB}.

[3]The Darken relation, or more precise the Darken-Dehlinger relation, links the interdiffusion coefficient to the self-diffusion coefficients of the constituents [52]: $D_{AB} = \left(N_A \bar{V}_A D_B + N_B \bar{V}_B D_A\right) \Phi$, where N_i are the respective mole fractions, and $\bar{V}_i$ the partial molar volumes. Φ is the thermodynamic factor. For a recent study on the interplay of these different diffusion coefficients, see [93].

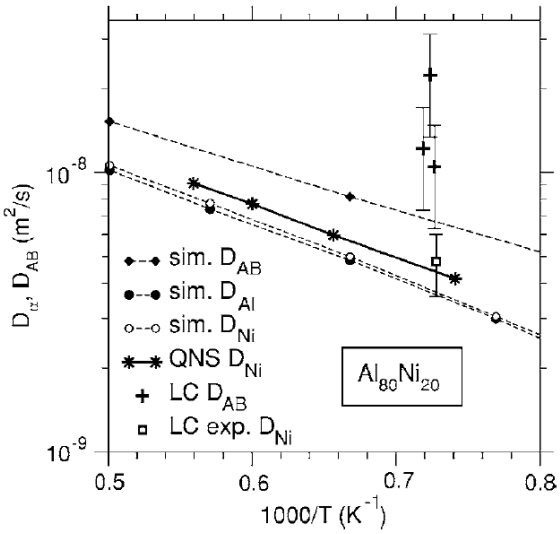

Figure 2.5: Interdiffusion and self-diffusion coefficients vs. inverse temperature, as obtained from experiment: quasi-elastic neutron scattering QNS, and long-capillary method LC, and from molecular-dynamics simulation sim. The lines through the data points are guides to the eye. The error bars of the simulation and QNS data are of the order of the size of the symbols. From [43].

lute scale, see chapter 3.

2.3 Sample synthesis

The alloy samples were prepared from elements with very high purity: Al granules with 99.98 % from chemPUR chemicals, Ni in natural isotopic composition from Alfa Aesar as nickel foil, 99.994 % (metals basis) purity. The Ni isotopes as powder were delivered by STB Isotope GmbH, ^{58}Ni with 99.70 % enrichment, and ^{60}Ni with 99.60 % enrichment.

The respective amounts were weighed with high precision scales and the conglomerate of metallic pieces[4] was then melted together by arc melting in an inert Ar gas.

The arc melting apparatus is shown in Fig. 2.6. Between a W needle anode and a Cu cathode, both water-cooled, a high voltage leeds to edge discharge. The resulting plasma arc is used to melt up the different materials. Voltage and current could be adjusted to achieve optimal homogeneity and minimal evaporation. The device was evacuated to the low 10^{-5} mbar region

[4]The Ni isotopes powder was first melted to ingots in a vacuum furnace, with a subsequent melting with B_2O_3 flux treatment to remove oxide impurities.

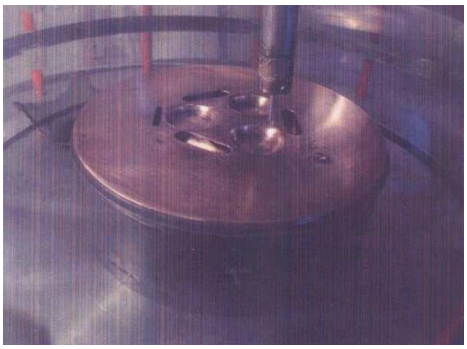

Figure 2.6: Arc melting device used to melt the alloys. The picture shows the neddle W anode and the Cu cathode containing the sample slots.

and flushed with Ar gas. This was repeated several times before the arc melting under Ar gas at about 800 mbar. The metal with highest melting point was positioned on top to further reduce evaporation losses. The ingots were remelted several times to insure homogeneity. The weight was controlled before and after melt-up. Sample slots of different setup were available. The large hollows in the Cu cathode, visible in Fig. 2.6, were used for melting the ingots for the levitation experiments. The resulting pellets were, due to surface tension, already in a processable shape for em. levitation, i.e. roughly spherical with a diameter of about 8 mm.

Also for the container experiments, the alloys were produced within in the arc melting furnace. Afterwards they were crushed to pieces smaller than 1 mm, and subsequently filled in the Al_2O_3 container, see Fig. 3.5, and molten up in the vacuum furnace in several steps. The weight was controlled during the whole processing, losses were in the per mill range.

Chapter 3

Experimental methods

3.1 Neutron Spectroscopy

Due to their typical energies, and correspondingly wavelengths of the order of atomic distances, neutrons are well suited to study the structure of condensed matter. In contrast to X-rays, neutrons are also isotope sensitive. This is due to an intrinsic property of each isotope, the scattering length b (cf. appendix A). Dependent on the natural isotopic mixture of the respective element, the scattering of neutrons also depends on whether we are looking at *coherent* scattering, i.e. scattering as a collective process, stemming from interaction between simultaneously scattered neutrons, or *incoherent* scattering, i.e. scattering from individual atoms. Each element differs in its coherent and incoherent scattering cross section, respectively. (For a detailed discussion, we refer to textbooks like [75], e.g.)

3.1.1 Quasi-elastic Neutron Scattering

The quantity which describes the scattering of the neutrons by a given sample independent of instrumental resolution is the double-differential cross section [85]

$$\frac{\mathrm{d}^2\sigma}{\mathrm{d}\Omega\,\mathrm{d}E_f} = \frac{k_f}{k_i} N \left[\frac{\sigma_{\mathrm{coh}}}{4\pi} S\left(q,\omega\right) + \frac{\sigma_{\mathrm{inc}}}{4\pi} S_{\mathrm{inc}}\left(q,\omega\right) \right] \quad , \tag{3.1}$$

where k_i and k_f are the absolute values of incoming and scattered wave vector, respectively. N is the number of atoms in the beam, Ω the solid angle, and E_f the final energy of the neutron. Without the factor N we get the *normalized* scattering cross section. We have two major parts in Eq. (3.1), the scattering law $S(\mathbf{q},\omega)$, related to coherent scattering, and the incoherent scattering law $S_{inc}(\mathbf{q},\omega)$ which hence relates to incoherent scattering.

They represent the space and time Fourier transforms of correlation functions:

$$S(\mathbf{q},\omega) = \frac{1}{h}\iint G(\mathbf{r},t)\mathrm{e}^{\mathrm{i}(\mathbf{qr}-\omega t)}\,\mathrm{d}\mathbf{r}\,\mathrm{d}t \quad , \tag{3.2}$$

with $G(\mathbf{r},t)$ the pair correlation function, and

$$S_{\mathrm{inc}}(\mathbf{q},\omega) = \frac{1}{h}\iint G_s(\mathbf{r},t)\mathrm{e}^{\mathrm{i}(\mathbf{qr}-\omega t)}\,\mathrm{d}\mathbf{r}\,\mathrm{d}t \quad , \tag{3.3}$$

with $G_s(\mathbf{r},t)$ the self correlation function.

The diffusive motions of particles in liquids now is random with a continuous energy distribution, therefore, the dynamic scattering laws $S(\mathbf{q},\omega)$ and $S_{inc}(\mathbf{q},\omega)$ are centered at zero energy transfer ω. Their characteristic quasi-elastic linewidth is proportional to the diffusivity of the particles.

The wavelengths of the incoming neutrons were chosen such that the scattering from the sample will be dominated by incoherent scattering (from Ni). That is why we will relate the scattering cross section to a parameterization of the incoherent scattering law $S_{inc}(\mathbf{q},\omega)$, see chapter 3.4.3.

3.1.2 Time-of-flight spectroscopy

The experiments were performed on the spectrometer TOFTOF [91] at the Forschungsneutronenquelle Heinz Maier-Leibnitz. A schematic drawing of the instrument is given in Fig. 3.1.

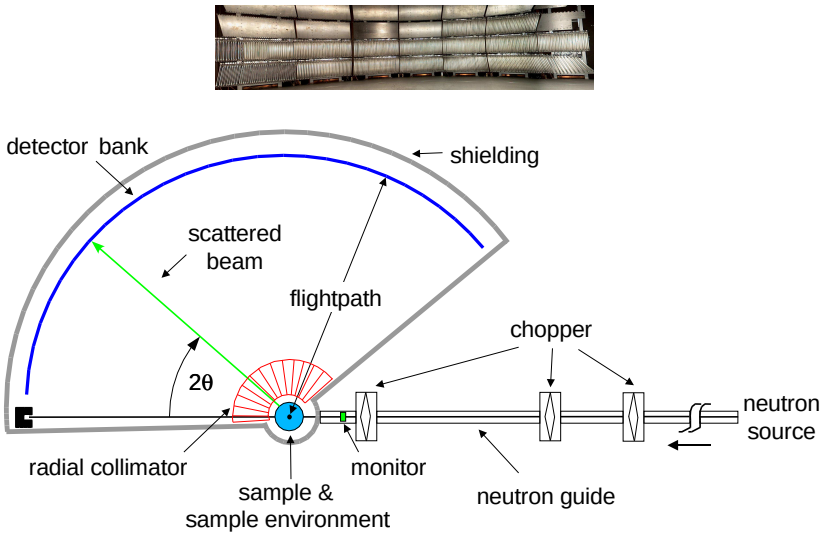

Figure 3.1: Plan of a time-of-flight spectrometer, from [48]. For details, see text.

Out of the neutrons from the reactor, a narrow band of neutrons with given wavelength – and energy – is selected by a chopper system. The incoming flux is measured by the monitor. After that, the neutrons hit the sample with environment and are scattered by the scattering angle 2Θ. After the flight path they hit the shielded detector bank, which is shown on the photograph of Fig. 3.1. A radial collimator ensures that only neutrons from the sample position hit the detector.

The energy of the outgoing neutrons is measured via their flight time from the sample to the detectors and the scattering angle determines the momentum transfer q. The result is the angle dependent intensity as function of time-of-flight. Fig. 3.4 shows such an intensity plot.

After normalizing to vanadium, calculating the energy transfer out of the change in neutron velocity and interpolation to constant q, one ends up with the absolute scattering intensity

$$I(q,\omega) = n_s z_s \int \left(\frac{\mathrm{d}^2\sigma}{\mathrm{d}\Omega \mathrm{d}\omega'}\right)^{\mathrm{norm}} R(q,\omega-\omega')\mathrm{d}\omega', \tag{3.4}$$

where n_s is the number density of scatterers in the sample and z_s the typical path length of neutrons through the sample. The double-differential scattering cross section $\frac{\mathrm{d}^2\sigma}{\mathrm{d}\Omega \mathrm{d}\omega'}$ is convoluted with the energy resolution of the instrument $R(q,\omega)$ to give the measured intensity. The double-differential scattering cross section in turn directly relates to the scattering laws via Eq. 3.1.

Modi operandi

Levitation experiments For the major part of the experiments, we used an incoming wavelength of 5.4 Å. This relates to a maximal (elastic) momentum transfer of about 2.4 $\mathrm{Å}^{-1}$ which is below the first structure factor maximum of the Al-Ni system [18]. This reduces strongly the contribution of coherent scattering, therefore also the amount of multiple scattering. For this wavelength, the energy resolution is approx. 78 μeV. The size of the spherical samples for levitation was approx. 8 mm in diameter. Sample size and sample mass were in some cases adjusted to assure best levitation conditions. The Ni self-diffusion coefficient is then derived from the full width at half maximum of the determined scattering function, in the limit of small momentum transfer q.

Alternatively, a smaller incoming wavelength of 3.8 Å was used to study the effect and contribution of the coherent scattering, including the region of the first structure factor maximum into accessible elastic momentum transfer,

in order to study the influence of topological ordering on the diffusion which is related via coherent scattering.

Typical measurement times were 2 to 3 hours per temperature and sample, depending on the Ni concentration.

Container experiments For the measurements of the dynamic partial structure factors of chapter 5.1, we needed very good statistics. We chose a hollow cylindrical sample geometry, where the alloy is kept in an Al_2O_3 crucible, cf. chapter 3.2.2, with an outer diameter of 22 mm, a wall thickness of 1.2 mm for the alloys with ^{58}Ni and Ni in natural isotopic composition, and 4 mm for the ^{60}Ni alloy. The filling height was 2 to 3 cm, crossing the neutron beam completely.

The measurement times were 24 h per sample at one temperature of 1350 K.

3.2 Sample positioning

3.2.1 Electromagnetic levitation

For an extended measurement range, it is helpful to reduce contacts of the liquid alloy for example with container walls. For instance, these walls act as heterogeneous nucleation seeds, but also chemical reactions do occur at the high temperatures involved, limiting the measurement time, if possible at all. Finally, also the scattering of solid materials interferes with the signal.

The container-free method of electromagnetic levitation [40, 77] is a way to avoid all these hindrances. The absence of the dominant seeds for crystallization enabled an undercooling of several hundred degrees below liquidus, thereby giving the opportunity to do measurements in this important temperature range, see chapter 4.1, e.g. And it was also possible to perform measurements with larger momentum transfer q, where normally the occurring Bragg peaks of the container material strongly disturb the measurement. It was also possible to process materials which are highly reactive, for example Zr [93].

The principle of em. levitation is shown in Fig. 3.2. After positioning the sample in the center of a specially designed water-cooled copper coil and filling the chamber with inert gas (ultrapure He), a rf generator produces a varying magnetic field inside the coils, which induces a current in the metallic alloy. This in turn leads to another magnetic field which by Lorentz' rule creates a force directed towards lower field strength of the initial rf field,

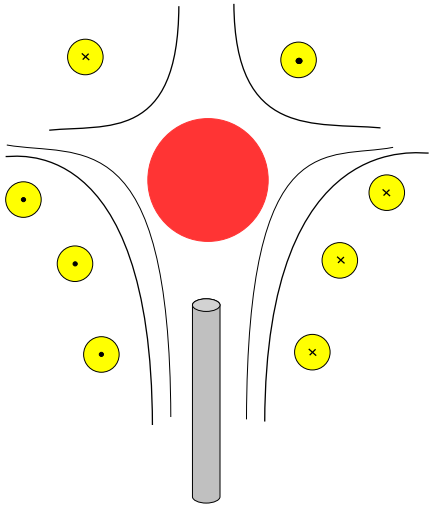

Figure 3.2: Schematic drawing of the electromagnetic levitation working principle. The central sphere symbolizes the metal droplet in the coil whose wires' cross sections are drawn with the appropriate direction of current. The black lines are equipotential lines. Also shown is the position of the cooling gas nozzle.

thereby counteracting gravity. By carefully designing the copper coil, one gets a very stable positioning of the sample. Due to the resistance of the material, the levitation is also connected with a heating of the sample. The temperature is read out using a pyrometer which is gauged by the observed emission plateau at the (known) liquidus temperature. Control of the temperature was achieved by controlled flow of ultrapure He cooling gas through a nozzle below the sample.

In order to make use of all available detector banks at TOFTOF, the coil design of [40] was adjusted to a wider opening (1 cm). For measuring quasi-elastics, it was important to shield the water-containing copper coil. This was done by a B_4C flag before and a Li containing ribbon directly around the coil. A photograph of the actual setup is shown in Fig. 3.3.

The achieved signal-to-noise ratio in the quasi-elastic regime was more than 20, cf. Fig. 3.4.

With our new sample design, the sample could be held stable at a constant temperature for several hours.

3.2.2 Ceramic sample holder

To determine the dynamic partial structure factors of $Al_{80}Ni_{20}$, see chapter 5.1, we used three samples with different Ni isotopic enrichment (see

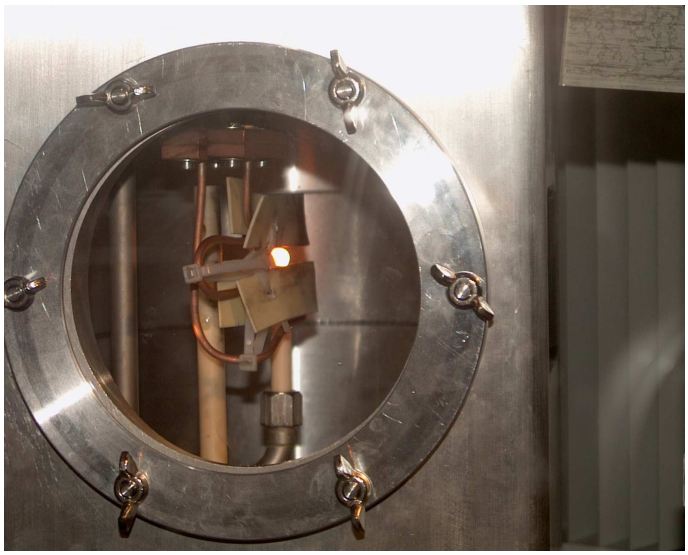

Figure 3.3: Picture of the actual experimental setup. The liquid metal droplet is held against gravity (diameter 7 mm) in the water-cooled copper coil, which are shielded by a Lithium-containing ribbon.

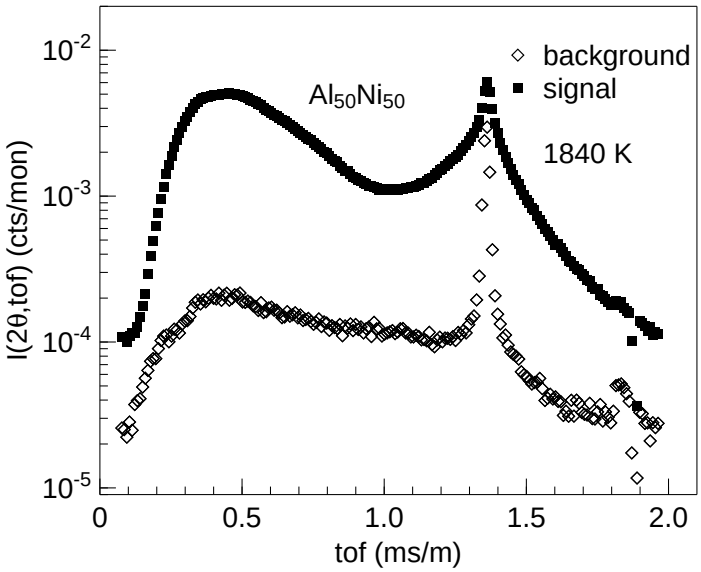

Figure 3.4: Integrated raw intensity over all angles of sample (full squares) and background (open diamonds) for $Al_{50}Ni_{50}$.

chapter 3.3. The focus there was to get data with high precision (24 hour measurement time) at a single temperature above liquidus. Therefore the samples were prepared in hollow cylindrical geometry in an Al_2O_3 crucible, shown in Fig. 3.5. The resulting hollow sample cylinder has a wall thickness of 1.2 mm and an outer diameter of 22 mm for the case of natural Ni and ^{58}Ni

Figure 3.5: Crucible consisting of two Al_2O_3 cylinders, resulting in a sample geometry of a hollow cylinder with an outer diameter of 22 mm and a wall thickness of 1.2 mm.

enrichment. For the ^{60}Ni sample, a crucible with the same outer diameter, but 4 mm wall thickness was used, to compensate for the weaker scattering of ^{60}Ni.

The achieved signal-to-noise ratio in the quasi-elastic regime for the container experiments with Ni in natural isotopic composition and ^{58}Ni was about two orders of magnitude, cf. Fig. 3.6 a). For the sample with enriched

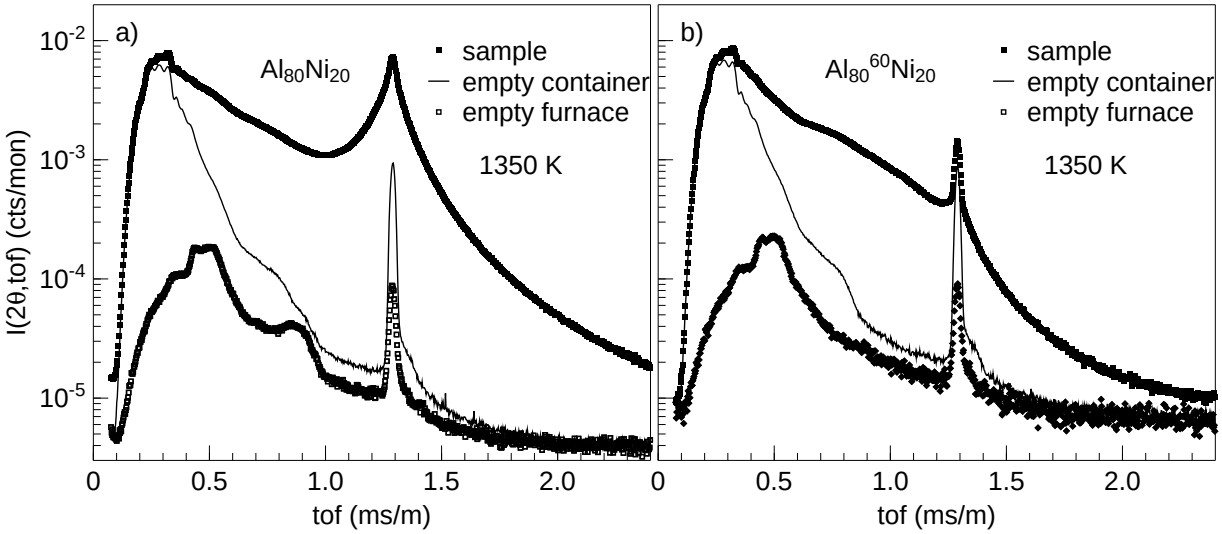

Figure 3.6: Integrated raw intensity over all angles of sample (full squares), empty Al_2O_3 container (line), and background of empty furnace (open squares) for $Al_{80}Ni_{20}$ with natural isotopic composition (a) and ^{60}Ni (b).

^{60}Ni, the signal-to-noise ratio is still more than a factor of 10 (Fig. 3.6 b).

As we need high statistics to determine the partial structure factors, and ^{60}Ni is a weak scatterer, we measured each isotope sample for 24 h.

3.3 Isotopic Substitution

To determine all three quasi-elastic partial structure factors of a binary liquid – the self-correlations of both constituents and the cross-correlation –, one has to perform three measurements with differing scattering lengths. This can be either achieved by varying the techniques, a combination of neutron and X-ray scattering, e.g. [90], or with the same technique, i.e. neutron scattering, on three samples with identical chemical composition but differing scattering length due to different isotopic enrichment. For the alloy systems of this work, Ni is the element of choice for different isotopic enrichment. Ni in natural isotopic composition is as mentioned already a strong incoherent scatterer. The major isotope, ^{58}Ni, is a strong and pure coherent scatterer. As third isotopic variation, we decided for ^{60}Ni, which also scatters purely coherent, but even weaker than Al. So scattering from Al really plays a role when measuring Al-^{60}Ni alloys. Table 3.1 shows the respective scattering cross sections of the used Ni isotopic compositions, compare also the listing in appendix A.

Table 3.1: Coherent and incoherent scattering lengths of the used Ni isotopes. All data from [78].

	^{58}Ni	^{60}Ni	$^{\mathrm{na}}$Ni
σ_{coh}[barn]	26.1	0.99	13.3
σ_{inc}[barn]	0	0	5.2

3.4 Data analysis

3.4.1 Raw data reduction

determination of temperature The sample temperature was read out using a pyrometer. The emissivity of the sample was gauged during heating-up, the plateau in the time-temperature curve corresponding to the liquidus temperature of the alloy, taken from the known phase diagram [56]. The read-out temperature can then be converted to the actual temperature, using the equation

$$\frac{1}{T_{\mathrm{real}}} = \frac{1}{T_{\mathrm{meas}}} - \frac{1}{T^L_{\mathrm{meas}}} + \frac{1}{T^L_{\mathrm{real}}} \quad , \tag{3.5}$$

where T^L stands for the liquidus temperature, and real and meas for the real and the measured temperature, respectively. All temperatures in Eq. 3.5 are inserted in units of Kelvin.

The data was then read in and analyzed using the software FRIDA-1 (*Fast Reliable Interactive Data Analysis*) [95]. For each sample in addition to the temperature runs, a Vanadium measurement at room temperature and a background scan were taken. All measurements were normalized to monitor counts, sample and background signal were then normalized to the Vanadium measurement, to correct for differences in detector efficiency. The resulting raw data is $I(2\Theta, tof)$, with 2Θ the scattering angle and tof the time of flight, cf. Fig. 3.4.

These raw data are then transformed to the scattering function $S(2\Theta, \omega)$ by firstly deriving the energy transfer ω from tof

$$\hbar\omega = \frac{1}{2}m_n\left(\frac{1}{tof_{\mathrm{el}}}\right)^2 - \frac{1}{2}m_n\left(\frac{1}{tof}\right)^2 \quad , \tag{3.6}$$

with m_n the neutron mass, and tof_{el} the time of flight (inverse velocity) for incoming neutrons.

The measured intensity is proportional to the double differential cross section and the scattering law

$$I(2\Theta, tof) \propto \frac{\partial^2\sigma}{\partial\Omega\partial tof}\frac{\partial tof}{\partial\omega} \propto A\frac{k_f}{k_i}S(q,\omega) \quad . \tag{3.7}$$

k_f also depends on the time of flight. In total, we get a tof^4-dependence that becomes more pronounced upon approaching the energy loss side of the spectrum,

$$S(2\Theta, \omega) \propto \frac{\partial^2\sigma}{\partial\Omega\partial\omega} \cdot tof^4 \quad . \tag{3.8}$$

When measuring with a sample container, the next analysis step will be self-absorption correction, see next section. For container-free measurements, we directly interpolate the angle 2Θ to constant q, correct for detector efficiency, and get the scattering law $S(q, \omega)$.[1]

We derived the scattering law for the pure sample signal, and the sample signal minus full background. The Fourier transform in time space of the scattering law leads us to the intermediate scattering function of Eq. (2.10), which basically is the exponential decay of the Ni self correlation. So for

[1] To be precise, this is only the absolute scattering law, when the scattering length density of the sample is the same as that of the vanadium used for the normalization, see chapter 3.4.5. One chooses a Vanadium shape close to the sample geometry to get a similar resolution.

large times (several tens of ps), $S(q,t)$ should go to 0. Fig. 3.7 shows the intermediate scattering functions of a pure sample signal and one with 100% background subtraction. One can see that no subtraction of background

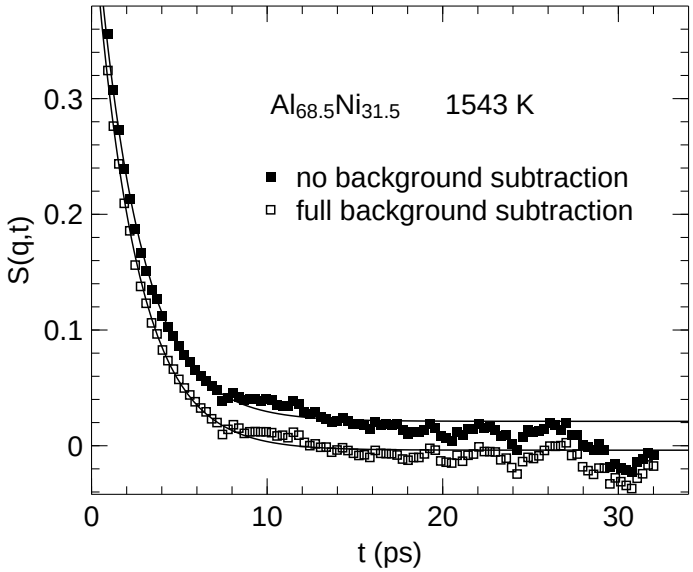

Figure 3.7: Intermediary scattering function (for $Al_{68.5}Ni_{31.5}$). The full squares show raw data without subtraction of background. The open squares are with 100% background subtraction. The lines are exponential fits to the data.

leads to a positive residual value of $S(q,t)$ for large decay times, whereas the full subtraction of the empty chamber measurement overestimates the background intensity, leading to a negative value for large t. This is because a present sample reduces the incoming flux on the Lithium covering of the coils (the dominant scatterer for background) by scattering and absorption. Nevertheless, both cases result in a similar exponential parameter ($0.40\,\mathrm{ps}^{-1}$ without background subtraction and $0.41\,\mathrm{ps}^{-1}$ with full background subtraction). So after an optimal background treatment, we would want $S(q,t)$ to decay exactly to zero. From this consideration, we evaluate a multiplication factor for the background, of the order of 0.7, before subtracting it from the raw spectra. The exact value of this correction factor has no strong influence on the derived relaxation times or diffusion coefficients, due to the low intensity of the background, cf. Fig. 3.4.

The resulting scattering laws $S(q,\omega)$ can then be fitted with scaled Lorentzians, as described in the next but one subsection.

3.4.2 Self-absorption correction

To correctly treat an empty container measurement, one has to consider the effects of self-absorption. The measured intensity and hence also the scattering law $S(q,\omega)$ comprise scattering contributions of the sample (I_S) and of the container (I_C) which are not simply additive. So it is not possible, to simply subtract the scattering signal of the container from the combined scattering I_{SC}. Especially for quasi-elastic measurements it is important to do a careful analysis, because the contribution of self-absorption is asymmetric, as slower neutrons have an increased residence time in the sample and hence show an increased probability to get absorbed. In order to get a symmetrised scattering law, self-absorption correction is even more important than the detailed balance factor[2].

Following Paalman and Pings [71], we can resolve the contribution of self-absorption using

$$I_S(\mathbf{q},\omega) = \frac{1}{A_{S,SC}(\mathbf{q},\omega)} I_{S+C}(\mathbf{q},\omega) - \frac{A_{C,SC}(\mathbf{q},\omega)}{A_{S,SC}(\mathbf{q},\omega) A_{C,C}(\mathbf{q},\omega)} I_C(\mathbf{q},\omega) \quad , \tag{3.9}$$

where the A's are absorption factors for the container (C) and sample (SC). The first index denotes the scattering part, the second one the absorption part, see [71] for details.

3.4.3 Scattering Law

If we assume ideal incoherent scattering, the scattering law for the diffusion of Ni in the melt, in the hydrodynamic regime of low momentum transfer q, can be described using Eq. (2.11):

$$S_{inc}(q,\omega) = \frac{A}{\pi\hbar} \frac{Dq^2}{\left(Dq^2\right)^2 + \omega^2} + b_q, \tag{3.10}$$

a Lorentzian with D the self-diffusion coefficient of Ni, the dominant incoherent scattering contributor, A a proportionality factor, containing, amongst others, number density of scatterers and typical path length of neutrons through the sample, and b_q a (q-dependent) background which accounts for contributions of Debye level, among other things, that are assumed constant in the fitting range.

[2]The process of neutron energy loss and of neutron energy gain are not equally probable. Therefore, it depends on temperature, $S(q,-\omega) = \exp(-\hbar\omega/k_BT)S(q,\omega)$. At high temperatures, the detailed balance factor imposes only minor corrections to the scattering law.

For principal reasons, we allow for $D(q)$ to be dependent on momentum transfer q, for more on that see chapter 3.4.4. This $D(q)$ will be our key to the dynamics and the description of the transport mechanism.

Fig. 3.8 shows the measured scattering law $S(q,\omega)$ for $Al_{68.5}Ni_{31.5}$, as a function of temperature and momentum transfer q, respectively. Please note the semi-logarithmic presentation.

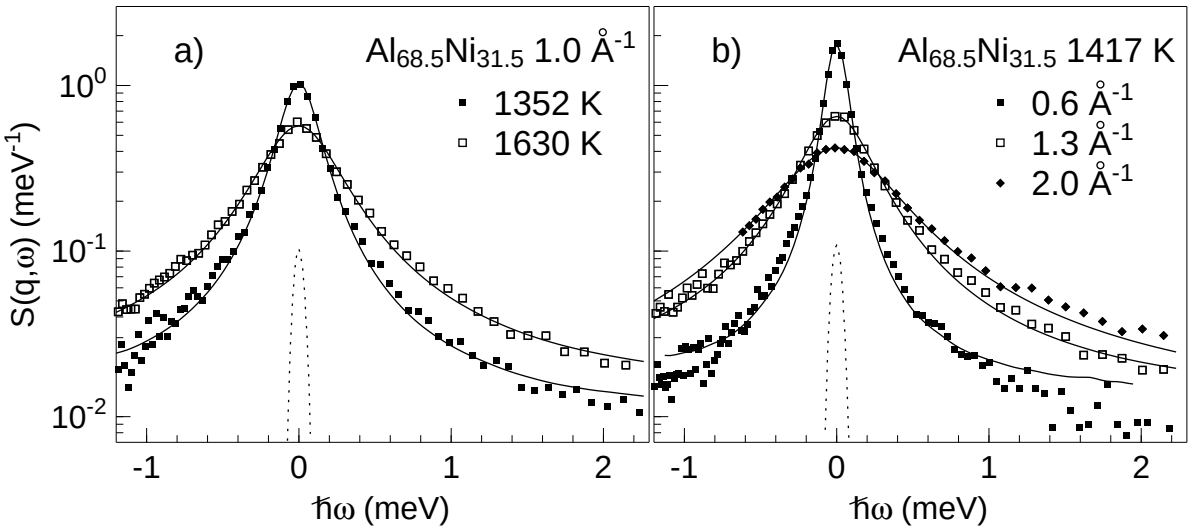

Figure 3.8: Scattering law $S(q,\omega)$ of liquid $Al_{68.5}Ni_{31.5}$: (a) at fixed momentum transfer q for two different temperatures; 270 K below liquidus temperature [T_{liq} = 1623 K] (filled squares) and above melting point (open squares), (b) at 1417 K (undercooled) for three q values, 0.6 $Å^{-1}$, 1.3 $Å^{-1}$ and 2.0 $Å^{-1}$, respectively. The lines are fits with a Lorentz function that is convoluted with the instrumental energy resolution shown as dashed line.

We find a broadening of the quasielastic line with increasing temperature (fig. 3.8 a) and increasing momentum transfer q (fig. 3.8 b), respectively.

3.4.4 q-dependent diffusivity

Under the assumption of dominant incoherent scattering and in the hydrodynamic regime, D of Eq. (3.10) is a constant, as in Eq. (2.9). From this we will derive the self-diffusion.

To study the processes at higher q outside the hydrodynamic limit, we define an effective q-dependent diffusivity

$$D(q) = \frac{\Gamma_{1/2}(q)}{\hbar q^2} \quad . \tag{3.11}$$

For ideally incoherent scattering, $\Gamma_{1/2}(q) = \hbar D_c q^2$, with D_c constant. Then, Eq. (3.11) just gives this constant.

3.4.5 Data Normalization

In order to derive from the scattering data for various isotopic enrichments the partial structure factors, we have to choose the correct normalization to number density of scatterers, geometry and scattering length. As the multiplication of factors has no influence on the linewidth, this detailed treatment was not necessary for deriving the diffusivity, but is now as we have to consider the interaction of the different scattering lengths in the matrix inversion to come. In the first step of deriving the partial static structure factors, we follow the steps given in [24], but also taking into account incoherent scattering from Ni in natural isotopic composition.

The data treatment using FRIDA-1 (cf. chapter 3.4.3) results in a scattering function $S^*(q,\omega)$, which is not yet normalized exactly. Assuming a Lorentzian shape, we get the respective structure factor $S^*(q) = \int S^*(q,\omega)\mathrm{d}\omega$ just using the properties of a scaled Lorentzian:

$$S^*(q) = \frac{a\pi}{\Gamma_{1/2}} \quad , \tag{3.12}$$

where a is the amplitude and $\Gamma_{1/2}$ the HWHM of the Lorentzian.

This $S^*(q)$ corresponds to a normalized intensity,

$$S^*(q) = \frac{I^{norm}}{I_V^{norm}} \quad , \tag{3.13}$$

where the index V stands for vanadium.

To get the differential scattering cross section, we need to consider the number of scattering atoms in the sample, N_S, and in vanadium, N_V, respectively. Together with the incoherent scattering length of ^{51}V, we get

$$\left(\frac{\mathrm{d}\sigma}{\mathrm{d}\Omega}\right)^{norm} = S^*(q) \cdot \frac{N_V}{N_S} b_{inc,V}^2 \quad . \tag{3.14}$$

Assuming equal scattering areas for the vanadium and our samples, we can write this as

$$\left(\frac{\mathrm{d}\sigma}{\mathrm{d}\Omega}\right)^{norm} = S^*(q) \cdot \frac{n_V}{n_S} \cdot \frac{z_V}{z_S} \cdot \frac{\sigma_{inc}^V}{4\pi} \quad . \tag{3.15}$$

Here n is the scattering density and z is the flight path of the neutrons through the sample or vanadium. For our geometry of hollow cylinders, $z = \pi d$, with d the wall thickness of the hollow cylinder.

The total structure factor $F(q)$ can be derived by subtracting all constant contributions

$$\Delta = \Delta_{coh} + \Delta_{inc} + \Delta_{mult.scat.} \quad , \tag{3.16}$$

with $\Delta_{coh} = c_A b_A^2 + c_B b_B^2$ the coherent contribution, and Δ_{inc} and $\Delta_{mult.scat.}$ the isotropic contributions from incoherent and multiple scattering, respectively:

$$F(q) = \left(\frac{\mathrm{d}\sigma}{\mathrm{d}\Omega}\right)^{norm} - \Delta \approx \left(\frac{\mathrm{d}\sigma}{\mathrm{d}\Omega}\right)^{norm} - \frac{\sigma_{tot}}{4\pi} \quad . \tag{3.17}$$

The relation between total and partial structure factors is given by

$$F(q) = c_A^2 b_A^2 \left(S_{AA} - 1\right) + c_B^2 b_B^2 \left(S_{BB} - 1\right) + 2 c_A c_B b_A b_B \left(S_{AB} - 1\right) \quad . \tag{3.18}$$

To derive the three unknown partial structure factors (of a binary alloy), we therefore need three measurements with varying b's, and then solve this set of three equations.[3] The resulting static partial structure factors for $Al_{80}Ni_{20}$ at 1350 K are plotted in Fig. 5.6.

For the static structure factor $S(q)$, there exist (at least) two types of notation. This is because one has several options to scale $\left(\frac{\mathrm{d}\sigma}{\mathrm{d}\Omega}\right)^{norm}$. In the so-called Faber-Ziman formalism [25], we scale the total structure factor $F(q)$ by the average (coherent) scattering lengths squared,

$$I(q) = 1 + \frac{F(q)}{\langle b \rangle^2} \quad , \tag{3.19}$$

where we used the letter I according to [60] to clarify the use of Faber-Ziman structure factors.

In Bhatia-Thornton notation [6], the normalized differential scattering cross section is scaled by the average of the square of the (coherent) scattering lengths,

$$S(q) = \frac{1}{\langle b^2 \rangle} \left(\frac{\mathrm{d}\sigma}{\mathrm{d}\Omega}\right)^{norm} \quad . \tag{3.20}$$

Both static structure factors have the same large q limit

$$\lim_{q \to \infty} \begin{matrix} I \\ S \end{matrix} (q) = 1 \quad , \tag{3.21}$$

and show similar oscillations, but different amplitudes. See Fig. 5.5 and 5.7 for the examples of our measurements.

[3] For a nice and detailed description, see [24] and [88].

The relation between Faber-Ziman and Bhatia-Thornton structure factors is given by [6]

$$S_{NN}(q) = c_{Al}^2 S_{AlAl}(q) + c_{Ni}^2 S_{NiNi}(q) + 2c_{Al}c_{Ni}S_{AlNi}(q) \quad , \tag{3.22}$$

$$S_{CC}(q) = c_{Al}c_{Ni}\left[1 + c_{Al}c_{Ni}\left(S_{AlAl}(q) + S_{NiNi}(q) - 2S_{AlNi}(q)\right)\right] \quad , \tag{3.23}$$

$$S_{NC}(q) = c_{Al}c_{Ni}\left[c_{Al}\left(S_{AlAl}(q) - S_{AlNi}(q)\right) - c_{Ni}\left(S_{NiNi}(q) - S_{AlNi}(q)\right)\right] . \tag{3.24}$$

Chapter 4

Diffusion Dynamics

4.1 Liquid metal Ni

In order to demonstrate the outcome of the previous data analysis, we will first focus on pure Ni[1]. This will also be a proof of the feasibility of our approach.

We use the Lorentzian fits of Eq. (3.10) to analyse the scattering laws $S(q, \omega)$. The half width at half maximum (HWHM) should, according to that equation, be proportional to q^2. A plot of $\Gamma_{1/2}$ vs. q^2 is given in Fig. 4.1.

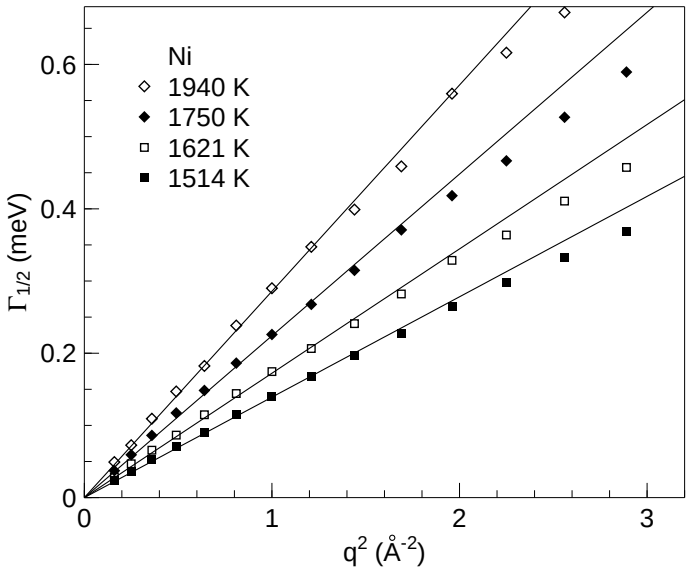

Figure 4.1: HWHM vs. q^2 for various temperatures for levitated Ni, derived from the scattering law $S(q, \omega)$.

[1]These results are published in [67].

Up to momentum transfers of $1.2\,\text{Å}^{-1}$ ($q^2 = 1.4\,\text{Å}^{-2}$), the HWHM shows a clear q^2 dependence. This also means that $D(q)$ of Eq. (3.11) is constant for up to $q = 1.2\,\text{Å}^{-1}$. Only for larger q, there is a deviation to smaller linewidth.

For larger values of the momentum transfer, Eq. (3.10) still can describe the data accurately, but the interpretation is more demanding. Firstly because this q range does not correspond any more to the hydrodynamic regime of low momentum transfer, and secondly, coherent scattering of Ni becomes relevant when q values approach the structure factor maximum[2].

The value of the Ni self-diffusion coefficients can be derived from the slope of $\Gamma_{1/2}(q^2)$ in the region of low momentum transfer q up to $1.2\,\text{Å}^{-1}$, following Eq. (3.11)

$$D = \frac{\Gamma_{1/2}}{\hbar q^2} \quad .$$

Arrhenius law The resulting Ni self-diffusion coefficients vs. $1/T$ are plotted in Fig. 4.2. Over a large temperature range – from more than 200 K above

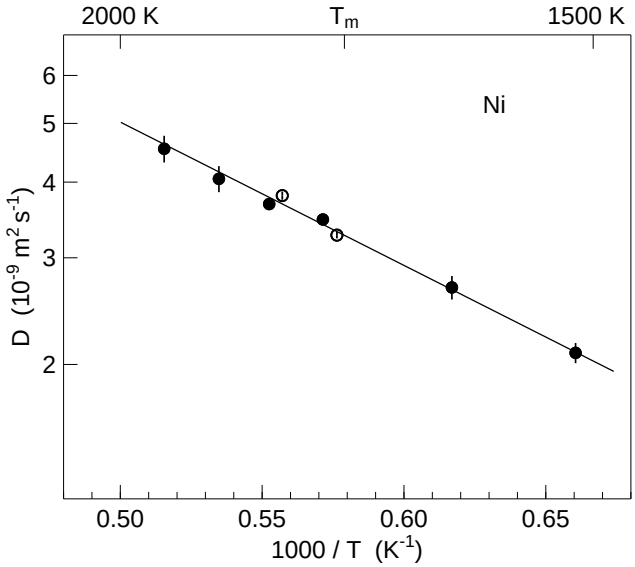

Figure 4.2: Temperature dependence of Ni self-diffusion coefficients. The line is a fit with Eq. (4.1). Full circles show our levitation data, the open circles are from [16, 17].

to more than 200 K below the melting point of 1727 K – the temperature dependence of the diffusion coefficients in Ni can be described by an Arrhenius law,

[2]See chapter 5.2 for details on the influence of the structure factor on the diffusivity.

$$D = D_0 \exp\left(-E_A/k_B\,T\right), \tag{4.1}$$

with an activation energy $E_A = 0.47 \pm 0.03\,\mathrm{eV}$ per atom, and the prefactor, containing the temperature independent contributions of change of entropy, coordination number, etc. [79], $D_0 = 77 \pm 8 \times 10^{-9}\,\mathrm{m^2/s}$.

Influence of undercooling This temperature dependence also shows that the change from a liquid in thermodynamical equilibrium to a metastable liquid at temperatures below the melting point is not reflected in its atomic dynamics [67]. So by undercooling, the diffusion gets slower, according to the Arrhenius law (4.1), but stays qualitatively the same activated process.

Diffusion mechanism The Arrhenius behavior observed for liquid Ni differs from the T^2 behavior reported for metallic melts with lower packing density such as Sn, Pb, In and Sb [46, 63]. A comparison is shown in Fig. 4.3. The data clearly indicates that the diffusion is an activated process follow-

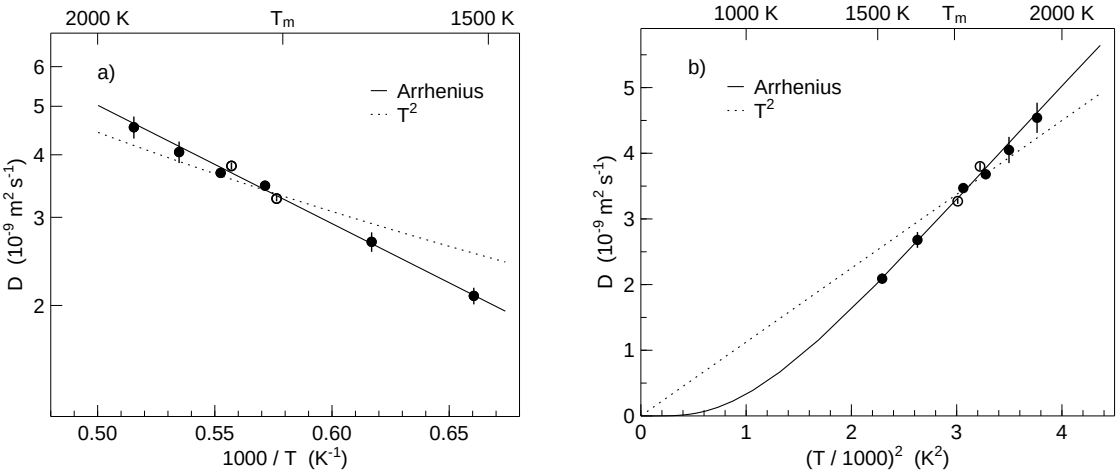

Figure 4.3: D as function of $1/T$ (left picture) and of T^2 (right picture). The straight line is a fit using Arrhenius' law (4.1), the dotted line follows a T^2 law.

ing an Arrhenius law 4.1, and not T^2 scaling. However, a definite distinction between Arrhenius and T^2 is only possible with data obtained from the metastable state of the undercooled melt.

Consistency of approach Fig. 4.2 also contains data of [16, 17], from a completely different setup. In [16, 17], the Ni was filled into Al_2O_3 containers, resulting in a hollow cylindrical geometry with a wall thickness of 1.2 mm. In

this way, multiple scattering from Ni was minimized, while exploiting the full beam size, thus enhancing intensity. In our geometry of spherical Ni with 8 mm diameter, multiple scattering might play a more important role and influence the determination of the self-diffusion coefficient unfavorably. Also pure Ni scatters more strongly than all the other Al-Ni alloys. But the perfect agreement between the data derived using em. levitated samples and the data from container experiments shows that multiple scattering (observable for $q < 0.5\,\text{Å}^{-1}$), does not interfere with the determination of the Ni self-diffusion coefficient.

4.2 Binary liquid Al-Ni alloys

The main focus of our work were liquid alloys, as the diffusion or more generally the question of material transport in the liquid alloy is of major interest in alloy formation. We focused our studies on Al-Ni, because for this system, there exist reliable simulations with detailed predictions of diffusion coefficients [19], and also a series of data in a limited temperature and q range.

Al-Ni shows CSRO over a broad compositional range, as detailed in chapter 2.1.

A recent QENS study on Al-Ni melts above liquidus [18] studied how mass transport is affected by CSRO. The diffusion coefficient was practically the same for $Al_{25}Ni_{75}$ as for pure Ni. Only for Al concentrations of 62 at.% and higher, the diffusion significantly increased. However, it was not possible yet to measure diffusion coefficients for the complete compositional range.

In combination with MD simulation, the features of the experiments were explained as follows. In the Ni-rich system, the added Al atoms take Ni positions, so that the distance between repeated Al-Al units corresponds to that of repeated Ni-Ni units. This works up to about 50 at.% of Al. Then, simulation shows that the distance between repeated Al-Al units becomes larger without significantly influencing the Ni-Ni distances. So packing fraction goes down, and the Ni self-diffusion increases strongly for the Al-rich alloys. This explanation was derived from the modeled partial structure factors. For measurements of static and dynamic partial structure factors, see the next chapter 5.1 of this work.

In the binary Al-Ni system, the mass transport seems to be dominated by the packing fraction [18], yet one should also check for possible influences of the underlying phase diagram. Most simulations rely on a temperature independent diffusion coefficient for the mass transport during solidification, with a value derived from capillary diffusion measurements at best, though

the process in reality works out of the metastable undercooled liquid state, where no value of the diffusion coefficient has been measured yet.

Previously, the study of dynamics in the metallic melt using neutron scattering was hindered by the demands of containing the liquid metal, thus reducing the accessible temperature range and also limiting the experiments to less active alloy systems. Thus, the work of Reference [18], e.g., was performed using alumina crucibles to contain the melt. This limits the accessible temperature and q (due to unwanted scattering from containers) range and prevents undercooling.

As with our em. levitation technique, there are no nucleation seeds from container walls, this technique allows to undercool the metallic melts by several hundred degrees. As compared to the work of Ref. [18], we are thus able to discuss the concentration and temperature dependence of the Ni self diffusion in the complete compositional domain. Fig. 4.4 shows the Al-Ni phase diagram. The blue dots mark the temperatures and compositions

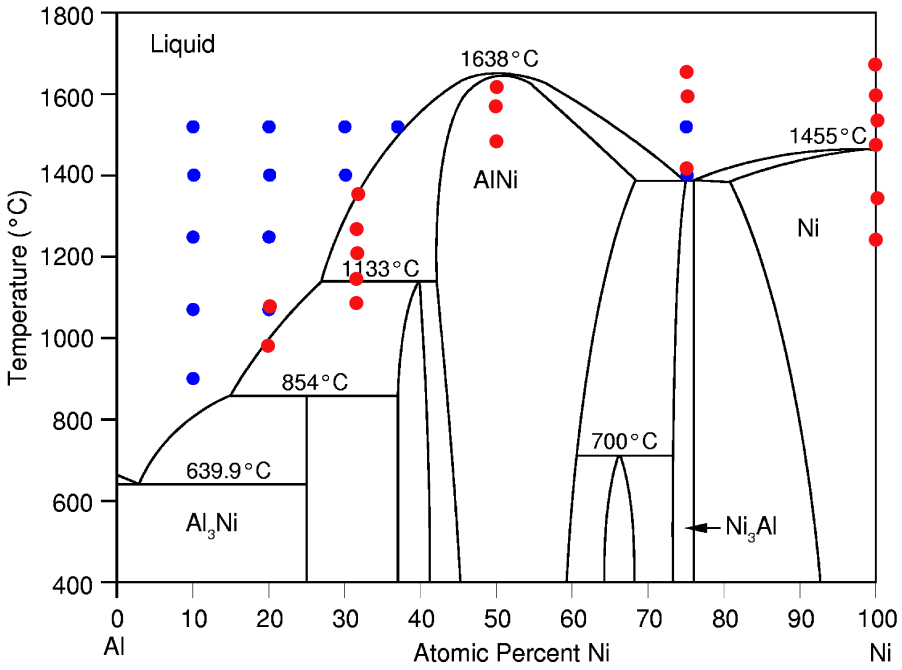

Figure 4.4: Al-Ni phase diagram. Blue dots mark the container measurements of [16, 18]. Red dots show the levitation measurements of this work.

studied by [16, 18] in an Al_2O_3 crucible. In red are given the experiments using em. levitation.

The $Al_{50}Ni_{50}$ intermetallic compound with the highest liquidus of 1940 K is of particular interest, to see whether this large liquidus temperature is

reflected in the dynamics of the melt. To get diffusion data at various temperatures for this alloy is demanding as temperatures are high.

The simulation of Das et al. [18] predicts a strong increase of the Ni self-diffusion with increasing Al content for Al-rich alloys. For medium to low Al content, the Ni self-diffusion coefficients are fairly constant with a slower increase towards the Ni rich side by about 10 %. In contrast, the experiments of [18] show a decrease (with increasing Ni content) or at least constant value for the Ni self-diffusion coefficient for the Ni-rich alloys. This will be studied in more detail, to see whether the dynamics is really constant in the Ni-rich Al-Ni alloys and to determine the composition at which the dynamics do change. In addition to the determination of the Ni self-diffusion coefficients on an absolute scale with small error, we will also track the q dependent dynamics from small q values of about $0.5\,\text{Å}^{-1}$ up to typical momentum transfers of the first structure maximum around $3\,\text{Å}^{-1}$ by means of an effective diffusivity $D(q)$. The absence of any solid container material is the precondition for an extensive study of the q dependence, otherwise the Bragg peaks of the container material will render large regions of $S(q,\omega)$ inaccessible. Another important question is whether the dynamics of the metallic melt are changed qualitatively upon undercooling when the system becomes metastable.

In addition to the intermetallic $Al_{50}Ni_{50}$, we studied an alloy of the Ni-rich side ($Al_{25}Ni_{75}$) and an Al-rich one ($Al_{80}Ni_{20}$). For the binary alloy $Al_{80}Ni_{20}$, we could compare our EML results with data from container experiments [16, 17], in order to assure the applicability of the combination of EML with QENS to derive diffusion coefficients with high precision. Due to a different sample geometry (spheres of 8 mm diameter instead of hollow cylinders with 1 mm wall thickness), the total number of scatterers in our case is higher, and multiple scattering could play a larger role. But the results clearly indicate that multiple scattering is still weak enough not to interfere with the determination of temperature and concentration dependent diffusion coefficients with a high precision.

4.2.1 Temperature dependence

We studied alloys of the Al-Ni system with varying Ni content: 20 at. %, 50 at. % and 75 at. %, and also 50 weight % Ni (corresponding to 31.5 at. % Ni). Each sample was prepared as detailed in section 2.3. The spherical ingots had diameters of about 8 mm, somewhat tuned to alloy specifics as melting point or conductivity. The derived Ni self-diffusion coefficients are listed in table 4.1.

In Fig. 4.5, these diffusion coefficients are plotted as function of the inverse

Table 4.1: Ni self-diffusion coefficients derived from the quasi-elastic line width for various Al-Ni compounds. The temperature is ± 5 K.

alloy	T_{liq} [K]	T [K]	D [$10^{-9}\,m^2s^{-1}$] this work	D [$10^{-9}\,m^2s^{-1}$] crucible [16, 17]	E_A [eV per atom]	D_0 [$10^{-9}\,m^2s^{-1}$]
$Al_{25}Ni_{75}$	1658	1670		3.05 ± 0.17	0.465 ± 0.027	78 ± 13
		1689	3.22 ± 0.08			
		1795		3.95 ± 0.10		
		1868	4.35 ± 0.05			
		1928	4.90 ± 0.20			
$Al_{50}Ni_{50}$	1940	1758	3.7 ± 0.3		0.42 ± 0.06	60 ± 22
		1840	4.35 ± 0.17			
		1892	4.59 ± 0.11			
$Al_{68.5}Ni_{31.5}$	1613	1352	1.83 ± 0.03		0.563 ± 0.025	230 ± 50
		1417	2.29 ± 0.10			
		1484	2.87 ± 0.04			
		1543	3.28 ± 0.13			
		1630	4.03 ± 0.18			
$Al_{80}Ni_{20}$	1245	1259	2.91 ± 0.09		0.376 ± 0.018	100 ± 14
		1350	3.93 ± 0.14	4.02 ± 0.06		
		1525		5.71 ± 0.07		
		1670		7.30 ± 0.08		
		1795		8.74 ± 0.09		

temperature.

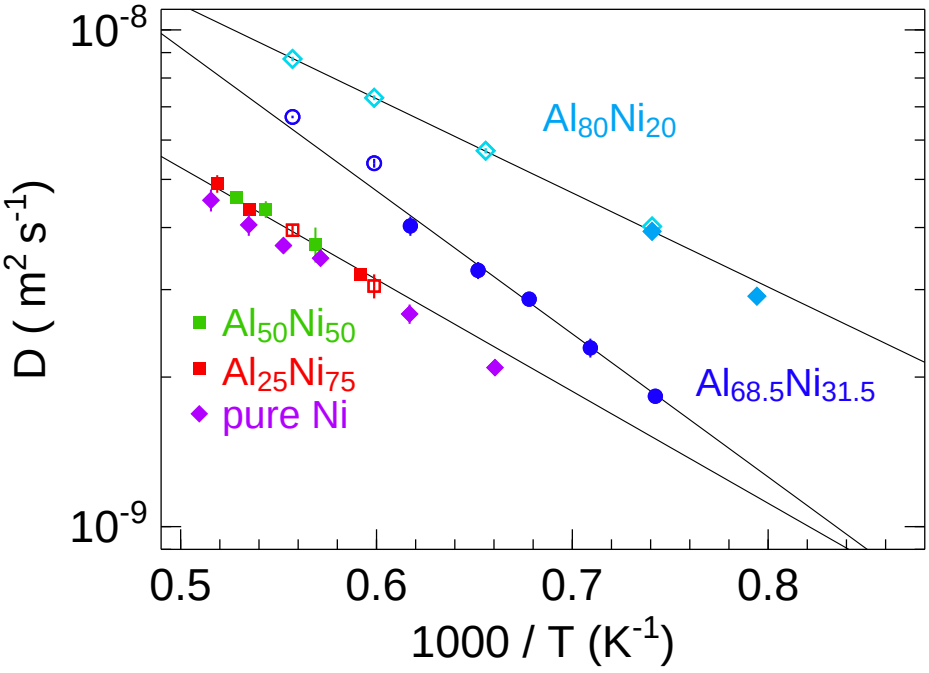

Figure 4.5: Derived Ni self-diffusion coefficients in Al-Ni melts as function of inverse temperature. Open symbols show data from previous container experiments [16, 17]. Lines are fits to an Arrhenius law.

For all alloys, the temperature dependence of the Ni self-diffusion coefficient can be described by an Arrhenius law (4.1), the resulting activation energies are also given in table 4.1.

What one can see is that for Ni rich alloys of the Al-Ni system, the Ni self diffusion is practically independent of Al content, up to an aluminum content of 50 at. %. It is also remarkable that – though the measurements of the Ni rich alloys are all in the same absolute temperature range – the liquidus temperatures of these alloys are quite different, 1940 K for $Al_{50}Ni_{50}$, 1658 K for $Al_{25}Ni_{75}$ and 1726 K for pure Ni. Correspondingly, the data represent diffusion in an undercooled melt in a metastable state for $Al_{50}Ni_{50}$, whereas in $Al_{25}Ni_{75}$, diffusion was measured well above liquidus in the stable melt. The pure Ni data show measurements in both states. No qualitative nor quantitative change can be found for the Ni self diffusion in the metastable state. Neither in the q-dependent quasi-elastic line width nor in the derived diffusion constants was there any indication of a change of dynamics at the liquidus temperature.

For alloys with Al content higher than 50 at. %, we see an increase in Ni diffusion. Noticeable is the very high activation energy found for the alloy

$Al_{68.5}Ni_{31.5}$, 0.56 eV/atom. We performed also additional container experiments with $Al_{68.5}Ni_{31.5}$ (open circles in Fig. 4.5). Unfortunately we could not measure to higher temperatures due to the failing of the container. Also the levitation experiment could not be repeated yet. To study this interesting point in more detail, additional experiments should be performed for this composition.

For the compound $Al_{80}Ni_{20}$, we see an increase in Ni diffusion. We could not achieve undercooling, but we measured the diffusion coefficient at the same temperature as was done in a previous crucible experiment [17], resulting in the same diffusion coefficient. This is a verification of our new approach, proofing that multiple scattering is not foreclosing our measurements.

4.2.2 Concentration dependence

We will now look at the concentration dependence of Ni self diffusion at a constant temperature. This is shown in Fig. 4.6.

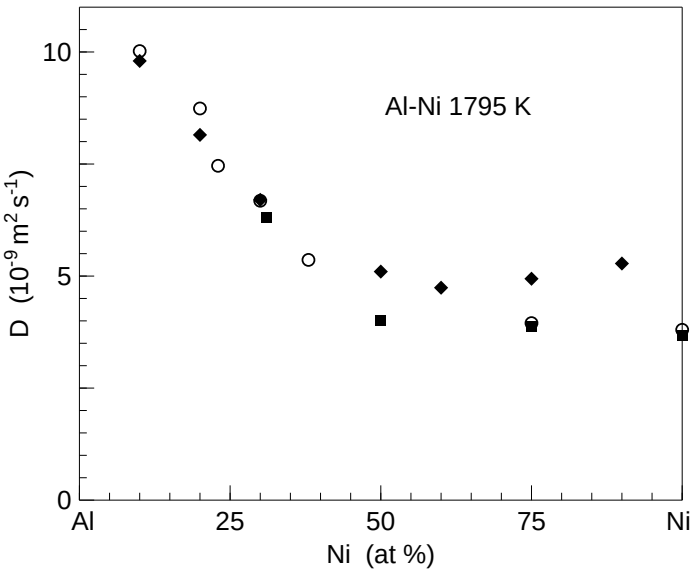

Figure 4.6: Ni self-diffusion coefficients in Al-Ni as function of composition at 1795 K.

Coming from the Ni-rich side, one sees that the addition of Al does not change the diffusion constant up to values of 50 at. % Al. After that, further addition of Al will increase diffusion drastically. This can be understood when we consider that the density of the Al-Ni alloy at fixed temperature is reduced (non-linearly) by adding of Al; also the packing fraction goes down and therefore diffusion increases. In other words, only for a high Al

concentration are the aluminum atoms changing the structure, before they are just sitting on Ni sites. So this is merely a case where packing fraction governs mass transport [18] and no dependence on thermodynamic properties as liquidus temperature, e. g., is observed.

One could expect, especially in the intermetallic systems, a correlation between crystal and liquid order. To check for possible relations of the diffusion to the phase diagram, we look at the concentration dependence of the Ni self-diffusion coefficient of the studied Al-Ni alloys at their respective liquidus temperature, extrapolated using Eq. (4.1). This is shown in Fig. 4.7.

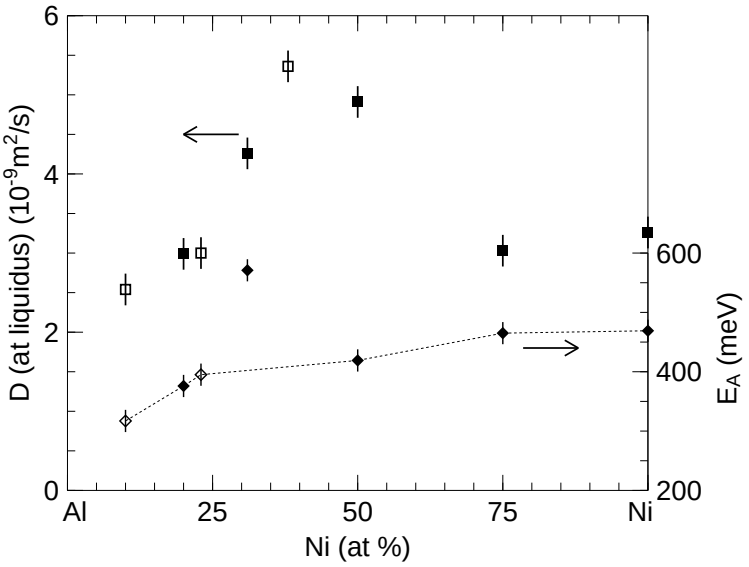

Figure 4.7: Ni self-diffusion coefficients at the respective liquidus temperature (squares), and derived activation energy (diamonds). The dotted line is a guide to the eye. Diffusion coefficients for Al-rich compounds are partly from container experiments [17](open symbols).

In the simplest approach, one would expect a roughly constant diffusion coefficient at liquidus, independent of composition, assuming similar packing of atoms at the respective liquidus [73]. Indeed, for both ends of the composition range (Al-rich and Ni-rich), the diffusion coefficients are comparably $3 \times 10^{-9}\,\mathrm{m^2 s^{-1}}$, despite the highly different melting temperatures (1726 K for Ni, 933 K for Al). For intermediate concentrations, the higher temperature of the intermetallic compund does seem to cause a moderate increase in diffusion. The activation energies are fairly equal, with somewhat lower values on the Al-rich side, except for the high value of $Al_{68.5}Ni_{31.5}$. The largest value of Ni self-diffusion is not reached for the Ni concentration with the highest liquidus temperature (1940 K for $Al_{50}Ni_{50}$), but already at around 40 at. % Ni. The phase diagram of Al-Ni is not reflected in the Ni self-diffusion coefficient.

Neither for the activation energy, nor for the Ni self-diffusion coefficient there is evidence for intermetallic phases, the principal behavior is that of a simple liquid like Ni.

Chapter 5

Interplay Structure and Dynamics

In the previous chapter, we discussed the temperature and concentration dependence of the Ni self-diffusion coefficient as one central quantity of dynamics, needed for the description and modeling of mass transport in liquid metals. We now want to look into possible interactions between structure and dynamics.

For topological ordering, this has been studied and predicted by De Gennes [20], cf. recent measurements and MD simulations for Ge [44, 69]. When we probe the dynamics with a momentum transfer q in the region of maxima of the static structure factor (the first maximum for Al-Ni alloys is usually just below $3\,\text{Å}^{-1}$ [18]), the scattering law $S(q,\omega)$ will show a reduced linewidth - the *De Gennes narrowing*. Pairs of particles sampled at this q value have distances close to certain "preferred" coordinations and move more slowly [53], or better their correlation decays more slowly. (Correlation life time and linewidth in $S(q,\omega)$ are inversely proportional.) Now the question arises if something similar as for topological ordering is also valid for chemical ordering. In part 5.2, a comparable effect for CSRO is presented.

In the work of [18] on Al-Ni alloys with CSRO, the partial structure factors of Al-Ni alloys were modeled to predict Ni self-diffusion coefficients for the whole compositional range and to explain the measured dynamics.

In this chapter, we first present measurements of the partial structure factors, static and dynamic, of one of the Al-rich alloys studied in [18], $Al_{80}Ni_{20}$, to be also compared to MD simulations.

5.1 Partial Structure Factors

In order to study the possible relations between structure and dynamics in detail, we need information of the correlations between all constituents of the melt. In the case of the Al-Ni alloy system, these are the Al-Al, Ni-Ni, and Al-Ni correlations. A standard way to parameterize these are the static partial structure factors $S_{\alpha\beta}(q)$.

5.1.1 Static Structure Factors

The static partial structure factors of a binary mixture are defined as [36]

$$S_{\alpha\beta}(q) = \frac{1}{N} \sum_{k_\alpha=1}^{N_\alpha} \sum_{l_\beta=1}^{N_\beta} \left\langle \exp\left[\mathrm{i}\mathbf{q} \cdot \left(\mathbf{r}_{k_\alpha} - \mathbf{r}_{l_\beta} \right) \right] \right\rangle \quad , \tag{5.1}$$

where the indices k_α and l_β correspond to particles of species α and β, respectively.

To determine the three unknown static partial structure factors, we need three sufficiently distinct measurements, cf. chapter 3.3. For the Al-Ni system, a possible approach is to perform QENS on alloys with three different isotopic enrichments of Ni. We chose the same sample compositions as in [61] (but now for QENS) and measured three $Al_{80}Ni_{20}$ samples, where the Ni was of natural isotopic composition, enriched ^{58}Ni, and enriched ^{60}Ni, respectively. The alloys were contained in Al_2O_3 crucibles, cf. chapter 3.2.2, resulting in a sample geometry of a hollow cylinder with an outer diameter of 22 mm, a wall thickness of 1.2 mm for the alloys with ^{58}Ni and Ni in natural isotopic composition, and 4 mm for the ^{60}Ni alloy. The filling height was 2 to 3 cm, crossing the neutron beam completely.

The measurements were performed at 1350 K at the time-of-flight spectrometer TOFTOF of the *Forschungsneutronenquelle Heinz Maier-Leibnitz*, with an incoming wavelength of 5.1 Å. Energy resolution was 90 μeV. The three alloys were prepared as described in chapter 2.3.

All measured spectra could be well fitted by a single (scaled) Lorentzian, even though ^{58}Ni and ^{60}Ni do not scatter incoherently, see Fig. 5.1. For all spectra, there is a slight asymmetry of the flanks. But as we are mainly interested in the half width at half maximum (HWHM) to derive the diffusivity $D(q)$ and the area of the scattering law to derive the structure factors, this is not corroborating our results, note the semilogarithmic presentation of Fig. 5.1. For a generalized description of scattering laws by a Lorentzian, cf. [7], e.g.

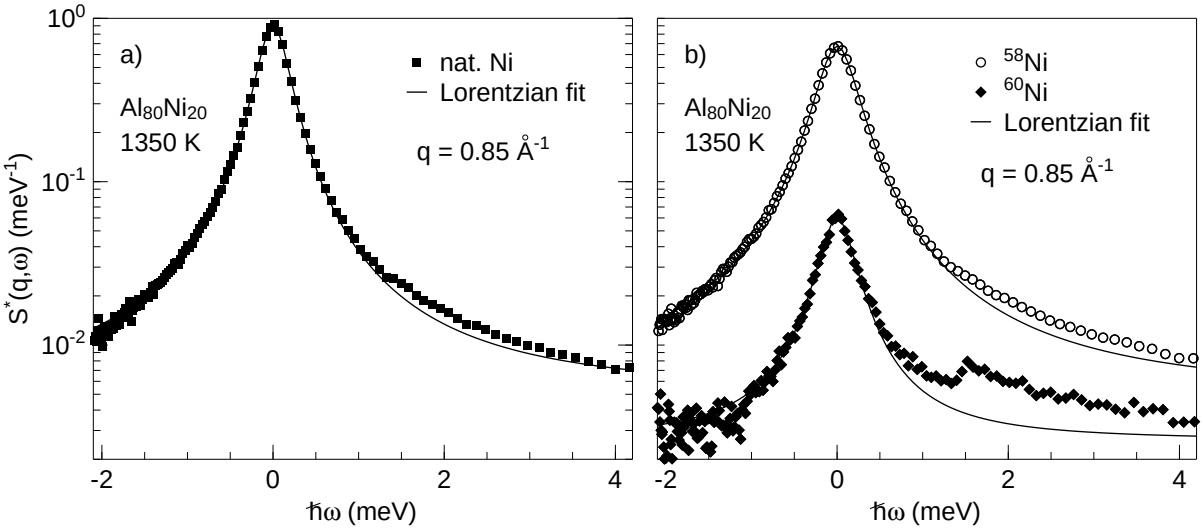

Figure 5.1: FRIDA-1 scattering law for $Al_{80}Ni_{20}$ with Ni in natural isotopic composition (filled squares), enriched ^{58}Ni (open circles), and enriched ^{60}Ni (filled diamonds). The lines are fits with a Lorentzian plus background. $q = 0.85\,\text{Å}^{-1}$.

To get the normalized spectra, we follow Eq. (3.15)

$$\left(\frac{\mathrm{d}\sigma}{\mathrm{d}\Omega}\right)^{norm} = S^*(q) \cdot \frac{n_V}{n_S} \cdot \frac{z_V}{z_S} \cdot \frac{\sigma_{inc}^V}{4\pi} \quad .$$

The vanadium wall thickness was 1 mm, for the $Al_{80}Ni_{20}$ with natural Ni and ^{58}Ni enrichment we had 1.2 mm, and for the sample with ^{60}Ni enrichment we used a 4 mm thick geometry. The number density of scatterers of $Al_{80}Ni_{20}$ is taken to be $6.3 \times 10^{22}\,\text{cm}^{-3}$, $n_V = 7.22 \times 10^{22}\,\text{cm}^{-3}$.

The resulting $\left(\frac{\mathrm{d}\sigma}{\mathrm{d}\Omega}\right)^{norm}$ for $Al_{80}Ni_{20}$ with three different Ni compositions are plotted in Fig. 5.2. For $Al_{80}Ni_{20}$ with ^{58}Ni and natural Ni, respectively, we see the prepeak of CSRO at about $1.7\,\text{Å}^{-1}$. But for the measurement with enriched ^{60}Ni, the scattering is weak and there is no prepeak. As in $Al_{80}{}^{60}Ni_{20}$, the Al scatters more strongly than the ^{60}Ni, we probe predominantly the Al-Al correlations. So it is to be expected that there also won't be a prepeak in the Al-Al partial structure factor, but in the Ni-Ni partial structure factor.

To get the total structure factors from Eq. (3.17), we need the respective

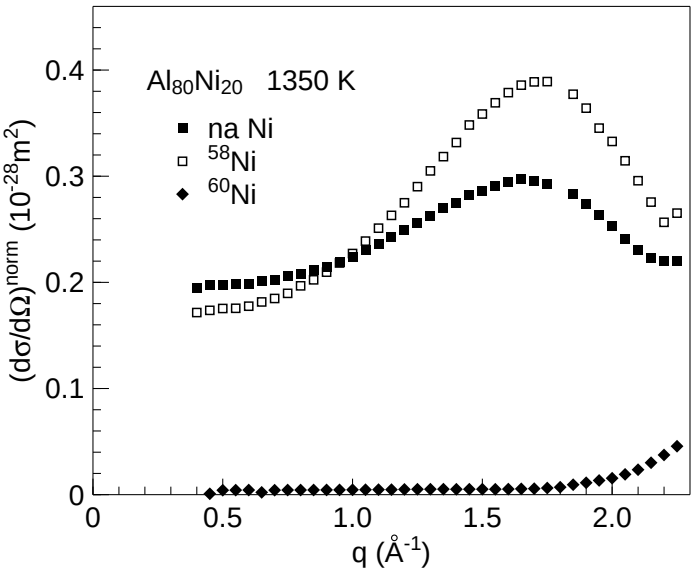

Figure 5.2: The normalized differential scattering cross sections for $Al_{80}Ni_{20}$, with natural Ni, ^{58}Ni, and ^{60}Ni enrichment, respectively.

total scattering cross sections. For the studied $Al_{80}Ni_{20}$ we have

$$\sigma_{tot}(Al_{80}{}^{na}Ni_{20}) = 4.90\,\text{barn} \quad (5.2)$$

$$\sigma_{tot}(Al_{80}{}^{58}Ni_{20}) = 6.42\,\text{barn} \quad (5.3)$$

$$\sigma_{tot}(Al_{80}{}^{60}Ni_{20}) = 1.40\,\text{barn} \quad . \quad (5.4)$$

σ_{tot} for $Al_{80}{}^{na}Ni_{20}$ contains also the contribution from incoherent scattering. The main problem in deriving the structure factors is the determination of the absolute values. Usually, an additional normalization constant is used to ensure that $S(q)$ has the correct large momentum transfer limit $S(q \to \infty) = 1$. As we study the structure factors quasi-elastically, only up to $q = 2.3\,\text{Å}^{-1}$, this is not possible in our case. Therefore subtracting a fixed quantity, as for example the total scattering cross sections of Eq. (5.2) to (5.4), from the measured total neutron structure factors is always connected with possible errors. The contributions of coherent scattering have less influence, as the structure factors, in a subsequent step, will be normalized by the coherent scattering cross sections. As in chapter 4, we will base the treatment of incoherent scattering on the notion that it dominates the scattering signal of $Al_{80}{}^{na}Ni_{20}$ for small q. When integrating the modeled incoherent scattering at low q (cf. section 5.1.3), this accounts for an additonal 1.3 barn in Eq. (5.2). So, the analysis will consider values for the incoherent scattering contribution to the $Al_{80}{}^{na}Ni_{20}$ signal[1] between minimally the literature value

[1]For $Al_{80}{}^{58}Ni_{20}$ and $Al_{80}{}^{60}Ni_{20}$, incoherent scattering is negligible.

of $\sigma_{inc}(^{na}\mathrm{Ni}) = 5.2\,\mathrm{barn}$, and maximally the modeled incoherent contribution. However, it will be shown that the different subtracted values of incoherent scattering contribution affect only the absolute values of the structure factors, but do not change the features we want to derive, i.e. the q position of peaks and the linewdith (for the dynamic structure factors). The latter quantities remain unchanged.

This can be seen in Fig. 5.3 b), which shows the total structure factor for $\mathrm{Al_{80}}^{na}\mathrm{Ni_{20}}$ at 1350 K for three different values of incoherent scattering Δ_{inc} subtracted. Filled circles represent the maximal $\Delta_{inc}^{model} = 0.19\,\mathrm{barn}$ from modeling the scattering law for small q to be purely incoherent. Open circles show the total structure factor for minimal subtraction of $\Delta_{inc}^{theo} = c_{Ni} \cdot \frac{\sigma_{inc}}{4\pi} = 0.083\,\mathrm{barn}$. The filled squares represent an intermediate subtraction of $\Delta_{inc}^{*} = 0.11\,\mathrm{barn}$, derived by considerations discussed in the following. The resulting total structure factors for $\mathrm{Al_{80}}^{58}\mathrm{Ni_{20}}$ and $\mathrm{Al_{80}}^{60}\mathrm{Ni_{20}}$ are shown in Fig. 5.3 a).

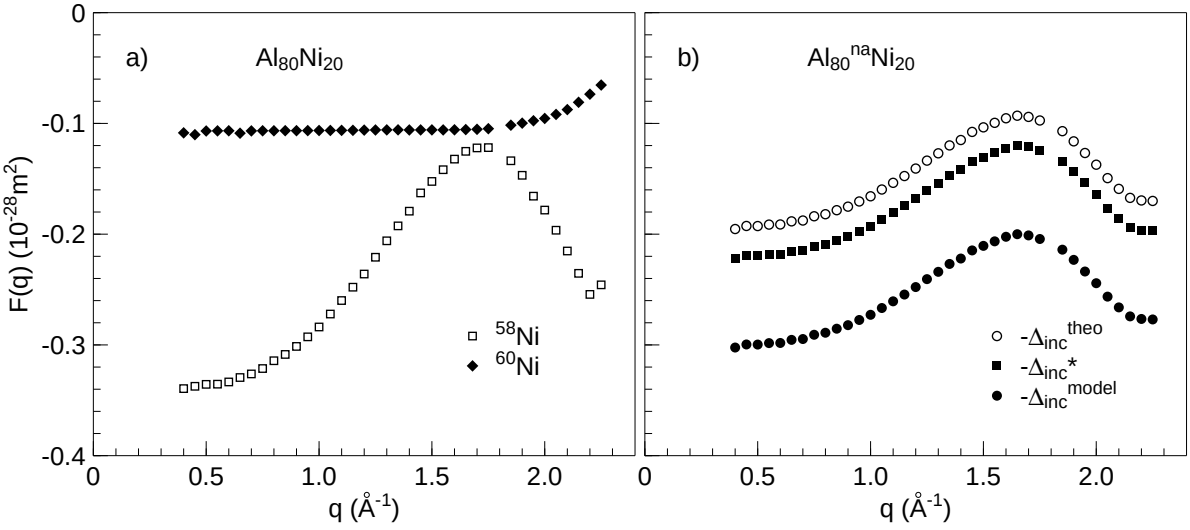

Figure 5.3: The total structure factors for $\mathrm{Al_{80}Ni_{20}}$, with ^{58}Ni and ^{60}Ni enrichment, respectively (a) and for $\mathrm{Al_{80}}^{na}\mathrm{Ni_{20}}$ (b) with consideration of three different values of the correction for incoherent scattering contributions.

Fig. 5.3 b) shows that a change of Δ_{inc} just shifts the absolute value of the total structure factor, its q-dependence is not affected. This will be the case for all the following partial structure factors.

To decide for the applicable Δ_{inc}, we studied the absolute values of the Bhatia-Thornton partial structure factors $S_{CC}(q)$ and $S_{NN}(q)$. These quantities must be larger than zero to have physical meaning. The Bhatia-Thornton

partial structure factors [6] are constructed from the Fourier transforms of the local number density and concentration in the alloy.

$$\begin{aligned} S(q) &= \frac{1}{\langle b^2 \rangle} \left(\frac{\mathrm{d}\sigma}{\mathrm{d}\Omega} \right)^{norm} \\ S(q) &= \frac{\langle b \rangle^2}{\langle b^2 \rangle} S_{NN}(q) + \frac{(\Delta b)^2}{\langle b^2 \rangle} S_{CC}(q) + \frac{2\Delta b \langle b \rangle}{\langle b^2 \rangle} S_{NC}(q) \quad , \end{aligned} \tag{5.5}$$

with $\Delta b = b_{Ni} - b_{Al}$. Here the normalization $1/\langle b^2 \rangle$ depends on the chosen value of incoherent scattering correction.

Fig. 5.4 a) and b) show the partial structure factors S_{CC} and S_{NN} for three values of Δ_{inc}. To derive the partial structure factors, three equations, one for each measured isotopic composition, of the type of Eq. (5.5) have to be solved (cf. Eq. (5.13) and (5.14)).

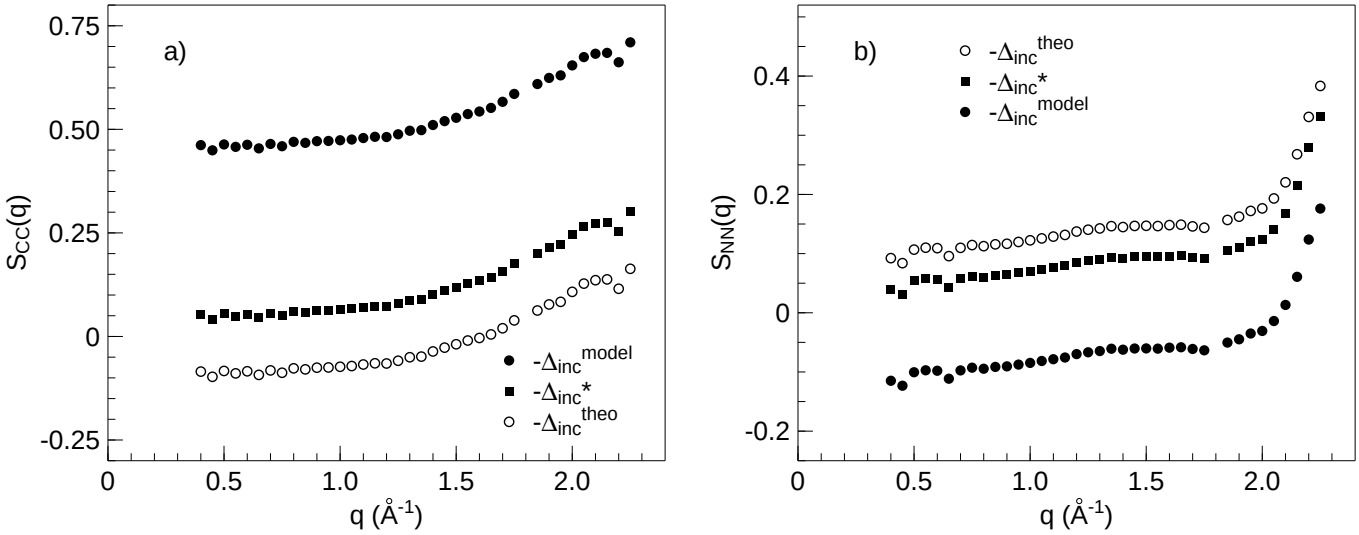

Figure 5.4: Bhatia-Thornton partial structure factors S_{CC} (a) and S_{NN} (b) for three values of Δ_{inc}.

Δ_{inc}^{model} corresponds to the maximal subtraction by assuming the scattering law of $Al_{80}{}^{na}Ni_{20}$ below $q \approx 0.7\,\text{Å}^{-1}$ to stem from incoherent scattering alone. Δ_{inc}^{theo} assumes absolute values for the total neutron structure factors from which the tabular value of incoherent scattering can be subtracted. These two values are the limitations within which we decided for a probable value. But important to note is, that all partial structure factors of number density correlations $S_{NN}(q)$ show no prepeak (Fig. 5.4 b), but the starting increase above $2\,\text{Å}^{-1}$ of the first structure factor maximum, independent on the

choosing of Δ_{inc}. A prepeak just shows up in the concentration-concentration structure factor $S_{CC}(q)$ of Fig. 5.4 a)[2], with its maximum shortly above $2\,\text{Å}^{-1}$, again independent of the absolute value. This is a clear indication for chemical ordering.

As can be seen in Fig. 5.4, the two limiting values Δ_{inc}^{model} and Δ_{inc}^{theo} lead to negative $S_{NN}(q)$ and $S_{CC}(q)$, respectively. In the following, we will therefore work with an intermediate Δ_{inc}^{*} of 0.11 barn, stressing again that this does neither influence the discussion of q-dependence or q positions of properties of (partial) structure factors, nor the HWHM (only the amplitude) of the dynamic partial structure factors of chapter 5.1.3.

The Bhatia-Thornton partial structure factors are in agreement with the findings of [61], cf. Fig. 2.4, though in that work, $S_{CC}(q)$ is defined without the prefactor $c_{Al}c_{Ni}$ of Eq. (3.23) and therefore oscillates around 1 and not $c_{Al}c_{Ni}$ as in our case.

As mentioned in chapter 3.4.5, we can give the static structure factor also in the Faber-Ziman formalism [25], which relates to the correlations by atom type.

$$\begin{aligned} I(q) &= 1 + \frac{F(q)}{\langle b \rangle^2} \\ I(q) &= \frac{c_{Al}^2 b_{Al}^2}{\langle b \rangle^2} S_{AlAl}(q) + \frac{c_{Ni}^2 b_{Ni}^2}{\langle b \rangle^2} S_{NiNi}(q) + \frac{2 c_{Al} c_{Ni} b_{Al} b_{Ni}}{\langle b \rangle^2} S_{AlNi}(q) \end{aligned} \quad (5.6)$$

The static structure factors $I(q)$ of our measurements are shown in Fig. 5.5. As in the normalized scattering cross section, we find prepeaks in the measurements with natural Ni and ^{58}Ni, but not in the one with ^{60}Ni enrichment. For $q \leq 1.7\,\text{Å}^{-1}$ (the peak maximum), the two curves $I(q)$ for $Al_{80}Ni_{20}$ with natural Ni and with ^{58}Ni enrichment run on top of each other, just like the result in $D(q)$ of Fig. 5.8.

Using Eq. (3.18), we now get a set of three equations, relating the three total structure factors $F_{na}(q)$, $F_{58}(q)$, and $F_{60}(q)$ from the respective measurements to the partial Faber-Ziman structure factors S_{AlAl}, S_{NiNi}, and S_{AlNi}:

$$\begin{pmatrix} F_{58}(q) \\ F_{60}(q) \\ F_{na}(q) \end{pmatrix} = \mathcal{B} \begin{pmatrix} S_{NiNi}(q) - 1 \\ S_{AlAl}(q) - 1 \\ S_{AlNi}(q) - 1 \end{pmatrix} \quad , \quad (5.7)$$

[2]To be more precise, one sees only an increase in $S_{CC}(q)$ with reduced slope towards $2\,\text{Å}^{-1}$, indicating a peak with its maximum at about $2.1\,\text{Å}^{-1}$, but this interpretation is sustained by the findings of Maret et al. [61], cf. Fig. 2.4 b).

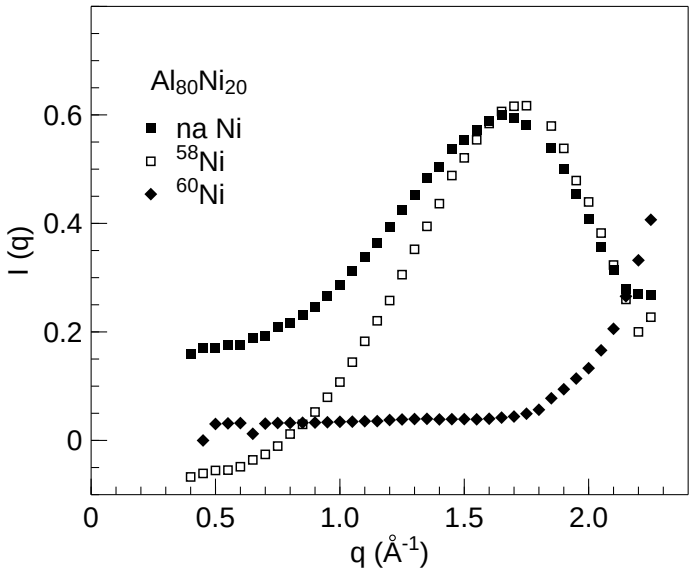

Figure 5.5: The static structure factors in Faber-Ziman notation $I(q)$ for $Al_{80}Ni_{20}$, with natural Ni, ^{58}Ni, and ^{60}Ni enrichment, respectively.

with

$$\mathcal{B} = \begin{pmatrix} c_{Ni}^2 b_{^{58}Ni}^2 & c_{Al}^2 b_{Al}^2 & 2c_{Ni}c_{Al}b_{^{58}Ni}b_{Al} \\ c_{Ni}^2 b_{^{60}Ni}^2 & c_{Al}^2 b_{Al}^2 & 2c_{Ni}c_{Al}b_{^{60}Ni}b_{Al} \\ c_{Ni}^2 b_{^{na}Ni}^2 & c_{Al}^2 b_{Al}^2 & 2c_{Ni}c_{Al}b_{^{na}Ni}b_{Al} \end{pmatrix} = \begin{pmatrix} 8.29 & 7.61 & 15.89 \\ 0.31 & 7.61 & 3.09 \\ 4.24 & 7.61 & 11.37 \end{pmatrix} \cdot 10^{-30}\,\mathrm{m}^2, \tag{5.8}$$

containing the coherent scattering lengths of the constituents. Matrix inversion then leads to the static partial structure factors of Fig. 5.6.

The Al-Al partial structure factor has a constant small negative value and increases slightly, starting shortly below $2\,\text{Å}^{-1}$. The Ni-Ni partial structure factor starts at a more negative value and increases at much smaller q values than S_{AlAl}. This increase is expected to be the flank of a prepeak at around $2\,\text{Å}^{-1}$, but the decay in Ni-Ni correlation afterwards is not clear enough to be sure. However a comparison with the data of the large q range of Maret et al. [61] supports this interpretation, see Fig. 2.4. So, the position of the prepeak changes when going from partial to static structure factors.

The combination of the three partial structure factors as in Eq. (3.18) therefore can lead to a prepeak in the total structure factor. In our case this happens for $Al_{80}Ni_{20}$ with ^{58}Ni and natural Ni, but not for $Al_{80}Ni_{20}$ with ^{60}Ni. However, the chemical ordering is the same for every isotopic composition. In the case of $Al_{80}{}^{60}Ni_{20}$, the scattering of the ^{60}Ni atoms is weaker than that of the Al atoms. That is why in the case of a sample enriched with ^{60}Ni, we see dominantly the Al dynamics, whereas in samples with natural Ni

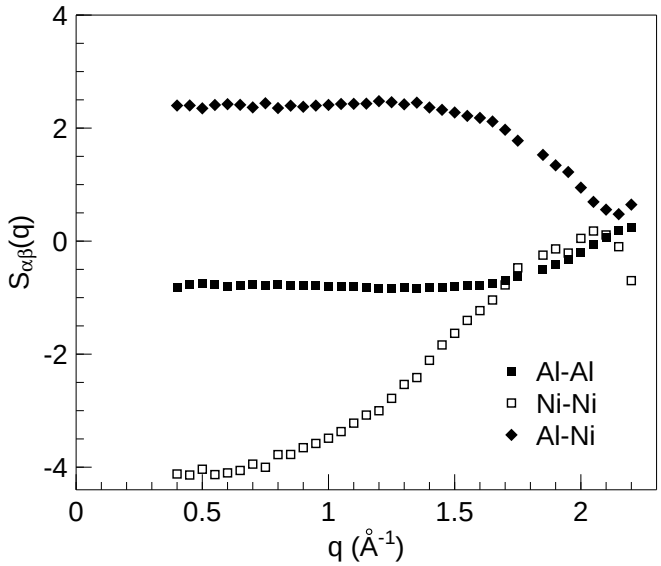

Figure 5.6: Static Faber-Ziman partial structure factors for $Al_{80}Ni_{20}$ at 1350 K.

isotopic composition or enriched with ^{58}Ni, the Ni dynamics is the dominant contribution. But the position of the prepeak changes when combining the partial structure factors to the static one. So, the considerations of Das et al. [18] on the oreoeak position in the static structure factor is not conclusive, only a study of partial structure factors can give clear insights.

The Bhatia-Thornton static structure factor $S(q)$ is shown for our experiments in Fig. 5.7. Similar to the Faber-Ziman structure factors of Fig. 5.5, prepeaks show up in the measurements with ^{58}Ni and natural Ni, but not with ^{60}Ni enrichment. Also, for $q \leq 1.7\,\text{Å}^{-1}$, the two curves $I(q)$ for $Al_{80}Ni_{20}$ with natural Ni and with ^{58}Ni enrichment again run on top of each other. In comparison to the Faber-Ziman structure factors of Fig. 5.5, the normalization of the prepeaks is different, note the different absolute values (0.75 for the prepeak in Bhatia-Thornton notation, 0.6 for the Faber-Ziman normalization).

5.1.2 Diffusivity

Analogously to previous analyses, we can study the linewidths of the fitted Lorentzians to each scattering function $S(q,\omega)$ for each q value to derive the diffusivity $D(q) = \Gamma_{1/2}(q)/(\hbar q^2)$ from Eq. (3.11). This is shown for the $Al_{80}Ni_{20}$ alloys in Fig. 5.8. Given are the results for the measured samples with three different Ni isotopic compositions. The striking feature in the

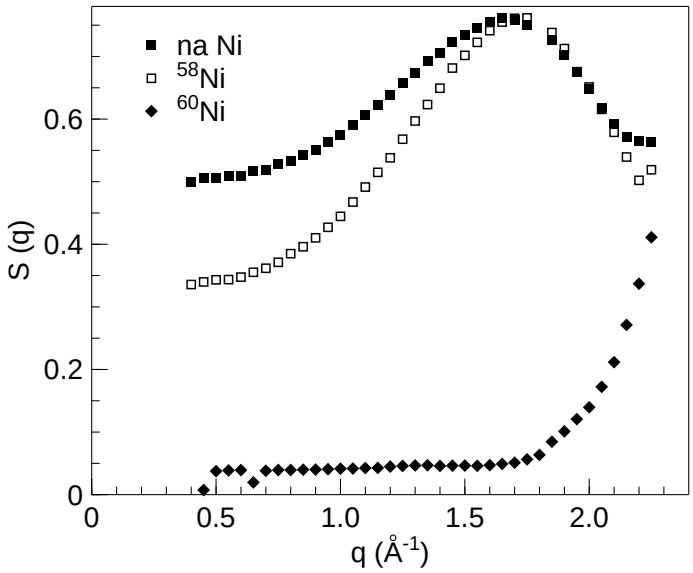

Figure 5.7: The static Bhatia-Thornton structure factors for $Al_{80}Ni_{20}$, with natural Ni, ^{58}Ni, and ^{60}Ni enrichment, respectively.

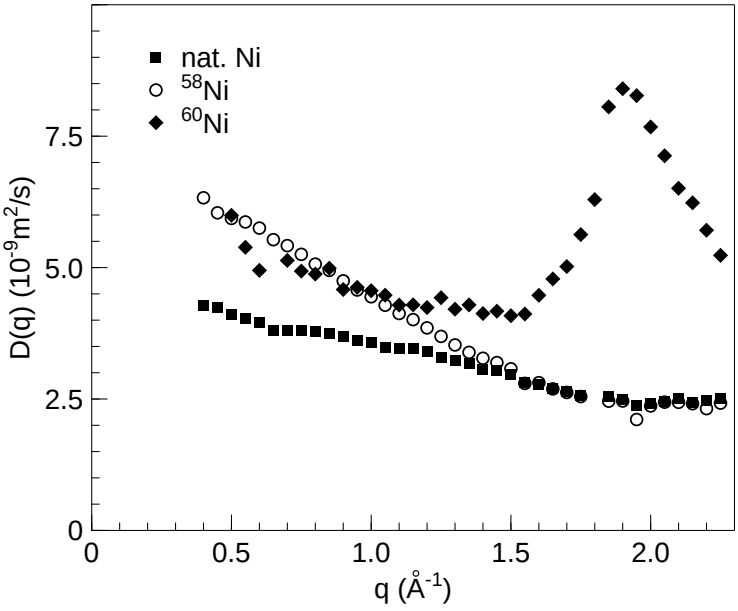

Figure 5.8: q-dependent diffusivity as function of momentum transfer for the three $Al_{80}Ni_{20}$ samples with different Ni composition: Ni with natural composition (filled squares), enriched ^{58}Ni (circles), and enriched ^{60}Ni (diamonds).

diffusivity of Fig. 5.8 is the strong increase observed for $Al_{80}{}^{60}Ni_{20}$ in the region around $2\,\text{Å}^{-1}$. This can again be explained by the weak scattering of

^{60}Ni, i.e. with this isotopic enrichment, we strongly probe the Al dynamics. See the comparison with simulation later in this chapter.

When looking at $Al_{80}{}^{58}Ni_{20}$ and $Al_{80}{}^{na}Ni_{20}$, we find similar values for $D(q)$ in the region around $2\,\text{Å}^{-1}$. In these two alloys, Ni is the dominant scatterer. For q values lower than about $1.5\,\text{Å}^{-1}$, one can also clearly see a higher diffusivity for the coherent scatterers (^{58}Ni and ^{60}Ni) compared to the incoherent scattering alloy with natural Ni isotopic composition.

5.1.3 Dynamic Partial Structure Factors

An even more detailed analysis of the dynamics of an alloy system can be achieved when studying the dynamic partial structure factors

$$S_{\alpha\beta}(q,t) = \frac{1}{N}\left\langle \delta\rho_\alpha(\mathbf{q},t)\delta\rho^*_\beta(\mathbf{q},0)\right\rangle \quad , \tag{5.9}$$

with thermal averaging and $\delta\rho_\alpha(\mathbf{q},t)$ the density fluctuation of species α:

$$\delta\rho_\alpha(\mathbf{q},t) = \sum_{j=1}^{N_\alpha} \exp\left[\mathrm{i}\mathbf{q}\cdot\mathbf{r}_j(t)\right] \quad . \tag{5.10}$$

The dynamic partial structure factors can be derived from the measured $S^*(q,\omega)$ with a similar matrix inversion treatment as above. Simply speaking, we just keep the dependence on q and ω; we just have to make sure that we only multiply by factors, then the moment of integration from $S(q,\omega)$ to $S(q)$ does not matter. For this we have to subtract the incoherent part of $S^*(q,\omega)$ for the measurement of natural $Al_{80}Ni_{20}$. When we then approximate the scaling $1/\langle b\rangle^2$ of Eq. (3.19) by $1/\langle b^2\rangle$, Eq. (3.13) to (3.19) simplify to

$$S(q,\omega) = \frac{4\pi}{\sigma_{coh}}\cdot\frac{n_V}{n_S}\cdot\frac{z_V}{z_S}\cdot\frac{\sigma^V_{inc}}{4\pi}\cdot S^*(q,\omega) \quad . \tag{5.11}$$

We model the incoherent part of the scattering from $Al_{80}Ni_{20}$ using Eq. (3.10), with $D = 3.93\times10^{-9}\text{m}^2/\text{s} = 0.393\,\text{Å}^2/\text{ps}$. The scaling factor A is taken to match the scattering laws for small $q \le 0.8\,\text{Å}^{-1}$. In Fig. 5.9 are plotted the total scattering function of $Al_{80}{}^{na}Ni_{20}$ for $q = 1.65\,\text{Å}^{-1}$, and the result of subtracting the modeled incoherent part (the line in Fig. 5.9 a). The result has again Lorentzian shape.

We can evaluate the resulting coherent part of the scattering law to get the coherent part of the normalized scattering cross-section, see Fig. 5.10. Below $q \approx 0.8\,\text{Å}^{-1}$, it is difficult to calculate a value for the coherent scattering. Due to the small coherent contributions, the error from the subtraction

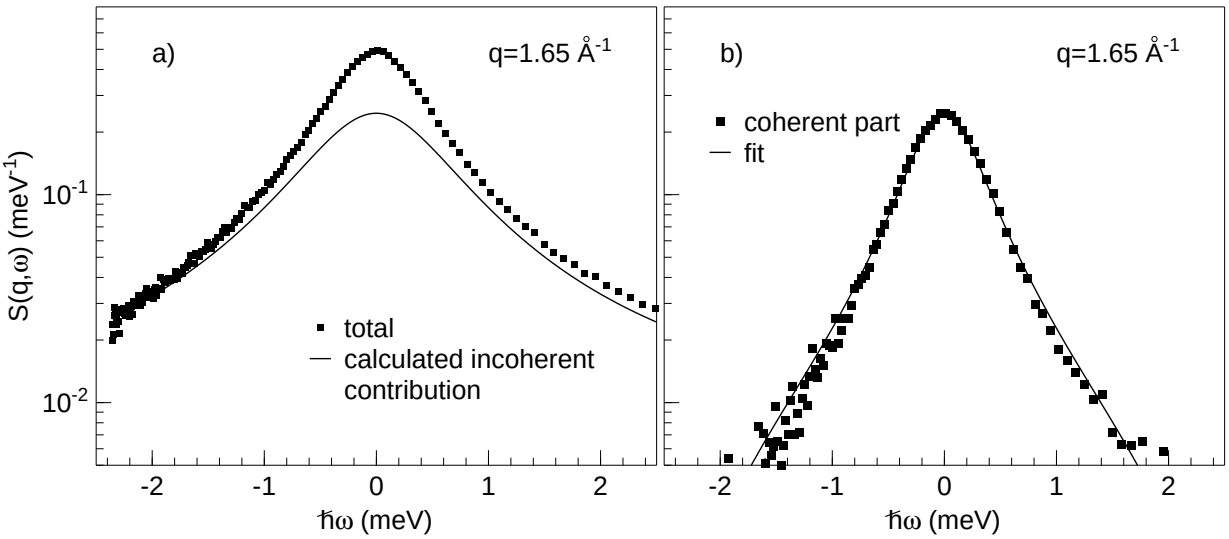

Figure 5.9: Total scattering law for $Al_{80}Ni_{20}$ at 1350 K and $q = 1.65\,\text{Å}^{-1}$ with modeled incoherent contribution (a), and resulting coherent scattering law (b).

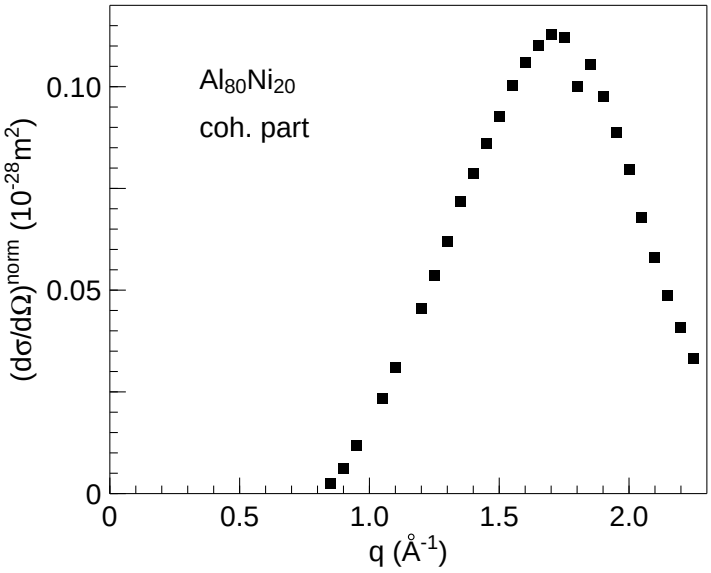

Figure 5.10: Normalized coherent scattering cross-section of $Al_{80}{}^{na}Ni_{20}$ at 1350 K.

of incoherent scattering contributions is rather large.

Keeping the energy dependence we can use the matrix of Eq. (5.8) to

derive the dynamic partial structure factors [3].

$$\begin{pmatrix} S_{NiNi}(q,\omega) \\ S_{AlAl}(q,\omega) \\ S_{AlNi}(q,\omega) \end{pmatrix} = \mathcal{B}_{norm}^{-1} \begin{pmatrix} S_{58}(q,\omega) \\ S_{60}(q,\omega) \\ S_{na}(q,\omega) \end{pmatrix} \quad . \tag{5.12}$$

The result is shown in Fig. 5.11 for two different q values. The first obvious

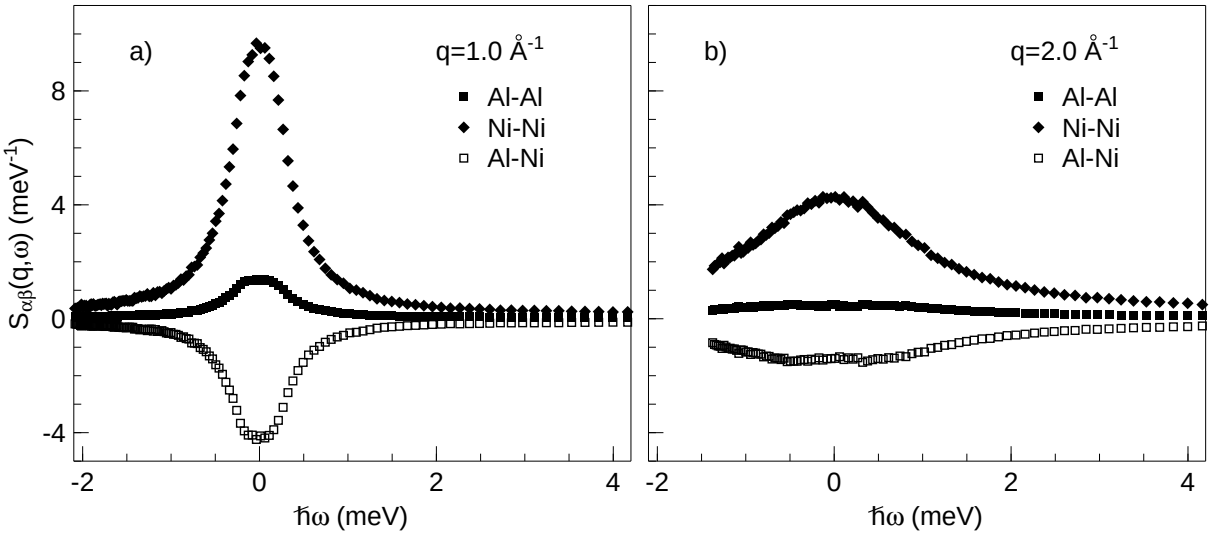

Figure 5.11: Dynamic partial structure factors $S_{\alpha\beta}(q,\omega)$ for $Al_{80}Ni_{20}$ at 1350 K and $q = 1.0\,\text{Å}^{-1}$ (a) and $q = 2.0\,\text{Å}^{-1}$ (b).

result is that Ni has a higher dynamic Ni-Ni partial structure factor than Al-Al. The cross term $S_{AlNi}(q,\omega)$ is always negative. Part a) shows the dynamic partial structure factors for $q = 1.0\,\text{Å}^{-1}$ in energy space. In part b), we see that for $q = 2.0\,\text{Å}^{-1}$, the scattering laws $S_{\alpha\beta}(q,\omega)$ get broader and have reduced amplitude. High q values also reduce the available energy transfer range at negative ω (energy loss).

Fig. 5.12 shows the Fourier transforms of the $S_{\alpha\beta}(q,\omega)$, the partial structure factors in time space $S_{\alpha\beta}(q,t)$, for three values of momentum transfer q, again in the Faber-Ziman notation. The straight lines are fits with an exponential decay, to derive the lifetime $\tau_{\alpha\beta}$. The dotted lines are similar fits, but with a fixed amplitude $S(q,0)$ from $S(q = 0.8\,\text{Å}^{-1}, 0)$, The two derived sets of lifetimes do not differ much.

Das et al. [19] performed extensive MD simulations for $Al_{80}Ni_{20}$ in a temperature range from 665 K to 4490 K. At our temperature above liquidus

[3]But this time each line of the matrix has to be normalized by the respective $\frac{\sigma_{coh}^{tot}}{4\pi} = c_{Al}b_{Al}^2 + c_{Ni}b_{Ni}^2$.

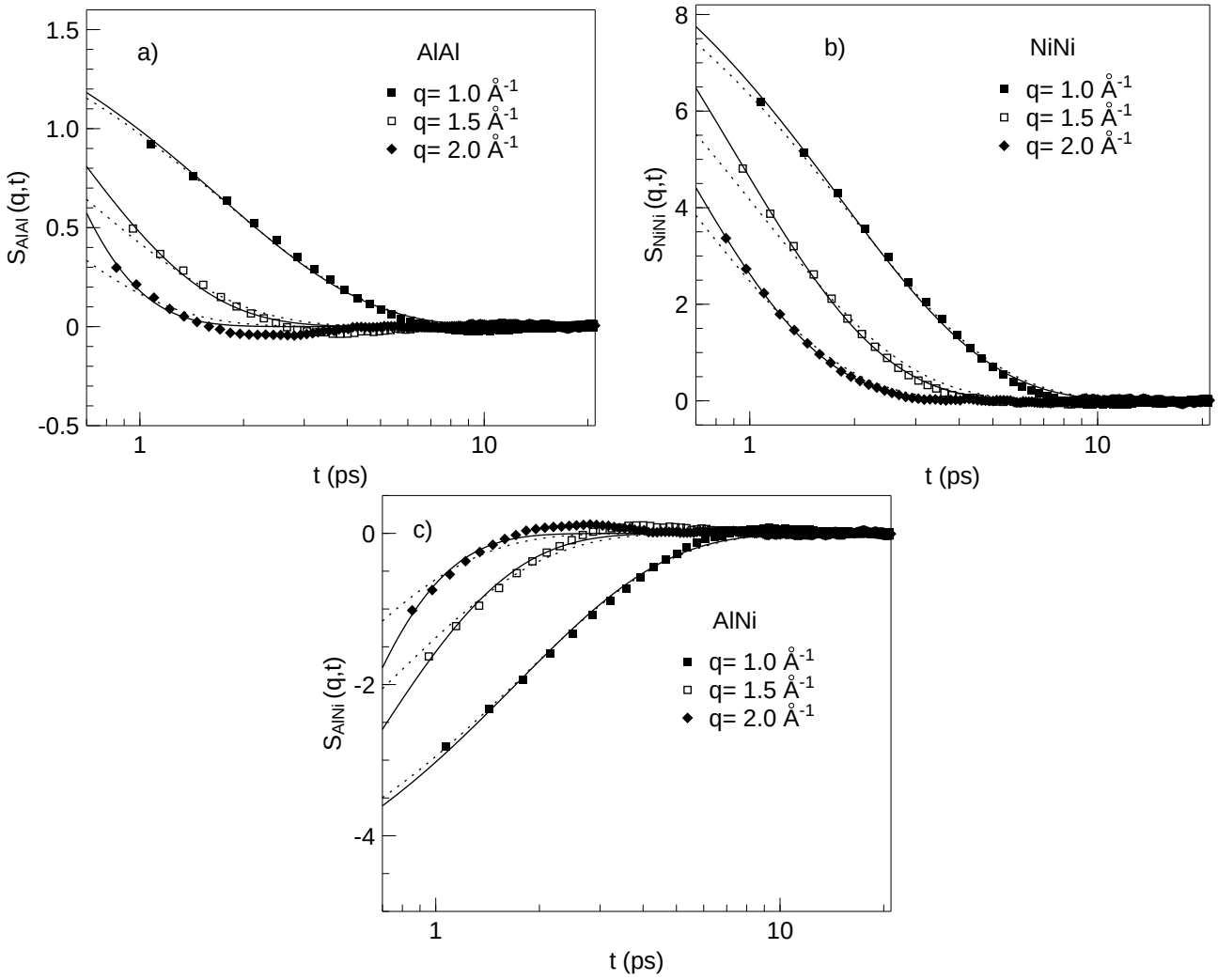

Figure 5.12: Dynamic partial structure factors $S_{AlAl}(q,t)$ (a), $S_{NiNi}(q,t)$ (b), and $S_{AlNi}(q,t)$ (c) for $Al_{80}Ni_{20}$ at 1350 K and three different q values. The straight lines are fits with an exponential decay without constraints, dotted lines are with fixed amplitude.

(1350 K), we are far away from the critical temperature of mode coupling theory $T_c \approx 700$ K [19]. That is why we do not see a two-step decay in $S(q,t)$, but a simple exponential decay to zero correlation within picoseconds. From this exponential decay, we derive the relaxation times τ, when the intermediate scattering function has decayed to 1/10 of the value at time 0 (defined accordingly to [19]). The derived relaxation times τ are stable with respect to errors in subtraction of the incoherent scattering for natural Ni. For example, if we subtract only 80 % of the modeled incoherent scatter-

ing contribution, the $S_{\alpha\beta}(q,\omega)$ will change in amplitude. But the coherent relaxation times show the same qualitative behavior, the effects described below even tend to become more pronounced. The absolute value of $1/(\tau q^2)$ in this case increases by at most 20 %.

The result for the coherent relaxation times $\tau_{\alpha\beta}(q)$ is plotted in Fig. 5.13. We see that in the region of the prepeak from around 1.5 Å^{-1} to above 2 Å^{-1},

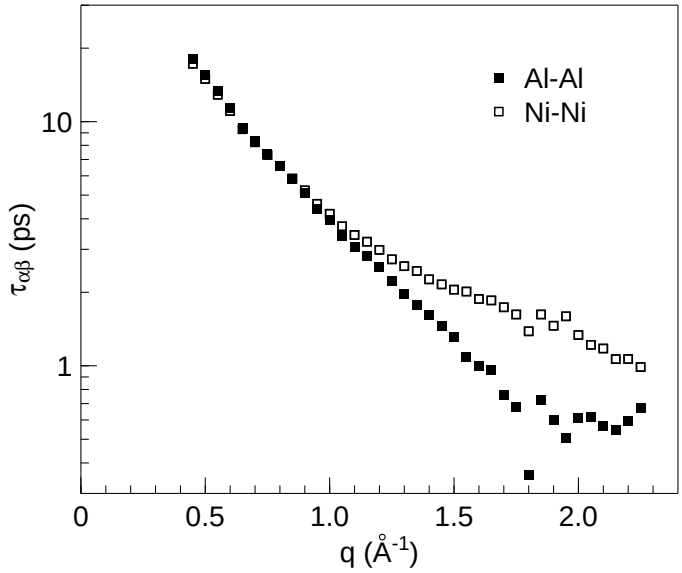

Figure 5.13: q-dependence of the coherent relaxation times $\tau_{\alpha\beta}(q)$ at 1350 K.

the Ni-Ni correlations show higher relaxation time, whereas the Al-Al correlation life time decreases continually. The error from the uncertainty of the amplitude $S(q, t = 0)$ is within the fluctuations of τ. In [19], for low temperatures up to 750 K, τ_{AlAl}, as well as τ_{NiNi}, show this increase in the region of the prepeak. For a similar simulation temperature (1360 K) as of our measurement (1350 K), the simulation yields no increase in coherent relaxation times [42], neither for Al-Al nor for Ni-Ni, see Fig. 5.14. The absolute values of the correlation times of the experiment and the simulation are comparable, and also the Ni-Ni correlation has longer lifetime in both cases. The experimental data shows equal correlation times for Al-Al and Ni-Ni for $q \leq 1.1$ Å^{-1}. This has to be qualified, as for the region of small q, the derivation of the purely coherent scattering part of the measurement with natural Ni isotopic composition has rather high error, as the coherent scattering in this q range is weak.[4] Unlike in [19], there is no indication that

[4]This was exactly the reason for modeling the scattering law as a simple Lorentzian from incoherent Ni scattering.

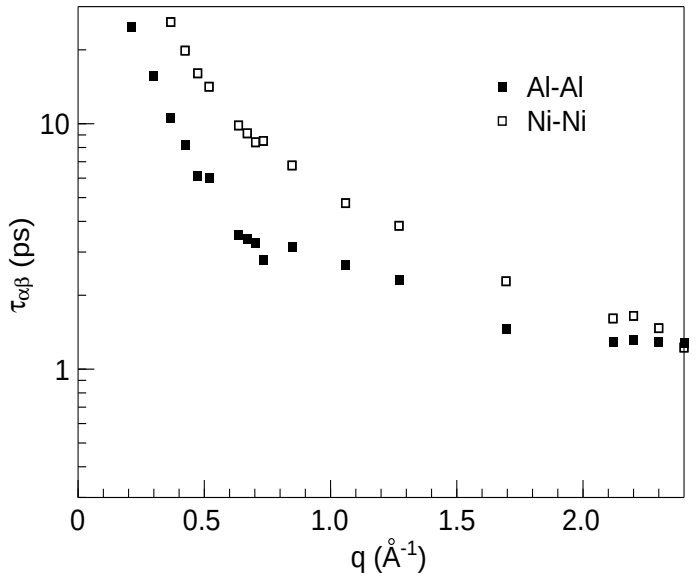

Figure 5.14: Simulated q-dependence of coherent relaxation times $\tau_{aa}(q)$ at 1360 K.

$\tau_{\alpha\beta}(q)$ is not in phase with the corresponding static partial structure factor $S_{\alpha\beta}(q)$.

From these relaxation times, we can calculate the q-dependent diffusivity $D(q) = 1/(\tau q^2)$. The result shows Fig. 5.15.

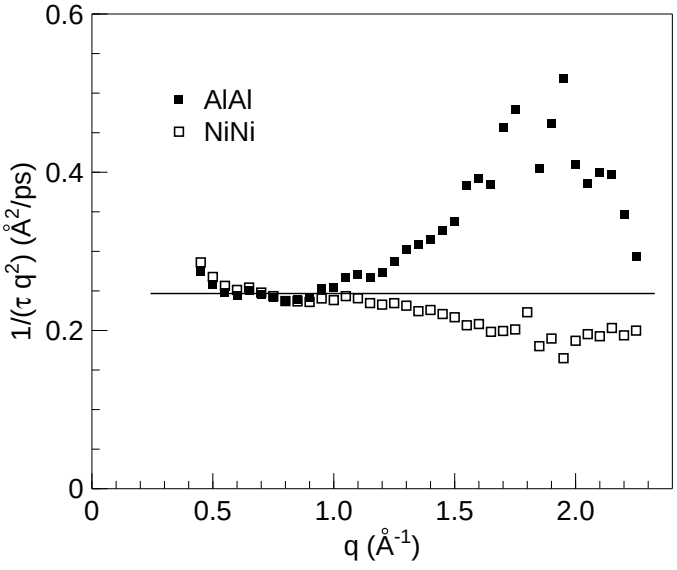

Figure 5.15: $1/(\tau q^2)$ for Al-Al and Ni-Ni correlations at 1350 K.

The relative increase of the Ni-Ni relaxation time leads to a decrease in the respective diffusivity, whereas for Al-Al correlation we find a peak at

the position of the prepeak in the total structure factor. In comparing with Fig. 5.8, we see that with the ^{60}Ni sample, we indeed probe predominantly the Al dynamics.

The straight line of Fig. 5.15 symbolizes what would be expected from a purely incoherent scatterer, where the relaxation time is proportional to q^{-2}.

Simulation now also provides data for the incoherent relaxation time for Ni, shown in Fig. 5.16. Except for the differing absolute value of the diffu-

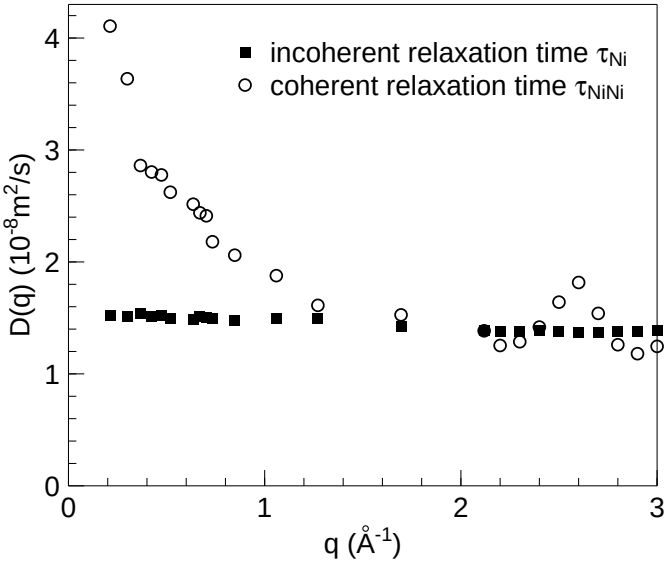

Figure 5.16: q-dependent diffusivity from simulated incoherent and coherent Ni relaxation times at 1360 K.

sivity, the relative behavior of the diffusivities for incoherent and coherent Ni is exactly the same as for $Al_{80}Ni_{20}$ with natural Ni and ^{58}Ni enrichment, respectively, see Fig. 5.8. The data for $Al_{80}Ni_{20}$ with ^{60}Ni enrichment in Fig. 5.8 can be explained by referring to Fig. 5.15.

Also for the dynamic partial structure factors, it is possible to give them in the Bhatia-Thornton formalism, to study and differentiate contributions from topological and chemical ordering. Furthermore, we are not forced to approximate the partial structure factors in this notation. We have to solve the equation

$$\begin{pmatrix} \frac{1}{\langle b^2\rangle_{58}}\left(\frac{\mathrm{d}\sigma}{\mathrm{d}\Omega}\right)^{norm}_{58}(q,\omega) \\ \frac{1}{\langle b^2\rangle_{60}}\left(\frac{\mathrm{d}\sigma}{\mathrm{d}\Omega}\right)^{norm}_{60}(q,\omega) \\ \frac{1}{\langle b^2\rangle_{na}}\left(\frac{\mathrm{d}\sigma}{\mathrm{d}\Omega}\right)^{norm}_{na}(q,\omega) \end{pmatrix} = \mathcal{M} \begin{pmatrix} S_{NN}(q,\omega) \\ S_{CC}(q,\omega) \\ S_{NC}(q,\omega) \end{pmatrix} \quad , \tag{5.13}$$

with

$$\mathcal{M} = \begin{pmatrix} \frac{\langle b\rangle_{58}^2}{\langle b^2\rangle_{58}} & \frac{(\Delta b)_{58}^2}{\langle b^2\rangle_{58}} & \frac{2\Delta b_{58}\langle b\rangle_{58}}{\langle b^2\rangle_{58}} \\ \frac{\langle b\rangle_{60}^2}{\langle b^2\rangle_{60}} & \frac{(\Delta b)_{60}^2}{\langle b^2\rangle_{60}} & \frac{2\Delta b_{60}\langle b\rangle_{60}}{\langle b^2\rangle_{60}} \\ \frac{\langle b\rangle_{na}^2}{\langle b^2\rangle_{na}} & \frac{(\Delta b)_{na}^2}{\langle b^2\rangle_{na}} & \frac{2\Delta b_{na}\langle b\rangle_{na}}{\langle b^2\rangle_{na}} \end{pmatrix} = \begin{pmatrix} 0.6237 & 2.3520 & 2.4223 \\ 0.9946 & 0.03800 & -0.366 \\ 0.7556 & 1.5272 & 2.1485 \end{pmatrix} \quad . \tag{5.14}$$

The partial structure factor of the number density correlation is too low in our studied q range to be able to derive further information out of it. The concentration-concentration partial structure factor $S_{CC}(q,\omega)$ is shown in Fig. 5.17 a). Fig. 5.17 a) gives the Fourier transform $S_{CC}(q,t)$. The

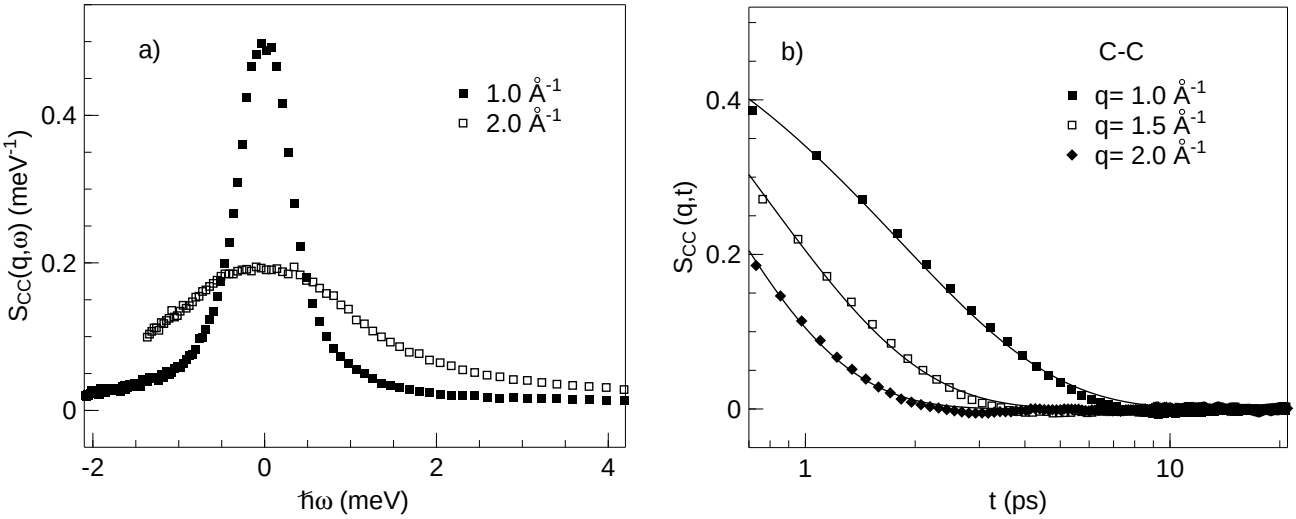

Figure 5.17: Bhatia-Thornton concentration-concentration partial structure factor $S_{CC}(q,\omega)$ (a) and its Fourier transform $S_{CC}(q,t)$ (b) for several q values.

qualitative behavior of S_{CC} is similar to that of the $S_{\alpha\beta}$.

Again we derive the relaxation time τ_{CC} from the exponential decay of $S_{CC}(q,t)$. It is shown in Fig. 5.18 a). Also shown are the Faber-Ziman relaxation times τ_{NiNi} and τ_{NiNi}, for reason of clarity depicted as lines. We see that the relaxation times of the concentration correlation, a measure of how fast Al-Ni coordinations decay, lie in between the coherent relaxation times of Al-Al and Ni-Ni correlations.

Fig. 5.18 b) shows $1/(\tau_{CC}q^2)(q)$, together with $1/(\tau_{NiNi}q^2)$ and $1/(\tau_{AlAl}q^2)$, according to picture 5.15. We find that the concentration correlations have no increased relaxation times in the region of the prepeak of CSRO. For the partial structure factor S_{CC}, the increased relaxation time of the Ni-Ni correlations and the decreased relaxation time of the Al-Al correlations seem

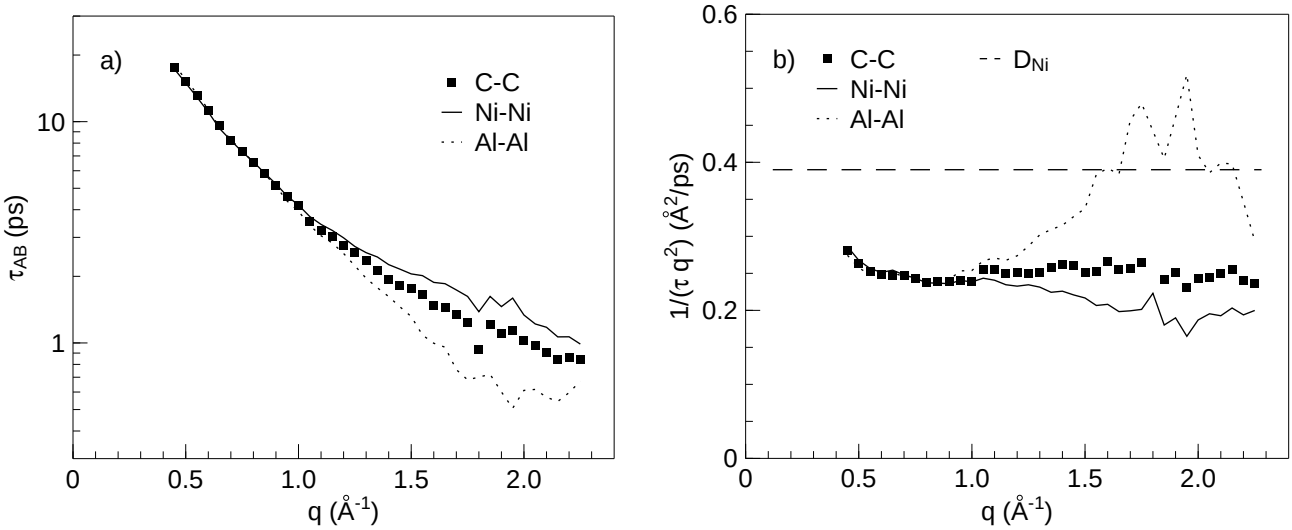

Figure 5.18: q-dependence of coherent relaxation time $\tau_{CC}(q)$ (a) and $1/(\tau_{CC}q^2)(q)$ (b) at 1350 K. The insetted line of (b) gives the value of the Ni slef-diffusion coefficient.

to add up to a constant, q independent value of $0.25\,\text{Å}^2/\text{ps} = 2.5 \times 10^{-9}\,\text{m}^2/\text{s}$. This value is somewhat lower than the derived value for the Ni self-diffusion coefficient of $3.9 \times 10^{-9}\,\text{m}^2/\text{s}$, it rather corresponds to the common value $D(q)$ of $Al_{80}Ni_{20}$ with natural Ni isotopic composition, and ^{58}Ni enrichment, respectively, for $q \leq ,1.5\,\text{Å}^{-1}$, cf. Fig. 5.8. However, this absolute value of the derived diffusion coefficients is depending somewhat (about 20 %) on the chosen normalization/ treatment of incoherent scattering Δ_{inc}.

We can relate S_{CC} to the interdiffusion D_{AlNi}. The interdiffusion is given by the Darken relation [43]

$$D_{AlNi} = \Phi \cdot S \cdot (c_{Al} D_{Ni} + c_{Ni} D_{Al}) \quad , \tag{5.15}$$

with S the contribution of cross correlations approx. equal to unity [43], $D_{Ni} \approx D_{Al}$ [43], and Φ the thermodynamic factor, for which applies

$$\Phi = \frac{c_{Al} c_{Ni}}{S_{CC}(q=0)} \quad . \tag{5.16}$$

Taking the value of S_{CC} for low q from Fig. 5.4 to be approximately 0.05, we would get for the interdiffusion

$$D_{AlNi} \approx 3 \cdot D_{Ni} \quad . \tag{5.17}$$

This ratio is in agreement with MD simulation [43]. However, $1/(\tau_{CC}q^2)$ in Fig. 5.18 b), which can be taken as the q-dependent interdiffusion $D_{AlNi}(q)$ [84],

indicates firstly that the interdiffusion D_{AlNi}, is q-independent, and secondly that in the hydrodynamic limit $q \to 0$, the self-diffusion coefficients of Ni and Al have the same value and are equal to the interdiffusion. This was not observed in the MD simulation [19]. In the region of increased Al self-diffusion, shortly below $2\,\text{Å}^{-1}$, $\bar{D} = c_{Al}D_{Ni} + c_{Ni}D_{Al}$ increases because of the increase of $D_{Al}(q)$, But this increase is exactly cancelled by the increase in $S_{CC}(q)$, when we use the extension of Eq. (5.15) to finite q, following Soltwisch et al. [84],

$$D_{AlNi} = \frac{c_{Al}c_{Ni}}{S_{CC}(q)}\bar{D} \quad . \tag{5.18}$$

A deviation of $S_{CC}(q)$ from the default value $c_{Al}c_{Ni}$ can be pictured as the amount of molecules/ agglomerates of Al_4Ni in the melt [84]. The Lorentzian form of $S_{CC}(q,\omega)$ implies an exponential time decay of these agglomerates. The individual atoms are wandering at a rate determined by D_{Al} and D_{Ni}, Al correlations decay faster than Ni correlations when probed with $q \geq 1\,\text{Å}^{-1}$. But the structure Al_4Ni lives longer by a factor $S_{CC}(q)/c_{Al}c_{Ni}$. The individual motion of Al and Ni and the more stable structure lead to a q-independent interdiffusion.

We already discussed the mass transport mechanism of Al-Ni alloys in chapter 4.2. In $Al_{80}Ni_{20}$, Al is the dominant species and one could assume that the Ni atoms would just randomly take the available spaces left free by Al. And the diffusion really is faster (compared to the Ni rich Al-Ni alloys), as packing fraction is lower due to Al. But as the prepeak in the structure factors (Fig. 5.3 to 5.7)[5] and the increased lifetime of the coherent Ni-Ni correlations (Fig. 5.13 and 5.15) show, the Ni diffusion is not a random hard sphere process, but chemical ordering influences the dynamics. And when probing Ni atoms in the q range of the prepeak of CSRO, their correlation does show an increased relaxation time. So there are certain preferred coordinations between Ni, which is exactly what CSRO means, but the effect on diffusion is quite similar to that of topological ordering, namely a reduced diffusion of Ni corresponding to regions of q with increased ordering. In contrast to this, the correlations of the main species Al seem to decay faster in the q range of CSRO.

For the example of $Al_{80}Ni_{20}$, we showed how one can derive details of the dynamics by analyzing the structure, more specific the dynamic partial structure factors. The findings were compared and sustained by MD simulations. For this set of experiments, the alloy was contained in an Al_2O_3

[5]For static structure factors covering the range of high momentum transfer, see [61], or in a binary Ni-Zr alloy [93].

container above liquidus. But also for the levitation experiments, we studied the interplay between the dynamics (in form of the q-dependent diffusivity $D(q)$) and CSRO.

5.2 Effect of Ordering on Diffusivity

We also performed QENS measurements on levitated alloys with an incoming neutron wavelength of 3.8 Å. We then get access to a range of momentum transfer from $q = 0.7\,\text{Å}^{-1}$ to $q = 3.1\,\text{Å}^{-1}$ at zero energy transfer. This encompasses also the first structure factor maximum of most Al-Ni alloys. As influences of coherent scattering then increase and the energy resolution is only 165 μeV, this wavelength is not optimally suited to derive the Ni self-diffusion coefficient, but nevertheless insights can be gained from the q-dependent diffusivity at these higher q values.

Let us take $Al_{50}Ni_{50}$ as example, its q-dependence of the scattering law is shown in Fig. 5.19 at a 100 degree of undercooling. The solid lines of

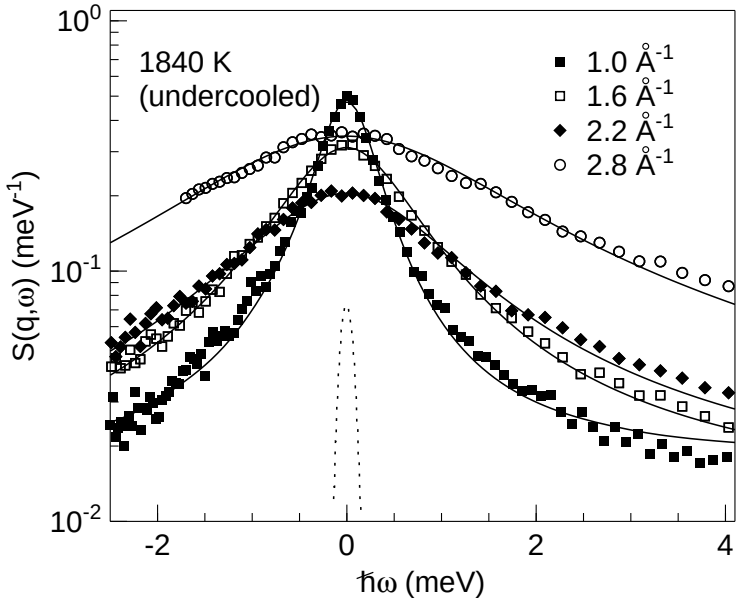

Figure 5.19: Scattering law of $Al_{50}Ni_{50}$ for various values of the momentum transfer q. The dotted line represents the energy resolution, the straight lines are Lorentzian fits to the data.

Fig. 5.19 are representations of a fit to the measured data, using the scaled Lorentz function convoluted with the instrumental energy resolution (FWHM 165 μeV), shown as dotted line.

For the lower q values 1.0 Å^{-1}, 1.6 Å^{-1}, and 2.2 Å^{-1}, we see a continuous broadening of the scattering law, connected with a reduced amplitude, so that the area of the Lorentzian stays constant. This relates to a constant structure factor, cf. section 3.4.5. For a momentum transfer q of 2.8 Å^{-1}, one can see that the linewidth is similar to the one at $q = 2.2$ Å^{-1}, but with increased amplitude. This indicates an increased scattering at the beginning of the first structure factor maximum. It has to be remarked that this scattering at higher q values cannot be attributed to dominant incoherent scattering anymore, but Fig. 5.19 shows that also in the region with strong coherent scattering contribution, the fit with a single (scaled) Lorentzian can describe the data rather well (note the semi-logarithmic plot of Fig. 5.19).

The area of this Lorentzian then relates to the static total structure factor, and from the linewidth we derive the effective diffusivity $D(q) = \frac{\Gamma_{1/2}}{\hbar q^2}$. This is shown in Fig. 5.20 for $Al_{50}Ni_{50}$ at 1758 K, i.e. nearly 200 K below the liquidus temperature of 1940 K. The red filled squares show the area of the

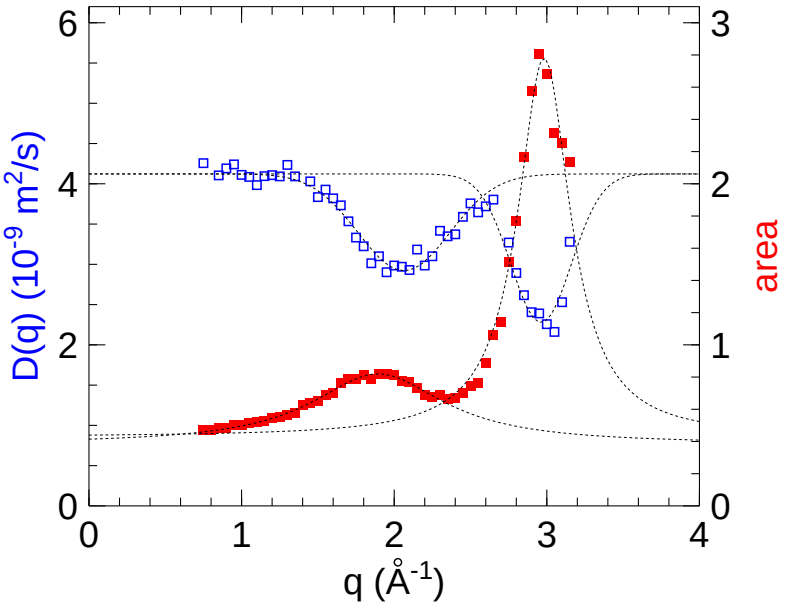

Figure 5.20: q dependent diffusivity (blue open squares) and area of the scaled Lorentz fit of the scattering law (red filled squares) for $Al_{50}Ni_{50}$ at 1758 K with an incoming wavelength of 3.8 Å. The dotted lines are guides to the eye.

fitted scattering law, i.e. the not normalized $S^*(q, \omega)$. We clearly see the first structure factor maximum at $q = 3.0$ Å^{-1}. For $q = 1.9$ Å^{-1}, the prepeak of CSRO is also nicely pronounced. The dotted lines of Fig. 5.20 are fitted Lorentzians as guide to the eye and to determine the peak positions.

If we now look at the diffusivity (blue open squares), we notice the known deviation from constant value, as soon as coherent scattering contributions become important, for $q > 1.4\,\text{Å}^{-1}$. But with the reduced incoming wavelength, we now can follow the development to higher q and also see the diffusivity increasing again, corresponding to a decrease in the quasi-elastic structure factor. The diffusivity then strongly decreases for $q > 2.6\,\text{Å}^{-1}$, when the region of the first structure factor maximum is reached.

The reduction in diffusivity for a maximum in the structure factor was predicted and explained by de Gennes [20]. It is usually found in liquid metals and glass forming systems [87]. Though originally developed regarding topological ordering, the first minimum of $D(q)$ shows that this so-called De Gennes narrowing also occurs for chemical ordering.

Yet it has to be noted that the reduction of diffusivity due to CSRO is not fully in phase with the structure factor, but always occurs at slightly higher q values. In the example of Fig. 5.20, the maximum of CSRO is at $q = 1.9\,\text{Å}^{-1}$, whereas the minimum of $D(q)$ lies at $q = 2.1\,\text{Å}^{-1}$. For the first structure factor maximum we find the position $q = 3.0\,\text{Å}^{-1}$, corresponding directly to the minimum in $D(q)$ at $q = 3.0\,\text{Å}^{-1}$. Also the ratio of amplitudes first structure factor maximum to CSRO prepeak is not reproduced in the minima of $D(q)$. A comparison with Fig. 5.5 and 5.6 might be helpful. There the position of the prepeak of CSRO was also at different positions. The static structure factor, similar to the area in Fig. 5.20, shows the prepeak at q values below $2\,\text{Å}^{-1}$, though it is composed of partial structure factors, whose Ni-Ni correlation structure factor shows a prepeak at about or shortly above $2\,\text{Å}^{-1}$. As the diffusivity probes the Ni dynamics, it is affected directly by the Ni-Ni correlations. Therefore it might be more appropriate to say that the diffusivity is in phase with the Ni-Ni partial structure factor.

We always found a reduced diffusivity when probed by neutrons with a momentum transfer where an increased ordering, be it chemical or topological, can be observed in the structure factor. This is a clear indication that indeed a preferred ordering of atoms leads to a reduced mobility/ an increased life time of the correlations.

5.3 Outlook: Ni-Zr

The electromagnetic levitation technique allowed also for the study of Zr based alloys in the liquid state, which are highly reactive. It was shown that the binary $Ni_{36}Zr_{64}$ shows similar mass transport behavior as the complex multicomponent vitralloys [41]. Therefore it is to be expected that properties

of multicomponent melts can be studied qualitatively but also quantitatively using a binary model system.

For the binary Ni-Zr alloy, it is possible to measure the partial structure factors. By this, the interplay between microscopic dynamics and structure can be discussed and simulated thoroughly. Fig. 5.21 shows the partial structure factors of $Zr_{64}Ni_{36}$ at 1350 K. From measurements at three $Zr_{64}Ni_{36}$

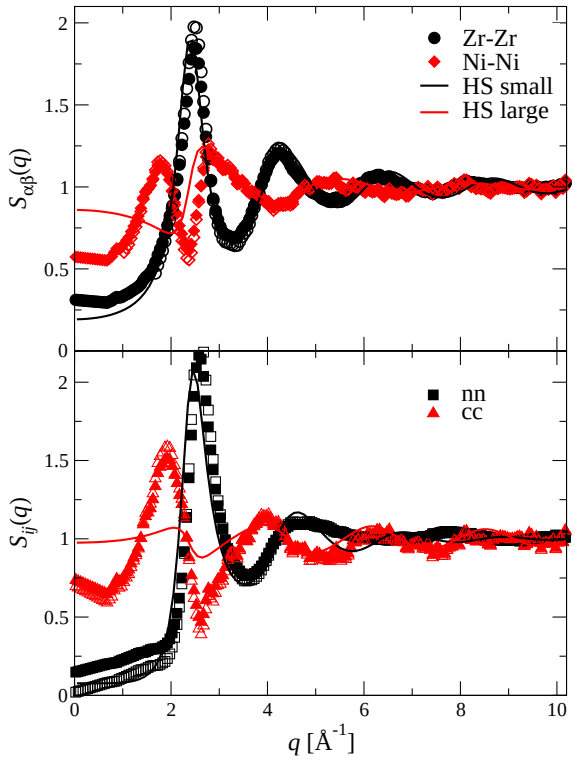

Figure 5.21: Faber-Ziman (top) and Bhatia-Thornton (bottom) partial structure factors of $Zr_{64}Ni_{36}$ at 1350 K. Symbols give measurement data from D20 at ILL. The lines are from hard-sphere calculations.

samples with natural Ni isotopic composition, ^{58}Ni, and ^{60}Ni enrichment, respectively, the partial structure factors in Faber-Ziman (top part of Fig. 5.21) have been determined, as well as the Bhatia-Thornton structure factors of concentration-concentration and number density correlations (bottom part). Filled and open symbols of each structure factor show two seperate data sets, which differ notably just in S_{NN} below 2 Å^{-1}. The lines are best fits with a hard-sphere model. It can sufficiently describe the Zr-Zr and number density structure factor, but not the Ni-Ni and concentration interactions, proofing again that CSRO is present and cannot be accounted for by random hard-sphere ordering.

Similar to the study of Al-Ni above, The Ni-Ni partial structure factor

shows a prepeak at $q \approx 1.8\,\text{Å}^{-1}$. This coincides with a peak in $S_{CC}(q)$. Again, a clear indication of CSRO.

And as the detailed study of [93] shows for this alloy, the self-diffusion of both constituents are strongly coupled, leading to equal values for the self-diffusion coefficient.

To illustrate this, we want to present one of the central results of [93] in Fig. 5.22. The data are derived from mode-coupling theory using the static

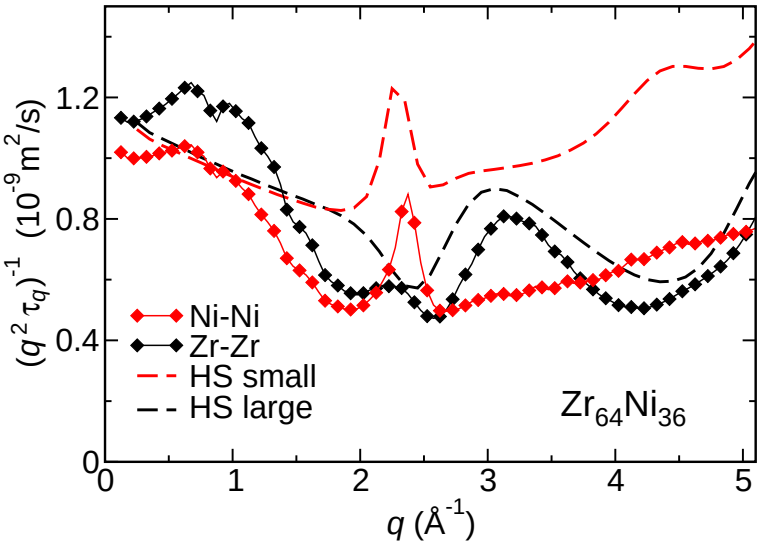

Figure 5.22: Inverse relaxation times $(q^2\tau_q)^{-1}$ at 1350 K for $\Phi_{\alpha\alpha}(q,t)$ with $\alpha =$ Zr (black) and Ni (red), calculated within mode-coupling theory as a function of wave number q. Symbols are using the experimental NiZr structure factor, lines are for the hard-sphere approximation.

partial structure factors of Fig. 5.21. The red and black data points show the Ni-Ni and Zr-Zr correlations, respectively. Plotted vs. q is the inverse of the relaxation time τ multiplied by q^2, which directly corresponds to the effective diffusivity of Fig. 5.20. For the Ni-Ni diffusivity, we observe the known double minimum corresponding to CSRO and topological ordering. Note that also in this case, the depth of the minima are rather equal than corresponding to the different heights of the structure factor peaks. The red dashed line shows result of a hard spheres simulation. Interestingly also in this case, a double minimum resulted, as the Ni atoms as minor species chiefly occupy spaces not taken by Zr in a random hard sphere mixture, causing a double peak in the structure factor. But the striking difference between the random hard sphere mixture and the real Ni-Zr alloy can be seen in the Zr-Zr correlation. There the hard sphere model shows only a single minimum in the Zr-Zr diffusivity,

corresponding to the single maximum of the structure factor. In contrast to this, the Zr-Zr diffusivity derived from actual measurements of the static partial structure factors clearly shows a double minimum, though the Zr-Zr structure factor has only a single maximum.

We can conclude that the dynamics of the Zr atoms is strongly influenced by the movement of the Ni atoms, as they are strongly correlated by CSRO. This CSRO leads to relaxation times which are not in phase with the structure factors.

It has been shown that CSRO leads to a decrease in diffusivity, and that the interactions of constituting atoms of a binary liquid alloy with CSRO are stronger coupled than can be inferred from the structure factors. Nevertheless there is a clear correlation between increased ordering, topological or chemical, and increased relaxation time, respective decreased diffusivity.

A quantitative comparison between binary and multicomponent melts becomes possible, as it was proven that material transport does not depend (at least not predominantly) on thermodynamic quantities, but chiefly on packing fraction and chemical ordering effects. So tailoring suitable binary melts opens new ways to principal understanding of multicomponent melts.

Also the violation of the Stokes-Einstein relation between viscosity and diffusion coefficient [66] should be studied in more detail. A way might be to use Neutron tomography to remeasure viscosities of multicomponent melts using a sort of inverse ball viscometer.

Chapter 6

Conclusion

This work presented measurements of the Ni self-diffusion coefficients, using a novel combination of existing techniques. Quasi-elastic neutron scattering with its intrinsic advantages for studying atomic processes was optimized using containerless sample positioning by electromagnetic levitation. This gave, firstly, access to a large range of momentum transfer q, enabling a close and detailed look on the dependence of the diffusion dynamics on the momentum transfer probed. A very clear narrowing of the linewidth of $S(q, \omega)$, for both topological and chemical ordering, was found.

The containerless sample positioning was secondly used to process alloys with a very high liquidus temperature. The dynamics of the Al-Ni system could be studied in the complete compositional range. We found Arrhenius-like behavior for all studied compositions and temperatures, and quite similar diffusion coefficients at respective liquidus temperatures. Also the activation energies were comparable (with the yet arguable exception of $Al_{68.5}Ni_{31.5}$).

$Al_{68.5}Ni_{31.5}$ was studied in the rather large temperature range of more than 270 K of undercooling up to temperatures above its liquidus temperature. The high liquidus intermetallic $Al_{50}Ni_{50}$ was also undercooled by about 200 K. This is the third large advantage of containerless processing, as container walls normally act as crystallization seeds. It was possible to keep the liquid alloys in the metastable undercooled state for hours to get sufficient scattering data for a detailed analysis. Neither quantitative nor qualitative differences showed upon undercooling. The dynamics stays the same in the metastable undercooled metallic melt.

The measurements on pure liquid Ni were a clear proof of feasibility of the combination of electromagnetic levitation with quasi-elastic neutron scattering. Multiple scattering is not influencing the determination of self-diffusion coefficients. The proportionality $\Gamma_{1/2} \propto q^2$ is valid for momentum transfers up to 1.2 Å^{-1}. The results in Ni presented a different picture than mea-

surements on metals with lower packing density, where for the temperature dependence of the diffusion coefficient, the universality of a T^2 law has been discussed. This can be clearly ruled out for Ni by the data from the undercooled Ni melt. The diffusion in Ni follows an Arrhenius-like temperature dependence.

The Ni self-diffusion coefficients were derived for Al-Ni alloys with Ni concentrations between 20 at. % and pure Ni. All in all, quasi-elastic neutron scattering on samples processed containerlessly produced Ni self-diffusion coefficients on an absolute scale with small error.

The dynamics in the binary alloy Al-Ni now give the following picture: Mass transport and diffusion depend strongly on the packing fraction. Starting on the Ni-rich side the Ni self-diffusion coefficient remains constant until about 50 at. % Al content, and then increases strongly. The density shows a consistent non-linear dependence on Al content. Al with a slightly smaller covalent radius (118 pm compared to 121 pm for Ni) takes at first, for Ni-rich binary alloys, positions of Ni atoms widely apart. This does not influence the dynamics of the system much. Only when there is enough Al in the composition, reducing also the density considerably, a clear increase in the Ni self-diffusion can be seen. The packing fraction is reduced, Ni atoms can move more freely. However, this does not occur similar to a random hard sphere process, where the atoms of the minority species move faster through the majority atoms which constitute the topolgical order. The Ni in Al-Ni shows a tendency to prefer certain coordinations. At certain distances – corresponding to the prepeak visible in the structure factors –, its pair correlations have significantly increased relaxation times (which is accompanied by a reduced relaxation time for the Al-Al correlation). So, the Ni atoms, though moving faster through an Al-richer environment, tend to keep their short-ranged chemical order. This in turn influences the diffusion of Al atoms. Both constituents, Ni as well as Al, will, by relaying of this CSRO, have similar self-diffusion coefficients.

Also the interdiffusion coefficient has an equal value and shows no q-dependence. The faster moving Al atoms together with the slower Ni atoms seem to cancel out, in connection with an increase in S_{CC}, indicating increased life time of agglomerates.

The diffusion in Al-Ni is thus depending on only a few quantities. Increasing temperature is just increasing the probability of the activated Arrhenius-like process, so diffusion increases. The activation energy – with the yet unclear exception of $Al_{68.5}Ni_{31.5}$ – is basically constant for the whole compositional range. Increasing Al concentration is reducing the packing fraction and thereby increasing the diffusion, a dependence on the underlying phase

diagram cannot be observed. The Ni self-diffusion coefficient at the respective liquidus temperatures of the alloys is changing only slightly with composition.

The determination of the dynamic partial structure factors in $Al_{80}Ni_{20}$ gave detailed insights how the prepeak visible in the total neutron scattering structure factor of most Al-Ni alloys [18] is the result of the three partial structure factors. In Faber-Ziman notation, the prepeak can be identified as stemming from the Ni-Ni correlations. The partial structure factor S_{NiNi} shows a prepeak shortly above $2\,\text{Å}^{-1}$, which lies at somewhat higher momentum transfer than in the static structure factor. In Bhatia-Thornton partial structure factors, the prepeak of CSRO shows up in S_{CC}, also above $2\,\text{Å}^{-1}$. By focusing on quasi-elastics, the effects of chemical short-range order clearly showed up.

Chemical short-range order, similar to topological ordering, leads to reduced diffusivity at respective q values, an effect termed *De Gennes narrowing*. But as it comes from only one of the particle-particle correlations, in our case Ni-Ni, the position of the minimum of diffusivity lies at higher q values than the the maximum of the respective prepeak of CSRO.

These findings of the Al-Ni system were and will be taken to study the dynamics in other binary and multicomponent alloys, to learn more about the material transport mechanism, highly important in the process of crystallization.

To conclude, this work gave new insights in the working of atomic transport in metallic liquids and offered a new experimental technique suitable to more detailed studies in this area.

Appendix A

Neutron scattering cross sections

	b [fm]	σ_{coh} [barn]	σ_{inc} [barn]	σ_{abs} [barn]
^{na}Ni	10.3	13.3	5.2	4.49
^{58}Ni	14.4	26.1	0	4.6
^{60}Ni	2.8	0.99	0	2.9
Al	3.449	1.495	0.0082	0.231
V	-0.382	0.0184	5.08	5.08

natural Ni isotopic composition:

68.27 % ^{58}Ni
26.1 % ^{60}Ni
1.13 % ^{61}Ni
3.59 % ^{62}Ni
0.91 % ^{64}Ni

All data from [78].

Appendix B

Listing of Diffusion Coefficients

Table B.1: Ni self-diffusion coefficients. The temperature is $\pm$ 5 K.

	T_{liq} [K]	T [K]	D [$10^{-9}\,\mathrm{m^2 s^{-1}}$]
Ni	1726	1514	2.09 ± 0.08
		1621	2.68 ± 0.12
		1750	3.47 ± 0.06
		1810	3.68 ± 0.07
		1870	4.05 ± 0.2
		1940	4.54 ± 0.23

Table B.2: Ni self-diffusion coefficients of Al-Ni alloys. The temperature is $\pm$ 5 K.

	T_{liq} [K]	T [K]	D [$10^{-9}\,\mathrm{m^2 s^{-1}}$]
$Al_{25}Ni_{75}$	1658	1689	3.22 ± 0.08
		1868	4.35 ± 0.05
		1928	4.90 ± 0.20
$Al_{50}Ni_{50}$	1940	1758	3.7 ± 0.3
		1840	4.35 ± 0.17
		1892	4.59 ± 0.11
$Al_{68.5}Ni_{31.5}$	1613	1352	1.83 ± 0.03
		1417	2.29 ± 0.10
		1484	2.87 ± 0.04
		1543	3.28 ± 0.13
		1630	4.03 ± 0.18
$Al_{80}Ni_{20}$	1245	1259	2.91 ± 0.09
		1350	3.93 ± 0.14

Table B.3: Ni self-diffusion coefficients of Ni-Zr alloys. The temperature is ± 5 K.

	T_{liq} [K]	T [K]	D [$10^{-9}\,m^2s^{-1}$]
Ni_5Zr	1620	1638	3.1 ± 0.3
$Ni_{64}Zr_{36}$	1343	1348	0.49 ± 0.07
		1460	1.02 ± 0.07
		1546	1.17 ± 0.08
		1649	1.68 ± 0.05
$Ni_{50}Zr_{50}$	1533	1354	0.48 ± 0.06
		1416	0.78 ± 0.08
		1475	0.98 ± 0.08
		1545	1.37 ± 0.13
		1657	1.82 ± 0.18
		1750	2.54 ± 0.13
		1800	2.75 ± 0.14
$Ni_{36}Zr_{64}$	1283	1210	0.36 ± 0.09
		1292	0.66 ± 0.04
		1344	0.75 ± 0.08
		1457	1.23 ± 0.13
		1544	1.66 ± 0.15
		1649	2.18 ± 0.12
$Al_{15}Ni_{25}Zr_{60}$	1215	1241	0.23 ± 0.05
		1348	0.44 ± 0.04
		1430	0.72 ± 0.08
		1510	1.02 ± 0.11

Table B.4: Other studied alloys containing a strong incoherent scatterer, Ni, Ti, or Co. The temperature is $\pm$ 5 K.

	T_{liq} [K]	T [K]	D [$10^{-9}\,m^2s^{-1}$]
$Ni_{80}P_{20}$	1173	1224	1.26 ± 0.03
		1273	1.52 ± 0.09
Ti	1941	2000	5.06 ± 0.25
$Fe_{73}Ti_{27}$	1403	1321	1.05 ± 0.15
		1441	1.73 ± 0.04
$Al_{68.8}Ag_{18.1}Cu_{13.1}$	773	783	2.28 ± 0.13
		823	2.69 ± 0.21
		873	3.1 ± 0.3
		923	3.6 ± 0.3
		973	4.0 ± 0.45
$Al_{13}Co_4$	1443	1376	0.90 ± 0.07
		1520	1.9 ± 0.18
$Al_{49.4}Ti_{50.5}$	1763	1577	1.88 ± 1.9
		1687	2.81 ± 2.9
		1731	3.3 ± 0.4
		1783	3.9 ± 0.4
$Al_{60}Ti_{40}$	1714	1477	0.94 ± 0.10
		1527	1.60 ± 0.16
		1586	2.10 ± 0.21
		1653	2.53 ± 0.26
		1774	3.7 ± 0.4

Appendix C

Publications of the author

1. *Determination of self-diffusion coefficients by quasielastic neutron scattering measurements of levitated Ni droplets.* A. Meyer, S. Stüber, D. Holland-Moritz, O. Heinen and T. Unruh, Phys. Rev. B **77**, 092201 (2008).

2. *Atomic diffusion mechanisms in a binary metallic melt.* Th. Voigtmann, A. Meyer, D. Holland-Moritz, S. Stüber, T. Hansen and T. Unruh, EPL **82**, 66001 (2008).

3. *Structure and dynamics of liquid $Ni_{36}Zr_{64}$ studied by neutron scattering.* D. Holland-Moritz, S. Stüber, H. Hartmann, T. Unruh, T. Hansen and A. Meyer, Phys. Rev. B **79**, 064204 (2009).

4. *Ni self-diffusion in Zr-Ni(-Al) melts.* D. Holland-Moritz, S. Stüber, H. Hartmann, T. Unruh and A. Meyer, J. Phys.: Conf. Ser. **144**, 012119 (2009).

5. *Dynamics in refractory Al-Ni melts.* S. Stüber, A. Meyer, D. Holland-Moritz and T. Unruh (in preparation).

Bibliography

[1] M. J. Assael, K. Kakosimos, R. M. Banish, J. Brillo, I. Egry, R. Brooks, P. N. Quested, K. C. Mills, A. Nagashima, Y. Sato, and W. Wakeham, J. Phys. Chem. Ref. Data **35**, 285 (2006).

[2] M. Asta, V. Ozoliņš, J. J. Hoyt, and M. van Schilfgaarde, Phys. Rev. B **64**, 020201(R) (2001).

[3] G. D. Ayushina, E. S. Levin, and P. V. Gel'd, Russ. J. Phys. Chem. **43**, 1548 (1969).

[4] U. Balucani and M. Zoppi. *Dynamics of the Liquid State*. Clarendon, Oxford, 1994.

[5] M. Barth, B. Wei, and D. M. Herlach, Phys. Rev. B **51**, 3422 (1995).

[6] A. B. Bhatia and D. E. Thornton, Phys. Rev. B **2**, 3004 (1970).

[7] A. B. Bhatia, D. E. Thornton, and N. H. March, Phys. Chem. Liq. **4**, 97 (1974).

[8] X.-F. Bian, J.-X. Zhang, Y.-B. Jia, and M.-H. Sun, Chin. Phys. Lett. **22**, 644 (2005).

[9] W. J. Boettinger, J. A. Warren, C. Beckermann, and A. Karma, Annu. Rev. Mater. Res. **32**, 163 (2002).

[10] J. Brillo and I. Egry, Z. Metallkd. **95**, 691 (2004).

[11] J. Brillo, A. Bytchkov, I. Egry, L. Hennet, G. Mathiak, I. Pozdnyakova, D.L. Price, D. Thiaudiere, and D. Zanghi, J. Non-Cryst. Solid **352**, 4008 (2006).

[12] J. Brillo, G. Lohöfer, F. Schmidt-Hohagen, S. Schneider, and I. Egry, Int. J. Mater. Prod. Tec. **26**, 247 (2006).

[13] J. Brillo, S. M. Chathoth, M. M. Koza, and A. Meyer, Appl. Phys. Lett. **93** (2008 (to be published)).

[14] R. F. Brooks, A. T. Dinsdale, and P. N. Quested, Meas. Sci. Technol. **16**, 354 (2005).

[15] S. Chandrasekhar, Proc. Lond. Math. Soc. **9**, 141 (1959).

[16] S. Mavila Chathoth, Ph.D. thesis, Technische Universität München, 2005.

[17] S. Mavila Chathoth, A. Meyer, M. M. Koza, and F. Juranyi, Appl. Phys. Lett. **85**, 4881 (2004).

[18] S. K. Das, J. Horbach, M. M. Koza, S. Mavila Chathoth, and A. Meyer, Appl. Phys. Lett. **86**, 011918 (2005).

[19] S. K. Das, J. Horbach, and T. Voigtmann, Phys. Rev. B **78**, 064208 (2008).

[20] P. G. de Gennes, Physica **25**, 825 (1959).

[21] M. J. Donachie. *Superalloys: a technical guide.* ASM International, Materials Park, 2002.

[22] I. Egry, L. Hennet, M. Kehr, G. Mathiak, S. De Panfilis, I. Pozdnyakova, and D. Zanghi, J. Chem. Phys. **129**, 064508 (2008).

[23] N. El-Kaddah and J. Szekely, Metall. Trans. B **15B**, 183 (1984).

[24] J. E. Enderby. *Amorphous Solids and the Liquid State*, chapter 1. Plenum Press, New York and London, 1985.

[25] T. E. Faber and J. M. Ziman, Phil. Mag. **11**, 153 (1965).

[26] F. Faupel, W. Franka, M.-P. Macht, H. Mehrer, V. Naundorf, K. Rätzke, H. R. Schober, S. K. Sharma, and H. Teichler, Rev. Mod. Phys. **75**, 237 (2003).

[27] J. L. Finney. *Amorphous Solids and the Liquid State*, chapter 2. Plenum Press, New York and London, 1985.

[28] T. Franosch, W. Götze, M. R. Mayr, and A. P. Singh, Phys. Rev. E **55**, 3183 (1997).

[29] J. Frenkel, Phys. Z. Sowjetunion **1**, 498 (1932).

[30] J. P. Garandet, G. Mathiak, V. Botton, P. Lehmann, and A. Griesche, Int. J. Thermophys. **25**, 249 (2004).

[31] W. Götze and Th. Voigtmann, Phys. Rev. E **67**, 021502 (2003).

[32] A. Griesche, M.-P. Macht, and G. Frohberg, J. Non-Cryst. Solids **353**, 3305 (2007).

[33] A. Griesche, B. Zhang, J. Horbach, and A. Meyer, Defect Diff. Forum (submitted).

[34] D. Gupta, K. N. Tu, and K. W. Asai, Phys. Rev. Lett. **35**, 796 (1975).

[35] A. G. C. Gwyer, Z. anorg. Chem. **57**, 133 (1908).

[36] J.-P. Hansen and I. R. McDonald. *Theory of Simple Liquids*. Academic, London, 2nd edition, 1986.

[37] M. Hansen. *Constitution of binary alloys*. McGraw-Hill Book Company, New York, Toronto and London, 1958.

[38] D. M. Herlach, R. F. Cochrane, I. Egry, H. J. Fecht, and A. L. Greer, Int. Mater. Rev. **38**, 273 (1993).

[39] D. Holland-Moritz, Habilitation, Ruhr-Universität Bochum, 2003.

[40] D. Holland-Moritz, T. Schenk, P. Convert, T. Hansen, and D. M. Herlach, Meas. Sci. Technol. **16**, 372 (2005).

[41] D. Holland-Moritz, S. Stüber, H. Hartmann, T. Unruh, T. Hansen, and A. Meyer, Phys. Rev. B **79**, 064204 (2009).

[42] J. Horbach. private communications.

[43] J. Horbach, S. K. Das, A. Griesche, M.-P. Macht, G. Frohberg, and A. Meyer, Phys. Rev. B **75**, 174304 (2007).

[44] S. Hosokawa, Y. Kawakita, W.-C. Pilgrim, and H. Sinn, Phys. Rev. B **63**, 134205 (2001).

[45] W. D. Huang, B. J. Yang, and R. W. Smith, J. Appl. Phys. **96**, 6213 (2004). See comment [82] and response [83].

[46] T. Itami, T. Masaki, H. Aoki, S. Munejiri, M. Uchida, S. Matsumoto, K. Kamaiyama, and K. Hoshino, J. Non-Cryst. Solid **312-314**, 177 (2002).

[47] N. Jakse, O. Lebacq, and A. Pasturel, Phys. Rev. Lett. **93**, 207801 (2004).

[48] F. Kargl, Ph.D. thesis, Technische Universität München, 2006.

[49] M. Kehr, W. Hoyer, and I. Egry, Int. J. Thermophys. **28**, 1017 (2007).

[50] A. Kerrache, J. Horbach, and K. Binder, EPL **81**, 58001 (2008).

[51] J. S. Kirkaldy and D. Y. Young. *Diffusion in the Condensed State*. The Institute of Metals, London, 1987.

[52] M. Kizilyalli, J. Corish, and R. Metselaar, Pure Appl. Chem. **71**, 1307 (1999).

[53] P. Kleban, J. Stat. Phys. **11**, 317 (1974).

[54] M. Kolbe, S. Reutzel, A. Patty, I. Egry, L. Rattke, and D. M. Herlach. *Multiphase Phenomena and CFD Modeling and Simulation in Materials Processes*, chapter Undercooling and demixing of CuCo melts in the TEMPUS facility during parabolic flight. TMS, Warrendale, 2004.

[55] S. Krishnan, J. J. Felten, J. E. Rix, J. K. Weber, P. C. Nordine, M. A. Beno, S. Ansell, and D. L. Price, Rev. Sci. Instrum. **68**, 3512 (1997).

[56] H. Landolt, O. Madelung, and H. Ahlers, editors. *Numerical data and functional relationships in science and technology / New series / Units and fundamental constants in physics and chemistry*. Springer, Berlin, 1991.

[57] Institut Laue-Langevin, 2008. http://www.ill.eu/d20/home/.

[58] S. Lefebvre, A. Quivy, J. Bigot, Y. Calvayrac, and R. Bellissent, J. Phys. F: Met. Phys. **15**, L99 (1985).

[59] X.J. Liu, X.D. Hui, H.Y. Hou, T. Liu, and G.L. Chen, Physics Letters A **372**, 3313 (2008).

[60] M. Maret, A. Pasturel, C. Senillou, J. M. Dubois, and P. Chieux, J. Phys. France **50**, 295 (1989).

[61] M. Maret, T. Pomme, A. Pasturel, and P. Chieux, Phys. Rev. B **42**, 1598 (1990).

[62] W. Marshall and S. W. Lovesey. Oxford University Press, Oxford, 1971.

[63] G. Mathiak, A. Griesche, K. H. Kraatz, and G. Frohberg, J. Non-Cryst. Solid **205-207**, 412 (1996).

[64] D. Mayou and A. Pasturel, J. Phys.: Condens. Matter **1**, 9685 (1989).

[65] A. Meyer, Phys. Rev. B **66**, 134205 (2002).

[66] A. Meyer, W. Petry, M. Koza, and M.-P. Macht, Appl. Phys. Lett. **83**, 3894 (2003).

[67] A. Meyer, S. Stüber, D. Holland-Moritz, O. Heinen, and T. Unruh, Phys. Rev. B **77**, 092201 (2008).

[68] Y. Mishin, M. J. Mehl, and D. A. Papaconstantopoulos, Phys. Rev. B **65**, 224114 (2002).

[69] S. Munejiri, T. Masaki, T. Itami, F. Shimojo, and K. Hoshino, Phys. Rev. B **77**, 014206 (2008).

[70] N. H. Nachtrieb, J. Chem. Phys. **24**, 746 (1956).

[71] H. H. Paalman and C. J. Pings, J. Appl. Phys. **33**, 2635 (1962).

[72] M. S. Petrushevskii, E. S. Levin, and P. V. Gel'd, Russ. J. Phys. Chem. **45**, 1719 (1971).

[73] P. Protopapas, H. C. Andersen, and N. A. Parlee, J. Chem. Phys. **59**, 15 (1973).

[74] W. K. Rhim, S. K. Chung, D. Barber, K. F. Man, G. Gutt, A. Rulison, and R. E. Spjut, Rev. Sci. Instrum. **64**, 2961 (1993).

[75] D. Richter. *Neutron Scattering*, chapter 2. Forschungszentrum Jülich GmbH, Jülich, 2000.

[76] W. C. Roberts-Austen, Proc. R. Soc. Lond. **59**, 281 (1895-1896).

[77] T. Schenk, D. Holland-Moritz, V. Simonet, R. Bellissent, and D. M. Herlach, Phys. Rev. Lett. **89**, 075507 (2002).

[78] V. F. Sears, Neutron News **3**, 26 (1992).

[79] P. G. Shewmon. *Physical Metallurgy*, chapter Diffusion. North-Holland Publishing Company, Amsterdam, 1965.

[80] M. Shimoji. *Liquid Metals*. Academic, London, 1977.

[81] M. Shimoji and T. Itami. *Atomic Transport in Liquid Metals*. Trans. Tech. Publ., Aedermannsdorf, 1986.

[82] M. Shirkhanzadeh, J. Appl. Phys. **102**, 086102 (2007).

[83] R. W. Smith, J. Appl. Phys. **102**, 086103 (2007).

[84] M. Soltwisch, D. Quitmann, H. Ruppersberg, and J. B. Suck, Phys. Rev. B **28**, 5583 (1983).

[85] G. L. Squires. *Introduction to the theory of thermal neutron scattering*. Dover, Mineola, 1996.

[86] C. Stelian, J. Cryst. Growth **310**, 1552 (2008).

[87] A. Tölle, Rep. Prog. Phys. **64**, 1473 (2001).

[88] C. Tomaras. Technical report, Technische Universität München, 2007 (unpublished).

[89] H. J. V. Tyrrell and K. R. Harris. *Diffusion Liquids*. Butterworths, London, 1984.

[90] H. Uhlig, L. Rohr, H. J. Guntherodt, P. Fischer, P. Lamparter, and S. Steeb, Zeitschrift für Naturforschung A **47A**, 826 (1992).

[91] T. Unruh, J. Neuhaus, and W. Petry, Nucl. Instrum. Methods A **580**, 1414 (2007). See erratum [92].

[92] T. Unruh, J. Neuhaus, and W. Petry, Nucl. Instrum. Methods A **585**, 201(E) (2008).

[93] Th. Voigtmann, A. Meyer, D. Holland-Moritz, S. Stüber, T. Hansen, and T. Unruh, EPL **82**, 66001 (2008).

[94] H. A. Wilson, Philos. Mag. **50**, 238 (1900).

[95] J. Wuttke, 2008. http://iffwww.iff.kfa-juelich.de/∼wuttke/doku/doku.php?id=frida:frida.

[96] H. Zabel. *Neutron and Synchrotron Radiation for Condensed Matter Studies*, chapter XIV. Springer Verlag, Berlin, 1993.

[97] V. Zöllmer, K. Rätzke, F. Faupel, and A. Meyer, Phys. Rev. Lett. **90**, 195502 (2003).

[98] R. Zorn and D. Richter. *Neutron Scattering*, chapter 2. Forschungszentrum Jülich GmbH, Jülich, 2000.

Acknowledgments

First of all, I have to thank my adviser Prof. Andreas Meyer, for his continuing and enthralling enthusiasm for this topic.

I also want to thank Oliver Heinen from DLR Köln for introducing me to the handling of the levitation apparatus, Fan Yang and Andreas Meier-Koll, my fellow PhD students from TU München for their devotional help during beam-time, Thomas Voigtmann of DLR for help in theory and the mode-coupling calculations, and of course DFG-SPP 1120 for funding.

For proof-reading the manuscript, I want to thank Fan Yang.